

UNIVERSITY OF BELGRADE
FACULTY OF MECHANICAL ENGINEERING

Abubakr M. Abdulgadr Kraedegh

**FATIGUE CRACK GROWTH IN T WELDED
JOINT OF ALUMINUM ALLOY**

Doctoral Dissertation

Belgrade, 2017

UNIVERZITET U BEOGRADU

MAŠINSKI FAKULTET

Abubakr M. Abdulgadr Kraedegh

**RAST ZAMORNE PRSLINE U T
ZAVARENOM SPOJU LEGURE
ALUMINIJUMA**

doktorska disertacija

Beograd, 2017

SUPERVISOR:

Dr. Aleksandar Sedmak, full professor
Faculty of Mechanical Engineering, Belgrade

BOARD OF COMMISSION:

Dr. Zoran Radakovic, full professor
Faculty of Mechanical Engineering, Belgrade

Dr. Aleksandar Grbovic, associate professor
Faculty of Mechanical Engineering, Belgrade

Dr. Emil Veg, assistant professor
Faculty of Mechanical Engineering, Belgrade

Dr. zijah Burzic, scientific adviser
Military Technical Institute, Belgrade

Date of defense:

DEDICATION

To my parents, my wife, my kids and my teachers

Acknowledgements

First of all, I would like to express my sincere gratitude to my supervisor Professor Aleksandar Sedmak. He offers continuous support to my paper writing, thesis revision and other academic activities such as international conferences, offering numerous suggestions and guides to my research. I also thank Dr. Aleksandar Grbovic for all his continues help, support, and interest in structural integrity assessment using continuum finite element analysis and ABAQUS benefits me a lot in my research. I am grateful to Dr. Blagoj Petroveski for his encouragement, guidance and support. I appreciate the help offered by Prof. Dr. M. Burzic in finishing the carried out experimental work.

A special thank is given to the staffs of Mechanical Engineering Faculty. I appreciate their help and their kindness.

My sincere appreciation, thanks and gratitude to the Libyan academic attaché in Serbia, which has supported me to my further education.

Finally, my sincere appreciation, thanks and gratitude to my wife and kids for their patience during the period of my study.

FATIGUE CRACK GROWTH IN T WELDED JOINT OF ALUMINUM ALLOY

Abstrakt:

U ovom radu su prikazani inicijacija i rast prsline u T spoju ploče od aluminijumske legure AA2024 –T351, zavarenom mešanjem trenjem (Friction Stir Welding - FSW), primenom mehanike loma. Svi analizirani modeli su napravljeni od legure 2024-A351. Osobine materijala i dimenzije u oblasti FSW spoja su usvojene na osnovu dostupnih eksperimenata.

Uticaj rasta prsline na zamorni vek neukrućenih i ukrućenih konstrukcija je razmatran primenom numeričkih metoda zasnovanih na analizi konačnim elementima – proširenoj metodi konačnih elemenata (PMKE). Korišćeni su softverski paketi ABAQUS i Morfeo za prikaz rezultata rasta prsline u svim oblastima T spojevia ploča zavarenih mešanjem trenjem. Urađeno je ispitivanje savijanja u tri tačke, sa odnosom napona $R = 0$. Takođe je zadato i zatezno zamorno opterećenje za različite odnose napona (0.5, 0 i -1).

Svi analizirani modeli su napravljeni od legure 2024-A351. Osobine materijala i dimenzije u oblasti FSW spoja su usvojene na osnovu dostupnih eksperimenata. Analizirani su sledeći primeri:

- Primer 1 Modeliranje konačnim elementima sučeonog zavarenog spoja pod čistim statičkim savijanjem u tri tačke
- Primer 2 Modeliranje konačnim elementima T zavarenog spoja pod čistim statičkim savijanjem u tri tačke
- Uticaji ukrućenja na napredovanje zamorne prsline zavarene ploče
- Primer 1 Modeliranje konačnim elementima sučeonog spoja pod statičkim zateznom opterećenjem
- Primer 2 Modeliranje konačnim elementima T zavarenog spoja pod statičkim zateznom opterećenjem
- Primer 3 Modeliranje konačnim elementima dvostrukog T spoja pod statičkim zateznom opterećenjem
- Uticaj odnosa napona na napredovanje zamorne prsline u dvostrukom T zavarenom spoju pod statičkim zateznom opterećenjem
- Primer 1 Odnos napona 0.5
- Primer 2 Odnos napona 0
- Primer 3 Odnos napona -1

- Eksperimentalna verifikacija numeričkih rezultata dobijenih za T spojeve zavarene mešanjem trenjem

Dobijeni su sledeći rezultati

- Numerički proračuni:
 - Koordinate x , y i z za vrh prsline u svakom koraku,
 - Raspodele faktora intenziteta napona – K_I duž fronta prsline u svakom koraku,
 - Zamorni vek izražen preko broja promena primenjenog opterećenja – N za svaki korak napredovanja prsline.
 - Brzine rasta zamorne prsline su prikazane u odnosu na raspodelu faktora intenziteta napona – K_I .
- Eksperimentalna verifikacija numeričkih rezultata ispitivanja T spojeva zavarenih mešanjem trenjem, uključujući i:
 - Zamorni vek izražen preko broja promena primenjenog opterećenja – N za svaki korak.

Ključne reči: zamorni rast prsline, proširena metoda konačnih elemenata (PMKE), žilavost loma, zavarivanje mešanjem trenjem (FSW), softver, zavarena konstrukcija, LEML – linearno-elastična mehanika loma, K – faktor intenziteta napona

Abstract:

In this present work, application of fracture mechanics is used to present a fatigue crack initiation and growth of friction stir welded (FSW) T joint plate made of aluminum alloy AA2024 –T351. All analyzed models are made from aluminum alloy 2024-T351. The properties of materials in the areas of joints and geometry measures of FSW joint are adopted from available experiments.

The effect of crack growth on fatigue life of unstiffened and stiffened structures is considered by using the numerical method based on finite elements - extended Finite Element Method (XFEM). ABAQUS software and Morfeo are used to display the results of the growth of cracks in welded T joint plates of FSW in all regions. Three point – bending load is applied, with stress intensity ratio $R = 0$. Tension fatigue load is also applied with different stress ratio of $R = (0.5, 0, \text{ and } -1)$

All analyzed models are made from aluminum alloy 2024-T351. Material properties in joints zones and geometry measures of FSW joint are adopted from available experiments. Following examples are analyzed:

- Example 1 Finite element modelling of butt welded joint under static pure Three - Point Bending Load
- Example 2 Finite element modelling of T welded joint under static pure Three - Point Bending Load
- Effect of stiffeners on fatigue crack propagation of welded plate
- Example 1 Finite element modelling of butt welded joint under static tensile loading
- Example 2 Finite element modelling of T welded joint under static tensile loading
- Example 3 Finite element modelling of double T welded joint under static tensile loading
- Effect of stress ratio on fatigue crack propagation of double T welded joint plate under static tensile loading
- Example 1 Stress ratio of 0.5
- Example 2 Stress ratio of 0
- Example 3 Stress ratio of -1

- Experimental Validation of Numerical Results of friction stir welded T-joints

Following results are obtain

- Numerical computations:
 - Points coordinates of crack front x, y, z for every progression step,

- Distributions of stress intensity factors- K_I along crack front for each progressions step,
 - Fatigue life in form of applied load number change - N for each step of propagation.
 - Fatigue crack growth rates are plotted versus the distribution of stress intensity factors – K_I .
- Experimental Validation of Numerical Results of friction stir welded T-joints is analysed with the following:
- Fatigue life in form of applied load number change - N for each step of propagation.

Keywords: fatigue crack growth, extended Finite Element Method (*XFEM*), fracture toughness, Friction Stir Welding (*FSW*), software, welded construction, *LEFM* - linear-elastic fracture mechanics, stress intensity factor- K ,

Scientific discipline:

Mechanical engineering

Scientific subdiscipline:

Structure integrity

UDC number:

621.791.05:669.715:620.178.3(043.3)

Nomenclature

a	Crack length
a_0	Initial crack length
B	Specimen thickness
E	Young's modulus
F	Applied force
J	J -integral
K	Stress intensity factor
K_I	Mode-I stress intensity factor
K_{eff}	Effective stress intensity factor
K_{IC}	Plane strain linear elastic fracture toughness
n	Strain hardening exponent
S	Distance between the two supports in 3-point bending specimen
W	Specimen width
ε_e	Elastic strain
ε_f	Fracture strain
ε_p	Plastic strain
ν	Poisson's ratio
$\sigma_1, \sigma_2, \sigma_3$	Principle stresses
σ_e	Effective stress
σ_{eq}	Von Mises equivalent stress
σ_f	Fracture stress
σ_m	Mean stress
σ_{max}	Maximum applied normal stress
σ_{min}	Minimum applied normal stress
τ	Tangential (shear) voltage
σ_{YS}	Yield strength
Δa	Crack length increment
b	The width of the element on the front of the crack

b_i^a	A nodal vector enhanced by the NT function
B_a	Matrix derivative of improved functions
B_u	Matrix derivative of classical functions
A, B, C, D	empirical constants of crack growth model
C	Constant (in Paris equation)
$\frac{da}{dN}$	Fatigue crack growth rate
d	The length of the element on the front of the crack
f	Fracture criterion
ΔK	Stress intensity factors range
ΔK_{th}	The range of stress intensity factors threshold
r	Radius of rotation
r_p	The dimension size of the plastic region
R	Stress ratio
t	Sample thickness
t_0	Characteristic sample thickness (material constant)
T	Temperature
u	Vector of movement of classical degrees of freedom
u_i	Displacement vector of the final element
u_x	Move in the X direction
u_y	Move in the Y direction
$u^h(x)$	Displacement function vector
Γ	Integration path
W	Work
γ_s	Unit surface energy
δ	Measured value of crack opening
μ	Slip module
θ	angle in the polar-cylindrical coordinate system
$\psi(r, \theta)$	Function of improvement
$\psi_\alpha(x)$	α – The enhancement function in the i – node ($\alpha \in ([1, m])$)
Φ	Factor in the Willenborg equation

Abbreviations

AA	Aluminum Association
ASME	American Society of Mechanical Engineers
ASTM	American Society for Testing and Materials
BM	base material
FEM	finite element method
LEFM	linear elastic fracture mechanics
FSW	Friction Stir Welding
HAZ	heat affected zone
LBW	laser beam welding
MIG	metal inert gas (welding)
SIF(s)	stress intensity factor(s)
SN	stress level versus number of cycles (curve)
N	nugget zone
TMAZ	thermo-mechanically affected zone
TWI	the Welding Institute
VCCT	virtual crack closure technique
SENB	single edge notched bend
CTOD	crack tip opening displacement
<i>R</i> -curve	fracture material resistance curve
SSY	small scale yielding
<i>J-R</i>	<i>J</i> -resistance (fracture resistance)

Table of contents

1	Introduction.....	1
1.1	Introduction	1
1.2	Research Requirements and Objectives	3
1.3	Thesis Outline	6
2	Literature Reviews.....	8
2.1	Aluminum-Copper-Magnesium Alloys	8
2.2	Design of welded aluminum aerospace structures	9
2.3	Friction stir welding of T-joints	11
2.3.1	Fatigue properties in FSW aluminum alloys	11
2.3.2	Fatigue crack growth behavior in FSW aluminum alloys	14
3	Friction Stir Welding: Process Modelling and Microstructure.....	18
3.1	Introduction	18
3.2	Description of Friction Stir welding (FSW).....	19
3.2.1	Important welding parameters	22
3.2.2	Heat generations during Friction Stir welding.....	26
3.2.3	Microstructure modification	30
3.3	Advantages and drawbacks of Friction Stir welding	32
3.4	Friction Stir Welding (FSW) of T joints	34
3.5	Aluminum alloys	37
3.5.1	Joining of aluminum alloys.....	40
3.6	Residual stress in friction stir welded aluminum alloys.....	41
3.7	Fatigue properties of friction stir welds	42
3.8	Concluding Remarks	44
4	Fracture mechanics concepts	45
4.1	Introduction	45
4.2	Fatigue behavior of metallic materials	46

4.3	Fracture mechanics approach on fatigue	47
4.3.1	Linear Elastic Fracture Mechanics (LEFM)	48
4.3.2	Elastic – Plastic Fracture mechanics.....	57
4.4	Fatigue crack growth.....	61
4.4.1	Initiation and stage I fatigue crack growth	61
4.4.2	Stage II fatigue crack growth.....	62
4.4.3	Stage III fatigue crack growth (final fracture)	63
4.5	Fatigue Life Prediction.....	64
4.5.1	High cycle fatigue	65
4.5.2	Low cycle fatigue.....	65
4.6	Fatigue Assessment of Welded structures.....	66
4.6.1	Fatigue Behavior of FSW Aluminum Joints.....	67
5	Extended Finite Element Method (XFEM)–Numerical simulation	69
5.1	Introduction	69
5.2	Basics of extended finite element method.....	70
5.2.1	Defining of the displacement field <i>XFEM</i> – <i>u</i>	71
5.2.2	The general form of the extended finite element method	73
5.3	XFEM Implementation in Abaqus	75
5.3.1	Modeling Approach	76
5.3.2	Virtual Crack Closure Technique	76
5.4	Fracture Growth Criteria	78
5.4.1	Evaluation of the stress intensity factors	79
5.4.2	Difficulties in the XFEM	80
5.5	Morfeo/crack for Abaqus	81
5.5.1	Extended description of Morfeo/crack for Abaqus.....	81
5.6	Stress intensity factor calculation using 3D finite element models	82
5.6.1	Introduction.....	82

5.6.2	Finite element modelling of T welded joint under static pure Three - Point Bending Load.....	84
5.6.3	Finite element modelling of welded joint under static Tensile Load.....	93
	Results and Discussion	113
6	Experimental Validation of Numerical Results of friction stir welded T-joints	115
6.1	Introduction	115
6.2	Material	115
6.2.1	Chemical composition	115
6.2.2	Metallography	115
6.3	Specimen preparation and Tests description.....	118
6.4	Experimental investigation of fatigue crack growth	118
6.5	Finite Element Model (FEM) and Analysis	120
6.5.1	Material model.....	120
6.5.2	FEA software	120
6.5.3	Numerical model.....	121
6.6	Experimental & Numerical results and discussion	126
7	Conclusions and Recommendations.....	128
	References.....	131

Table of figures

Figure 1.1 Optical micrograph of kissing bond and root flaw in conventional FSW joint.....	5
Figure 1.2 S-N curves of flaws (bonded) and sound conventional FSW joint	6
Figure 1.3 Tool set-up for conventional friction stir welding process.....	6
Figure 2.1 a proposed welded design solution for a wing skin panel joint of a transport aircraft. a) Conventional longitudinal stringer butt strap joint, b) Alternative welded solution	10
Figure 2.2 Fatigue crack growth regimes	12
Figure 2.3 S-N curves of base metal, FSW weld, laser weld and MIG weld for 6005Al- T5 14	
Figure 2.4 Fatigue crack growth curves for FS Wed (a) 5083-H32 and (b) 6061-T651 specimen along the BM and DXZ respectively, at R-ratio of 0.1 and 0.8 respectively.....	16
Figure 2.5 Comparison of FCGRs between WNZ, HAZ and the parent material, at R-ratio 0.33 and 0.7. FCGRs were evaluated in the as-FSW+T6 condition. Tests were conducted in laboratory air.....	17
Figure 3.1 an illustration of the FSW' process.....	20
Figure 3.2 Joint configurations for friction stir welding.....	22
Figure 3.3 Examples of the Whorl™ tool design.	24
Figure 3.4 Examples of the MX-Triflute™ (right), TriVex™ (middle) and MX-Trivex™ (left) friction Stir welding tools.	25
Figure 3.5 Schematic of friction stir welding: „a) process and „b) tool travel angle and plunge depth.....	26
Figure 3.6 FSW heat input contributions due to the shoulder (Q _S), pin lateral side (Q _P), and pin base (Q _{PB}).....	26
Figure 3.7 Schematic illustration of variations, predicted by CFD, of heat generation, peak temperatures and traversing force with rotation speed for FSW of 2024 aluminum alloy.....	29
Figure 3.8 Range of optimum FSW conditions for various tool plunge down forces for 4 mm thick ADC12 Al-Si casting alloy welded using 15 mm shoulder, 5 mm diameter, 3-9 mm long threaded pin.....	30
Figure 3.9 Regions in FSW joint	31
Figure 3.10 the microstructural zones found in demonstrated on a weld	32
Figure 3.11 Design solutions to produce T-joints by FSW	37
Figure 3.12 A schematic diagram showing dissolution and re-precipitation in age-hardenable aluminum alloys. HV denotes the Vickers hardness number.	38
Figure 3.13 Typical distribution of residual stresses across the FS welded region	42

Figure 3.14 S–N curves of base metal, FSW weld, laser weld and MIG weld for 6005Al-T5, FS welds presents fatigue strength higher than MIG and laser welds	43
Figure 4.1 Infinite plate with a central elliptical crack	49
Figure 4.2 Infinite plate with a central sharp crack	51
Figure 4.3 crack extended under fixed displacement (a), and under fixed load (b).	52
Figure 4.4 Stresses in polar co-ordinate system ahead of the crack.	55
Figure 4.5 Modes of loading: Mode I (opening), Mode II (in-plane shear) and Mode III (out-of-Plane).....	57
Figure 4.6 Hinged Model showing the simulated extended crack length at r_p accounting ..	58
Figure 4.7 Contour integral around crack tip used to define the J-integral.	60
Figure 4.8 Stage I and II of fatigue crack propagation	62
Figure 4.9 mechanisms of striation formation in the stage II of propagation: (a) no load	63
Figure 4.10 Fatigue fracture surface: (a) high applied load; (b) low applied load	64
Figure 5.1 Comparison of 2D solid fracture analysis model using enriched S-FEM (left)	70
Figure 5.2 Nodes NT and $H(x)$ improved function.....	71
Figure 5.3 Crack closure method ~two-step method, a) First step—crack closed and	77
Figure 5.4 Stress–strain curves for different regions in welded joint	84
Figure 5.5 Crack welded plate model	85
Figure 5.6 3D model of butt joint with all boundary conditions (ABAQUS model)	86
Figure 5.7 Finite Element mesh	86
Figure 5.8 Von Mises stresses at crack tip and crack opening at different steps.....	87
<i>Figure 5.9 Crack welded plate.....</i>	88
Figure 5.10 3D model of T welded joint.....	89
Figure 5.11 Finite Element mesh	89
Figure 5.12 Change of stress intensity factor vs. crack length	90
<i>Figure 5.13 Change of stress intensity factor vs. crack length.....</i>	91
Figure 5.14 Change of stress intensity factor with crack growth rate da/dN	91
Figure 5.15 Crack propagation vs. cycle number – N	92
Figure 5.16 Von Mises stresses at crack tip and crack opening at different steps.....	92
Figure 5.17 Crack welded plate	95
Figure 5.18 3D model of butt welded joint.....	95
Figure 5.19 finite element mesh.....	95
Figure 5.20 Crack welded plate	97
Figure 5.21 3D model of butt welded joint.....	97

Figure 5.22 finite element mesh.....	98
Figure 5.23 Crack welded plate	100
Figure 5.24 3D model of T welded joint.....	100
Figure 5.25 finite element mesh.....	101
Figure 5.26 Change of stress intensity factor vs. X coordinates of crack.....	102
Figure 5.27 Change of stress intensity factor with crack growth rate da/dN - right crack Tip	103
Figure 5.28 Change of stress intensity factor with crack growth rate da/dN - left crack Tip.	103
Figure 5.29 Crack propagation vs. cycle number – N	104
Figure 5.30 Von Mises stresses at crack tip and crack opening at different steps (butt welded plate)	104
Figure 5.31 Von Mises stresses at crack tip and crack opening at different steps (T welded joint plate)	105
Figure 5.32 Von Mises stresses at crack tip and crack opening at different steps double T welded joint plate).....	105
Figure 5.33 Change of stress intensity factor vs. X coordinates of crack.....	111
Figure 5.34 Change of stress intensity factor vs. X coordinates of crack.....	111
Figure 5.35 Change of stress intensity factor vs. X coordinates of crack.....	112
Figure 5.36 Crack propagation vs. cycle number – N	112
Figure 5.37 Change of stress intensity factor with crack growth rate da/dN	113
Figure 5.38 Change of stress intensity factor with crack growth rate da/dN	113
Figure 6.1 The experimental setup: 1) Test machine, 2) Cameras, 3) Light source, 4) Specimen	116
Figure 6.2 Characteristic regions in friction stir welded joint of AA 2024-T351, [12].....	117
Figure 6.3 Stress–strain curves for different regions in welded joint	117
Figure 6.4 Configuration of the T-joints.....	119
Figure 6.5 Three Point Bending specimen made of T Joint	119
Figure 6.6 Fatigue crack growth equipment	119
Figure 6.7 Scheme of measuring foil for fatigue crack growth monitoring	120
Figure 6.8 Finite Element boundary conditions.....	122
Figure 6.9 Finite Element mesh	122
Figure 6.10 Crack propagation vs. cycle number – N, a) comparison between experimental and numerical data.....	124
Figure 6.11 Change of stress intensity factor vs. crack length	125

Figure 6.12 Change of crack growth rate and stress intensity factor	125
Figure 6.13 Crack length and Von Mises stress for different crack growth steps (0, 10, 20, 25)	126

1 Introduction

1.1 Introduction

The need to design new commercial aircrafts that will replace the existing ones at the end of their design life to increase the world aircraft fleet that will grow in the next twenty years, has forced the aerospace International Community to investigate the possibility of obtaining more structures that are efficient in the cost and / or weight reduction field, with the same or better safety levels than the actual ones. Introducing new aircraft structures, cost and weight savings pursued with an integrated design.

The aerospace industry uses riveting as a fastening technology to join the aircraft panels of fuselage, wings and vertical and horizontal stabilizers.

Nowadays, many manufacturing industries use welding as an extremely strong application to allow both structural efficiency and reducing the cost.

This process of joining has a combination action of both heat and pressure in which materials are enabled to form metallurgical bonds.

Development and improvement of different fusion welding techniques have been taken a place for several decades, which lead to reduce in weight and increase in performance in the continuous manufacturing targets. Most of these techniques include tungsten inert gas, metal inert gas, laser welding, ultrasonic welding, arc welding, plasma welding and friction welding require the material to be melted and fused together in order to form the final weld.

The large-scale use of these welding techniques for joining of aerospace structures has long being inhibited by the difficulty of production of Aluminum alloys welds with high fatigue strength. [13]

A non-fusion solid phase welding process, which heat generated by friction is used to create high-integrity joint between similar or dissimilar metals, called friction stir welding (FSW). This technique was invented by W. Thomas and his colleagues at The Welding Institute (TWI), UK, in 1991. [11]

There are many different aluminum alloys such as 2xxx and 7xxx series are typically classified to be un-weldable by conventional welding techniques. Therefore, Friction stir welding is well suited for joining such alloys. [12]

The main advantages of this technique are: 1) capability to weld difficult-to-weld aluminum alloys, 2) less defects of weld 3) improve strength of the welded structure and different shape of weld including linear and curved welding are obtained.

The tensile properties and fracture locations of the joints are largely dependent on the welding defects and hardness distributions of the joints, and which, in turn, on the welding parameters [6].

Different joints can be produced by FSW such as T-joint, butt joint, lap joint, corner joint, spot joint and fillet joints. In addition, the technique has the ability to join similar and dissimilar metals like aluminum, copper, steels, titanium, magnesium and their alloys. FSW can also be used to weld hollow objects, such as tanks and pipes [8-10]

Crack-like defects or flaws that presented in manufacturing process, mainly in case of welding, or form early during service exist in many engineering materials and structures. Nowadays, numerous studies were conducted on fatigue strength of Friction stir welded 2024 Al-T351, 2024 Al-T3 and 7050 Al-T7451 joints.

The main following observations are resulted from these studies. First, the fatigue strength of the base material is much greater than the FSW joint that because the FSW joints are prone to fatigue crack initiation. Second, fatigue strength of the conventional fusion welding as MIG and laser welds joints is lower than the FSW joints.

Most aircraft structures are prone to cyclic fatigue loading during their service. Therefore, it is very important to determine and control of both fatigue crack initiation and growth.

Fracture mechanics provides the tools for an initial crack to reach a critical length to predict a fatigue life of the structure, with an existing crack and dimension of defects that present in the structure when introduced into service to calculate the strength remains in the material.

There are four different FSW regimes for each joint. These joint regimes have different fracture mechanics parameters.

In general, several locations can allow fatigue cracks to begin and most of these locations are around the regions of the weld in the joints and the discontinuities areas, all that results from high bending, residual stresses and weld notch stresses.

Single crack can be eventually formed and grows in different direction longitudinally and accidentally throughout the whole structure which may finally become a through thickness crack.

However, the test results of analytical fracture surface evaluation are not enough. This dissertation describes the test results of fatigue crack growth to clarify the characteristics of fatigue crack growth in FS Welded T Joint of the plate.

Numerical analysis was based on the Linear Elastic Fracture Mechanics (LEFM) theory. Finite element analysis, with the model being subjected to cyclic loading and a non-linear solution method was used to evaluate the fracture mechanics parameters like Stress Intensity Factor (SIF), this is the basis on which fatigue life prediction scheme has been modeled. Crack propagation phenomenon has been used to predict the fatigue life of the welded T joint. The versatility of FEA can be used to predict the fatigue life of different kinds of joints in future. In order to analyze fatigue crack growth in an integrated system of analysis. Present model has been developed to simulate crack in friction stir welded T joint made of aluminum alloy in three dimensions by Extended Finite element method using ABAQUS a fracture mechanics software package necessary to be able to estimate both plastic collapse and fracture strengths of the critical members containing defects.

1.2 Research Requirements and Objectives

In according to friction stir welding, it was increasing and widely used in currently to join the engineering materials in many applications including automotive body, railway components, ship, aerospace parts, nuclear and military applications [1, 3] as shown in Table 1.1 and Table 1.2 due to the joint properties overcome the conventional fusion welding [1, 3-4]. In order to understanding and preventing fatigue of failure, mechanism occurred in the structural and vehicle components, which these parts are prone to fatigue failure. Fatigue crack growth behavior of these parts was required to study in case of materials that easy to deform and initiate crack in early stage during service or contain defects or flaws from manufacturing process.

Table 1.1 Applications and type of aluminum where FSW has been used in automotive industry [3].

aluminum alloy in auto industry	
Inner and outer body panels	2008,2010,2036,3004,5052,5192,5754,6009,6010,6016,6022,6111
General structural components	6005,6005A,6009,6061
Extrusions	6063,6082,7005
Luggage racks, air deflectors	6463
Spare tire carrier parts	6061
Bumper components & Ace bars	5052,6009
Reinforcements	6009,6061,7003,7004,7021,7029
Brackets	6009,7021
Seats & Shells	7036,6010
Headrest bars	7116,7129
Tracks	6010,5182,5754,6009
Load floors	2036, 5182,5754,6009
Wheels	5454,6061,A356.0
Suspension components	6061 (forging)
Drive shaft composites	6061 (tube), aluminium metal matrix
Engine mounts	5454,5754
Sub-frames & engine cradles	5454,5754,6061,6063
Radiator tubes & fins	3003,3005
Condenser tubes	3102
Condenser fins	7072

Table 1.2 Applications of FSW in aerospace industry [3].

products	Strength levels	Alloy/temper	Applications
Sheet	Damage tolerant	2024-T3, 2524-T3/351	Fuselage/pressure cabin skins
Plate	Damage tolerant	2024-T351, 2324-T39, 2624-T351, 2624-T39	Lower wing covers
	Medium strength	2024-T62	Tactical aircraft fuselage panels
	Medium strength	2124-T851	Tactical aircraft bulkheads
	Medium strength	7050-T7451, 7X75-T7XXX	Internal fuselage structures
	High strength	7150-T7751, 7055-T7751, 7055-T7951, 7255-T7951	Upper wing covers
	Medium strength	7050-T7451	Spars, ribs, other internal structures
Forgings	High strength	7175-T7351, 7050-T7452	Wing/fuselage attachments
Extrusions	Damage tolerant	2024-T3511, 2026-T3511, 2024-T4312, 6110-T6511	Lower wing stringers Fuselage/pressure cabin stringers
	Medium/high strength	7075-T73511, 7075-T79511, 7150-T6511, 7175-T79511, 7055-T77511, 7055-T79511	Fuselage stringers and frames, upper wing stringers, floor beams, seat rails

Currently, studying fatigue crack growth behavior of FSWed joints was limited and has contradiction in trend as discussed in literature review. Moreover, in previous study was almost investigated the behavior of fatigue crack growth of conventional friction stir welding which FSW tool insert into joining material plates on one side. Even through, the conventional friction stir welded joint was better tensile and fatigue properties compared to conventional fusion welding as mentioned in earlier. However, there are reported that kissing bond or root flaws generating at the bottom part of conventional friction stir welded joint and affected to decrease fatigue properties of the joint as shown in Figure 1.1 and Figure 1.2 [19]. Moreover, conventional friction stir welding required highly constrained to fix the joining material plates during welding process as shown in Figure 1.3 [20].

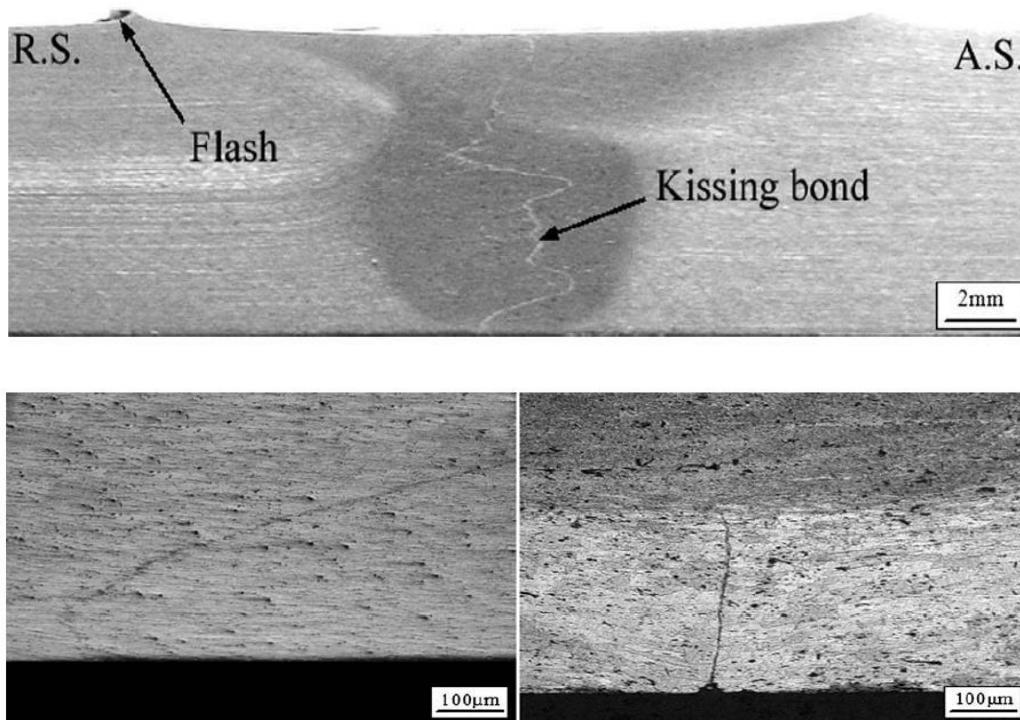


Figure 1.1 Optical micrograph of kissing bond and root flaw in conventional FSW joint

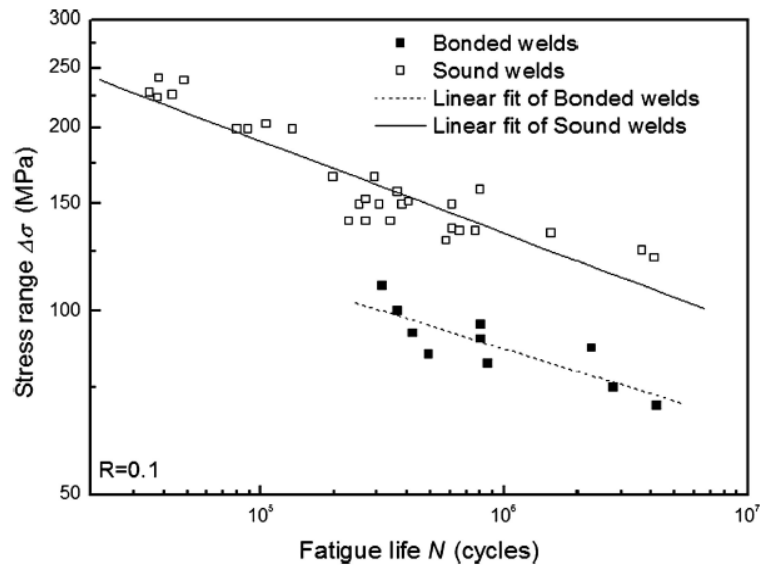


Figure 1.2 S-N curves of flaws (bonded) and sound conventional FSW joint

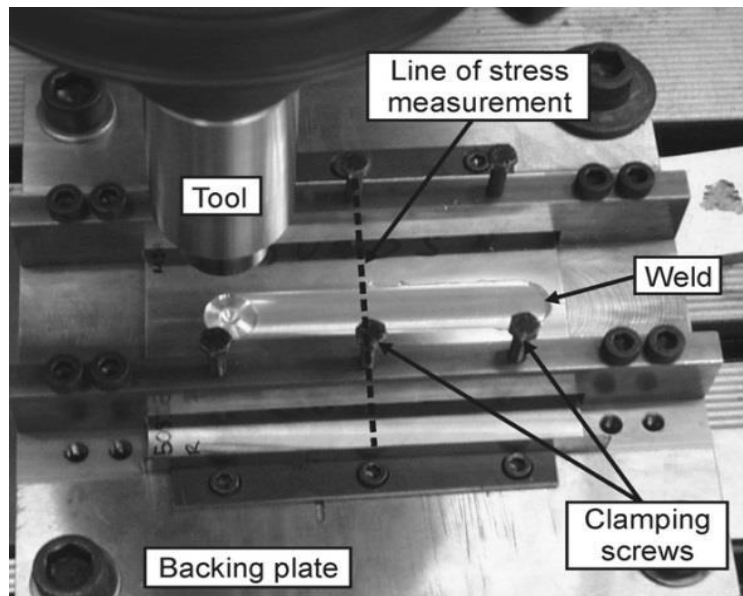


Figure 1.3 Tool set-up for conventional friction stir welding process

1.3 Thesis Outline

This research is divided into 7 chapters, which look at achieving the above objectives; the details of each chapter are given below:

- **Chapter 1:** Introducing the importance of welded joint plates.
- **Chapter 2:** presenting and reviewing the literature of aluminum alloys and their properties with different welded joint plate

-
- **Chapter 3:** In this chapter, the fundamental science behind FSW is covered. This includes, heat generation during friction stir welded joints made of aluminum alloys [AA2024], different friction stir welding zones, advantages and drawbacks of FS welded joint made of [AA2024].
 - **Chapter 4:** In this chapter a detailed description of fracture mechanics concepts, fatigue crack growth and fatigue life of aircraft structures
 - **Chapter 5:** This chapter deals with numerical simulation, i.e. application of extended finite element method using ABAQUS software and Morfeo
 - **Chapter 6:** In chapter, numerical results obtained will be compared with experimental results for T joint, with an appropriate discussion.
 - **Chapter 7:** This chapter concludes the Contribution of the candidate in the study.

2 Literature Reviews

Fatigue properties play an important role in mechanical structure. The significance of such properties become more critical in applications like transport vehicles, platforms, aerospace structures and bridge constructions. The critical impact of such properties makes its study important in engineering arena. Friction Stir welding technique covers a wide range of engineering applications. The research investigation of exploring the characteristics of welded aluminum aerospace structures has increased through time. Researchers are investing time to evaluate the fatigue behavior of FSW joints and study fatigue crack growth behavior. [6-9].

2.1 Aluminum-Copper-Magnesium Alloys

The hardening element incorporated in 2xxx series alloys is copper. In order to enhance tensile strength and natural aging magnesium is added to meet the requirements. The distinctive properties for such alloys include poor corrosion resistance, high strength with very low extrudability (typical extrusion speeds are as low as (1/6 m/min) and weldability is relatively poor for fusion techniques. Such alloys (Aluminum-Copper-Magnesium Alloys) primarily find their application in aerospace structures. Lightweight and toughness make aluminum alloys compatible for aerospace applications. Aluminum copper alloy Al-2024 is high aircraft quality being applied in formation of aircraft skins, cowls, and aircraft structures. Since it possesses shiny finish, it is also used in repair and restoration and aerospace applications. Combination of low density, high specific modulus, excellent fatigue resistance, and cryogenic properties make it feasible for aerospace applications. Heavy load acts on the aerospace application during takeoff, landing, supersonic speed maneuvering, and an extraordinarily high gravitational force, for structure comes under heavy stress in such conditions. The wings are subjected to heavy stress due to cyclic loading and shock load in extreme circumstances. Since welding operation is not facile in all conditions, it makes riveting more appropriate alternative. In aircraft structure a novel method, known as FSW is applied to weld aluminum alloys, which assist in building the structures of aircrafts.

2.2 Design of welded aluminum aerospace structures

The application of welded structural is relatively old, and finds its origin in 1920s, but it does not provide ample information or data of approach and methodologies used in welded aerospace structure.

The governing mechanical properties for the welded joints and fastened joints are different. Rivet joints have substantial potential to bear shear load. The simple butt-welded joint is different from riveted joints in dealing with stress concentrations, secondary bending moments and edge overlapping. The design requirements vary because of distinctive behavior of joints. The evident solution for the problem seems to be the replacement of welds joint with riveted joints, but such approach is not regarded as an efficient methodology. The degradation properties induced in welds differs from riveting. The material selection plays a critical role in minimizing the degradation process occurs due to welding process. For such reasons, exhaustive studies have been carried out to make material selection process more facile. The method provides an insight in selecting the appropriate material so that weight of the welded component can be minimized. The studies also suggest the application of panel-structures approach in design of welded airframes. As per these studies, the welded structural panels are supposed to be in flat form. The panels are then molded to achieve the desirable geometrical accuracy and heat treated (if possible). Eventually assembly process will be carried out to integrate individual panels. The strategy helps in reducing the residual stresses and makes the automation process of welding more facile. The application of fillet-welded joints used previous method, which increases design flexibility. However, the fatigue strength and inspect-ability for fillet-welded joints is generally lower than butt-welded joints. [2, 3]

British Aerospace Airbus has carried out a comprehensive study on friction stir welded aircraft structures and their corresponding benefits. The method applies welding which tends to reduce fastened joints, so that we may get decrement in manufacturing costs and achieve weight savings. In general applications fastened wings use skin panels that are typically jointed in the span-wise direction via a butt strap joint incorporating a stringer as shown in Figure 2.1. Such approach helps in eradicating the sealant film and butt strap. A span-wise butt weld is used to integrate the skin panels, which lies away from other

geometric stress concentration features, such as bolted and riveted stringers. Consequently, joint durability will improve.

There have been number of researchers who vigilantly looked after FSW, and Boeing was one of them. Boeing started its investigation in 1997, through the Phantom Works project, and effectively substantiated FSW for aircraft structural parts, military and aerospace applications. Since August 1999, market is equipped with such applications, such as the Delta II and Delta IV fuel tanks, along with the Boeing C-17 cargo ramp and in Boeing 747-8 freighter barrier beam. In November 2010, it has been acknowledged by Bolse that Boeing has produced more than 8,900 meters of friction stir weld without defects, especially for Delta rockets, which successfully executed 73 mission using welded tanks. The approach is mainly concerned with space applications, albeit the several FSW applications have been developed which ensures safety of critical structure, demanding high reliability. NASA worked in close association with Lockheed Martin, replacing the joining process in the Space Shuttle External Tank from variable polarity plasma arc (VPPA) to friction stir welding. The shift was desired to provide high reliability in joints and high strength.

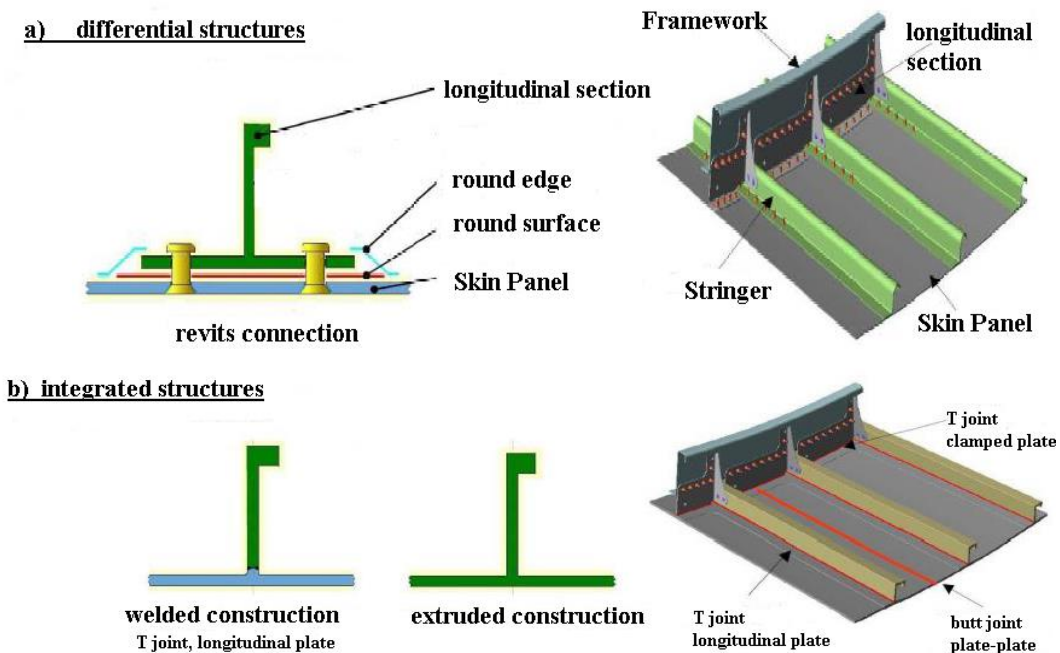


Figure 2.1 A proposed welded design solution for a wing skin panel joint of a transport aircraft. a) Conventional longitudinal stringer butt strap joint, b) Alternative welded solution

2.3 Friction stir welding of T-joints

The T-joint is a type of geometry, effective in increasing the inertia and strength of thin skins or plates. It does not cause any increment in the weight, which is regarded as an important factor in transport structures. The general structure of the joint consists of joining the web (the vertical element) with the flange or plate (horizontal element). In applications where specific weight of the structure is critically important, such as fuselages, reinforcement of aircraft, ships, trains and many other applications, the geometry can be applied to extract desirable effects. The geometry can be obtained by using the process of extrusion, although the dimensions attained by using such process are limited. The approach meets its limitations when dealing with large reinforced panels, which covers the path for the application of other methods such as riveting or adhesive bonding. Hence, in order to acquire such geometry, FSW is an important method as compared to other traditional methods. Few studies exist that substantiate the application of FSW in production of T-joints. The article of Erbsloh et al., explains the study of T-joints in aluminum alloy AA6013-T4 and 4 mm thick plates. Plunging the tool through the skin and the stiffener, the implications of the shape of backing plates in the T corners was analyzed. Conventionally, the T-joints are welded by orienting the web element in tangential to the frame and carrying out the welding operation in two corners of the T. It is worth noting that such approach does not comply with FSW, if special machining is available to produce a flat tangential surface along the weld line. In order to cater such problem, the weld may be produced with the shoulder tangential to the upper surface of the frame element, and the probe crossing the frame, with partial penetration of the web and mixing the materials to get the both parts integrated.

2.3.1 Fatigue properties in FSW aluminum alloys

A key assumption in the use of linear elastic fracture mechanics when applied to fatigue (and indeed any fracture process) is that similitude applies. Similitude occurs when the crack tip conditions can be uniquely defined by the stress intensity factor. It does not strictly take into account any load history effects, and/or the effects of crack closure. Figure 2.2 is a plot of typical data of crack growth rate, as conventionally plotted against ΔK , where $\Delta K = K_{max} - K_{min}$ (K_{max} is the maximum applied stress intensity factor and K_{min} is the minimum applied stress intensity factor). The graph shows three

distinct regions of crack growth. There is a notional linear portion of the growth curve in region II. The growth in this region is described by the well know Paris Law:

$$\frac{da}{dN} = C \Delta K^m$$

Where C and m are both scaling constants dependent on material, microstructure, loading frequency, testing environment, and R - ratio (i.e. K_{min}/K_{max})

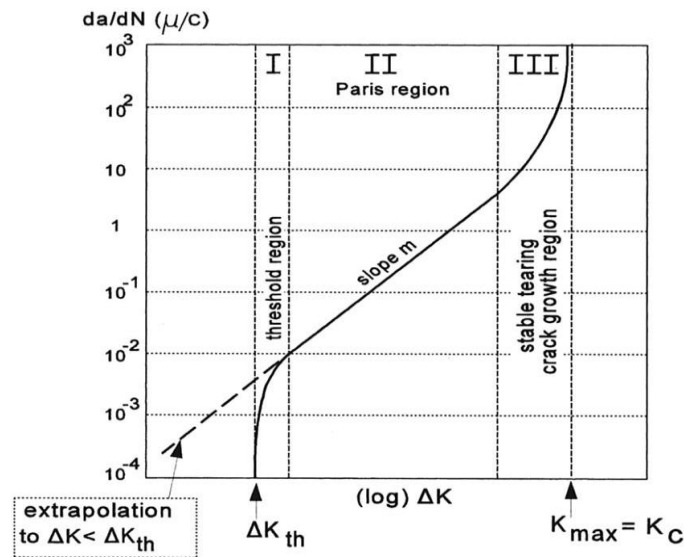


Figure 2.2 Fatigue crack growth regimes

From Figure 2.2. It may also be seen that there is a threshold value in region (I) where the crack driving force (i.e. ΔK) falls below a critical value for growth to occur. It is also evident that the growth rate accelerates towards K_{crit} (the "cyclic" fracture toughness) in region III.

The researchers have carried out several investigations on the fatigue strength of FS Welded joints, such as Welded 6006Al-T5 [8,9], 2024Al-T351 [10], 2024Al-T3 [6], 2219Al-T8751 [13] and 2519Al-T87 [7] joints. The implications of the study are as follows. The analysis made its evident that the fatigue strength of the FSW joint was lower than the base material for crack initiation is more likely in FSW joints [11-13]. Bussu and Irving [17] investigated that the fatigue strength for the transverse FSW specimens is lower than in the longitudinal FSW specimens. However, FSW joint shows higher strength than the conventional fusion welding as MIG and laser welds [9, 10]. S-N curves

for FSW joint, laser weld, MIG weld, and the base metal of 6005Al-T5 are shown in Figure 2.3. The basic reason behind effectiveness of FSW welds is their finer and uniform microstructure, than the fusion (laser and MIG) welds. In addition, the surface quality poses an important impact on the fatigue strength of the welds. Hori et al [8] showed the impact of tool speed on the fatigue strength, concluding decrement in the fatigue strength with increment in tool traverse speed/rotation rate (v/ω), due to increase of non-welded groove on the root side of the weld. Albeit observed that by skimming the non-welded groove, the fatigue strength of the FSW weld does not experience any change with changing (v/ω) ratio. Bussu and Irving [10] reported that skimming 0.5 mm thick layer from both root and top sides that eliminated all the profile irregularities resulted in the fatigue strength (for both transverse and longitudinal) of FSW specimens comparable to the base metal. The observations suggest the dependence of fatigue strength on crack nucleation, that actually limits it, and inherent defects or internal flaws are not likely to be present in successful FSW welds joints. The impact posed by FSW parameters on fatigue strength is convoluted and it has been found that the behavior is uncertain. Hori et al. [8] reported that for a specific (v/ω) ratio, the fatigue strength of the FSW weld does not change with the tool travelling speed. However, Biallas et al. [6] explains his observation by stating that for a constant (v/ω) ratio, the fatigue strength of FSW 2024Al-T3 welds with thickness of 1.6 and 4 mm was substantially enhanced with increment in tool rotation rate and travelling speed.

When 1.6 mm thick FSW weld was made at high tool rotation of 2400 rpm and travelling speed of 240 mm/min, fatigue strength was found to be same as the base metal. Subsequent operations, such as low plasticity burnishing (LPB) can increase the fatigue life of the FSW joints. Jayaraman et al. reported that LPB enhanced the high cycle fatigue endurance of aluminum alloy FSW 2219Al-T8751 by 80%, which is a result of introduction of a deep surface layer of compressive residual stress. Additionally, a highly polished surface will be attained due to LPB, and as noted earlier the FSW shows constrain of limited fatigue life due to surface crack nucleation. The two important parameters involved in desirable fatigue properties include compressive residual stresses at surface and high-quality surface finish. It should be note that the fatigue resistance of FSW specimens in air is found to be lower than the corresponding base material. Pao et al. [7] reported that the fatigue lives and fatigue threshold for FSW 2519Al-T87 and base

material specimens is identical in 3.5% NaCl solution. Certainly, the products of corrosion will pose an impact on fatigue crack nucleation.

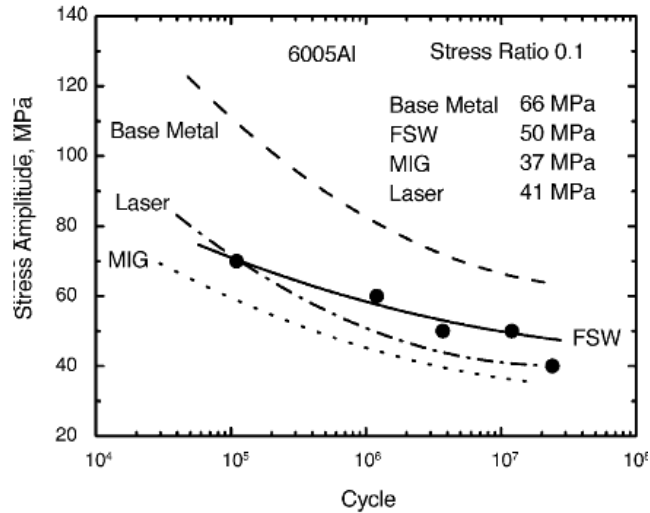


Figure 2.3 S-N curves of base metal, FSW weld, laser weld and MIG weld for 6005Al- T5

2.3.2 Fatigue crack growth behavior in FSW aluminum alloys

The behavior of fatigue crack growth has been a focus of attention for researchers. The investigations explored the impact of FSW on crack growth behavior [14-18]. The following explanation illustrates the investigation regarding impact of FSW on FCG. Donne et al. [15] studied the implications of weld and residual stresses by considering the fatigue crack growth in FSW 2024Al-T3 and 6013Al-T6 welds, using compact tension specimen. The study shows that the quality of the FSW welds can influence the behavior of fatigue crack growth to a limited extent. . When the value of ΔK will be low and R-ratio of 0.1, the resistance showed by FSW is superior to the base metal, whereas for high values of ΔK and higher R-ratios of 0.7-0.8, the FCG behavior of both the materials will be identical. Compressive residual stresses at the crack tip region are considered responsible for such behavior in the FSW welds, which causes decrement in the effective range of stress intensity factor (ΔK_{eff}) at the crack front. In this case, reduction in effective range of stress intensity factor is causing the FCG rate to be reduced at low ΔK and low R-ratio. Since the impact of compressive residual stress becomes insignificant at high ΔK and higher R-ratio, it makes the resistance of fatigue crack growth of base material and FSW identical. Donne et al. [15] observed that the $da/dN - \Delta K$ curves and FSW welds overlapped if the effect of residual stresses had been subtracted. Third

specimen geometry showed substantial effect on the FCG behavior of the FSW welds. Donne et al. [15] drew a parallel between the FCG curves obtained by specimens having compact tension and those having middle cracked tension for both base material and FSW weld at low R-ratio of 0.1. A sharp difference was observed in the case of FSW welds with overlapping of the curves of base materials. Such behavior is caused due to asymmetric distribution of residual stresses in different specimen possessing different geometry.

The enhancement in FCG resistance after FSW was investigated in FSW 2519Al-T87, 2024Al-T351 5083-H32 and 6061-T651 by Pao et al. [7], Bussu and Irving [17] and S. Kim et al. [18] respectively. Pao et al. [7] reported that the nugget zone and HAZ of FSW 2519Al-T87 showed lower fatigue crack growth rate and higher fatigue crack growth threshold, ΔK_{th} , at both $R=0.1$ and 0.5 , in air and in 3.5% NaCl solution, compared to the base material. Moreover, the nugget zone exhibited higher FCG resistance as compared to HAZ. The FCG rate in 3.5% NaCl solution for the base material, HAZ, and nugget zone, in the intermediate and high ΔK regions were found to be two times greater than the one showed in air. However, with the value of crack growth rate of 10^{-8} m/cycle, ΔK_{th} values in 3.5% NaCl solution were found to be higher than in the air. The fact can be rationalized by considering the corrosion product wedging that became increasingly dominant and corrosion product induced crack closure decreased the effective range of stress intensity factor, with eventual stoppage of crack growth. Bussu and Irving [17] reported that the crack growth behavior in the FSW 2024Al-T351 joints experienced major influence of weld residual stress and the impact of microstructure and hardness change was trivial. Moreover, their study concluded that their orientation with respect to centerline has considerable effect on the FCG rate in FSW 2024Al-T351. Although, in FSW weld that were mechanically stress relieved, with the application of 2% plastic strain, crack growth rate did not exhibit any distinctive behavior to those of the base material, irrespective of location and orientation. S. Kim et al. [18] also reported that WNZ of FS Wed 5083-H32 and 6061-T651 joints showed higher FCG resistance than FCG resistance in the BM as shown in Figure 2.4. It was suggested that compressive residual stress in WNZ caused a decrement in effective range of stress intensity factor, (ΔK_{eff}) and consequently causing reduction in FCG rate.

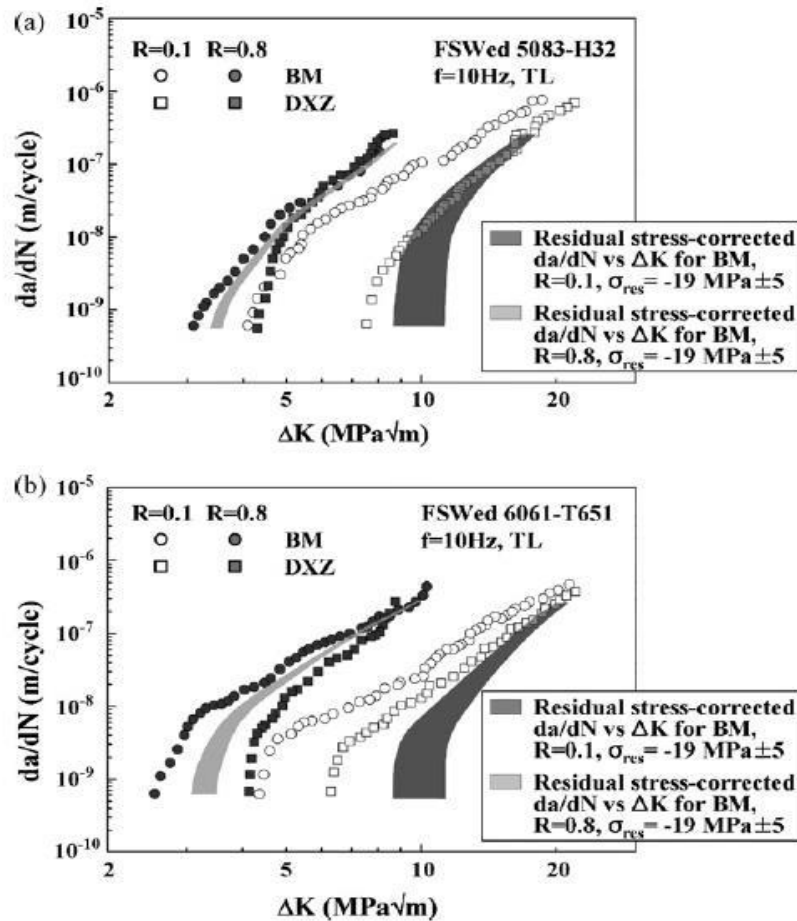


Figure 2.4 Fatigue crack growth curves for FS Wed (a) 5083-H32 and (b) 6061-T651 specimen along the BM and DXZ respectively, at R-ratio of 0.1 and 0.8 respectively

Paradoxically, in an investigation focusing the fatigue crack growth behavior of FSW 7050Al-T7451 in the as-FSW + T6 condition at lower stress ratio of 0.33, Jata et al. [14] observed highest near-threshold FCG resistance for HAZ, while lowest for the nugget zone as shown in Figure 2.5. When FCG rate was considered at higher stress ratio of 0.7, an insignificant difference was observed amid base material, nugget zone and HAZ. They suggested that an intergranular failure mechanism (fracture that grows along the grain boundaries of the material) was responsible for the decrement in the FCG resistance of the nugget zone. In HAZ, the residual stresses had a significant influence than the microstructure, eventually enhancing the FCG resistance. Similarly, Pao et al. [16] found that the HAZ of FSW 7050Al-T7451 in the as-FSW + aged (121°C/12 h) condition showed significantly lower FCG and much higher, ΔK_{th} at a stress ratio of 0.1 in both air and 3.5% NaCl solution. Albeit, in both air and 3.5% NaCl solution, identical FCG resistance was observed for the weld nugget zone and the base metal. The residual stress

and roughness induced crack closure caused HAZ to have low FCG rate. Moreover, a substantial increment in ΔK_{th} values had been observed for the nugget zone, HAZ, and base material in 3.5% NaCl solution. The observation is a compliance with FSW 2519Al-T87, attributed to the corrosion product-wedging phenomenon.

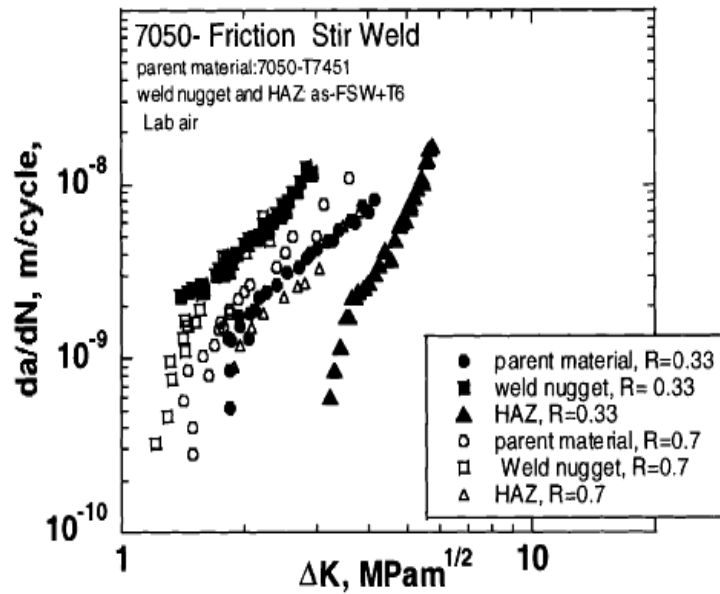


Figure 2.5 Comparison of FCGRs between WNZ, HAZ and the parent material, at R-ratio 0.33 and 0.7. FCGRs were evaluated in the as-FSW+T6 condition. Tests were conducted in laboratory air

3 Friction Stir Welding: Process Modelling and Microstructure

3.1 Introduction

The large - scale use of welding for joining of aerospace structures has long being inhibited by the difficulty of production of welds with an extremely strong fatigue and which strongly resists fracture in aerospace aluminum alloys like the extremely alloyed 2XXX and 7XXX series. In this case, these types of aluminum alloys are usually perceived as non-weldable due to limited porosity and microstructure during solidification in the fusion zone. There is also a substantial loss in the mechanical properties as related to the base material. These factors contribute to the difficulty of joining the alloys with use of the conventional processes. There is the capacity for some aluminum alloys to be resistant welded however the preparation of the surface is expensive in addition to surface oxide being a substantial issue. The Welding Institute (TWI) of UK came up with Friction Stir Welding in 1991 as a technique for joining solid state where it was first applied with aluminum alloys. The concept behind FSW can be perceived as very simple. A non-consumable tool rotates with a uniquely crafted pin with a shoulder that is pushed into the abutting edges of plates or sheets that are being joined and then traversed along the joint. The tool is meant for two fundamental functions:

- (a) Movement of material for joint production and (b) heating of the workpiece.

Friction between the tool and the workpiece influences the heating in addition to plastic deformation of the workpiece. The material around the pin is softened by localized heating in addition to the translation and rotation of the tool influences the movement of material from the front to the back of the pin. This leads to production of a joint in a solid state. Due certain geometric properties of the tool, the movement of material around the pin is usually sophisticated. A material in the FSW process goes through intense plastic deformation at very high temperatures that influences the production of fine and equiaxed recrystallization grains. Good mechanical properties are because of fine microstructure in friction stir welds.

FSW can be perceived as the most substantial development in the joining of metal over a decade in addition to being a green technology due to its versatility, friendliness to the environment and energy efficiency. In relation to the conventional welding processes, FSW can be observed to consume much less energy. There is no use of flux or cover gas that proves the process is friendly to the environment. Joining does not need the use of filler metal as with fusion welding hence cancelling out compatibility issue meaning all aluminum alloy can be joined. There is also the capacity to join dissimilar aluminum alloys if desired with equal ease. In contrast to the traditional friction welding, which is usually performed on small axisymmetric parts that can be rotated and pushed against each other to form a joint, friction stir welding has the capability to be used in different types of joints such as fillet joints, T butt joints, lap joints and butt joints.

3.2 Description of Friction Stir welding (FSW)

Aluminum alloys are applied in different structural areas where they are combined with respect to low weight and high strength. The past few years have seen substantial effort being concentrated on the use of FSW in the full-scale production of building of ships, the automotive sector and the aerospace industry. However the lack of sufficient scientific information, lack of clarity of the process, FSW has been applied in the manufacture of distinct types of weld joint configurations such as corner welds, fillet, T-sections, overlap welds and butt welds. There has been a successful friction stir weld and testing of the circumferential lap welds and longitudinal butt welds of alloy fuel tanks for space flights. The FSW process has the capacity to be utilized for three dimensional, non-linear, annular and circumferential welds. FSW is made for production of top level welds in wrought aluminum alloys the 2xxx, 5xxx, 6xxx and 7xxx series, Mg and Ti alloys, Fe alloys and thermos plastics. It also has the capacity to join dissimilar metals for thickness ranging from 0.6 to 40 mm for single sided welds and up to 75mm for the double-sided welds. Since the welding is automated, there is capacity to produce good weld quality and repeatability. The process of friction stir welding is illustrated in Figure 3.1. The tool piece comprises cylinder, called the shoulder, with a smaller diameter pin attached to the base.

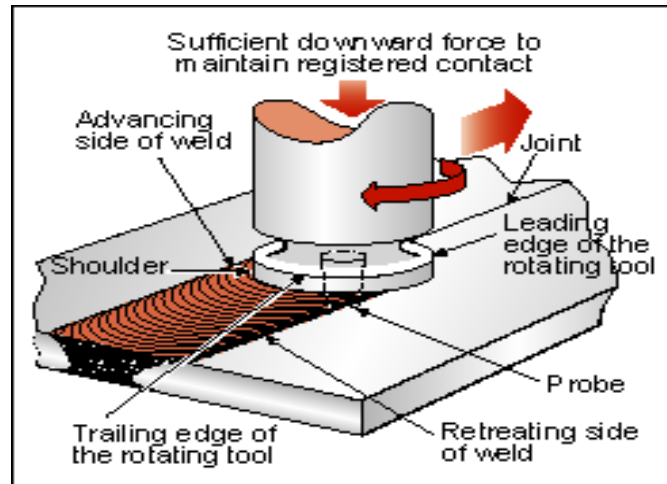


Figure 3.1 an illustration of the FSW' process

FSW involves a sophisticated means of material movement and plastic deformation. The design of the joint in addition to the welding parameters and tool geometry has a substantial effect on the flow of material and the distribution of temperature [30] [33]. Because, flow of material and the distribution of temperature influence the micro-structural of material. This section covers a few major factors that affect the FSW/FSP process such as the geometry of the tool, the design of the joint and the welding parameters. Very high temperatures are achieved during FSW this is attributed to the intense plastic deformation that occurs around the rotating tool. This is also due to the friction happening between the welded material and the tool. There is an evidence that the microstructure of the weld is highly influenced by these properties with respect to grain boundaries, grain size, the shape and type of precipitates. The mechanical behavior of the weld is then influenced by the microstructure. Temperature has the capacity to rise up to 500 degrees Celsius in order to influence dissolution of the precipitates [33]. However, this is seen too much depend on the alloy since permanence and dissolution of precipitates are in the central region of the weld. The maximum temperature is to be seen at the center of the weld in addition to existence of an isothermal zone located under the pin [29]. The temperature decreases with increase of the diameter of the weld center. It is identified [33] that the rate of rotation of the tool influences the growth of temperature while the rate of heating is dependent on the speed of traversing. In addition, it is also noted that the temperature is lightly higher on the advancing side in relation to the retreating side.

The coordinative impact of movement of the tool and temperature leads to production a distinctive microstructure in the FSW fields. In the stirred zone where there is occurrence of the intense plastic deformation, there can be evidence of recrystallization and development of texture this together with coarsening (roughness) and precipitates dissolution [29] [31]. There were no substantial differences noted between the retreating and advancing side of the weld. With respect to the mechanical characteristics of the weld, it is essential to consider both the solid hardened and precipitation hardened aluminum alloy. It is also noted that the center region of the weld is not as hard as the base of the alloys. This behavior has been connected to the dissolution and coarsening of the precipitates because of high temperatures produces during FSW [29] In this case there is no observation of reduction of hardness of the weld in solution hardened aluminum alloys. No very significant differences were observed between the advancing and the retreating side of the weld.

The use of FSW enables the increase in the strength of fatigue, lighter structure and is cost saving. The initial industrial application of FSW had the capacity to join hollow aluminum panels for the use in deep freezing fish. The combination of helpful features in FSW means it is being preferred for welding long lengths of material in railway industries, shipbuilding in marine, aerospace and aircraft industries (Al-2xxx). FSW has been noted to replace the fusion welding in automotive industry during the production of light alloy wheels, suspension parts and tailored blanks. There is also the capability to weld sophisticated curve shapes. Figure 3.2 introduces the joint configurations produced by Friction Stir Welding (FSW).

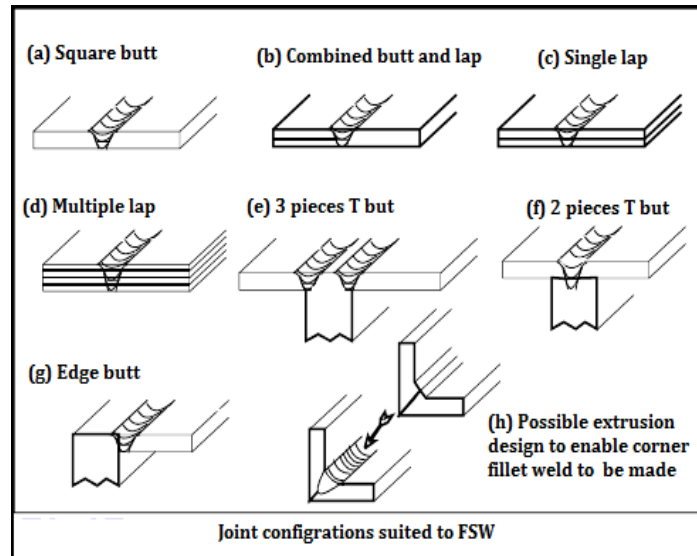


Figure 3.2 Joint configurations for friction stir welding

3.2.1 Important welding parameters

The importance of friction stir welding process is to study different number of variables that the welding process and the properties of the joint can be influenced. For instance, tool rotation and traverse speeds, tool design, and tool tilt angle with plunge depth.

3.2.1.1 Tool rotation and traverse speeds

There are basically two speeds of tool that are used in friction stir welding; one is about how fast the tool can rotate and second is about how quickly tool traverses the interface. Both the tools have their own significance and thus, each should be considered after highly critical analysis. This is important mainly so that welding cycle can be successfully completed with efficient results. It is also said that for a hotter weld, either traverse speed should be decreased or rotation speed should be increased. A successful weld is only possible if there is a hot material in the surrounding area. The material should be hot enough so that plastic can flow extensively and any other forces that act on the tools can be minimized. In the other case, where the material is not hot enough, it is possible that there may be flaws in the stir zone or tool may break even in worse cases. Excessively high heat input is also considered detrimental for the properties of weld. All these demands lead to the processing window where a complete range of parameters is present to show how a weld can be made of a good quality. The weld that will be made in this window will have a significantly higher heat input that may assure adequate material plasticity. However, this will not affect the weld properties, but it is clearly visible that a

good weld is difficult to make. Furthermore, a high quality weld can be made even if there are large tensile residual stress field defects, or it shows mechanical performance that is unsatisfactory. In certain conditions, there might be questions regarding economic choice of process through which weld has been made. According to these requirements, it is possible that there can be different processing windows that can be used for different systems such as tool, alloy and others; in which some compromises should be made to produce a quality weld. Some complicated situations may include different welds where different alloys are present, which may have different processing windows with various ranges of welding speeds, but the only possible and successful weld will be the one that has overlapping processing windows. The ratio of traverse and rotation speed has been reported by numerous authors or researchers who have also highlighted properties of friction stir welds. This ratio is also known as weld pitch, which is number of rotations per mm travelled reciprocal. In this work, the weld pitch is defined as:

$$Weld\ pitch = \frac{traverse}{rotation} \left(\frac{mm}{rev} \right) \quad 3-1$$

The weld pitch is also known as an idea that diminishes two parameters and results in a single factor. This helps in simplifying the reporting data. Weld pitch is also considered an important parameter but it is too complex to consider that the relationship between heat input and tool speed can be narrowed down to single parameter.

3.2.1.2 Tool design

Tool's design is considered a critical factor since a good tool can be useful in improving maximum possible speed of welding as well as quality of weld. The most basic consideration in tool design is the material from which it has to be made, which are numerous and should be considered wisely in order to make a successful tool. A tool material that has tough, strong and hardwearing properties is always desirable, mainly at high temperatures. Along with these properties, it is also important that the tool material should have low thermal conductivity and good oxidation resistance to minimize damages due to heat loss and thermal energy. AISI H13, hot worked tool, is considered perfect for welding 0.5 to 50 mm thick aluminum alloys. However, for any further demanding applications such as higher melting point materials like titanium and steel or highly

abrasive metal matrix composites, advanced tool materials are required. Further considerations are required in the design of pin and shoulder. Improvements in design have also proved that there are substantial improvement with respect to quality and productivity. According to Threadgill [25], who analyzed TWI group's tool design, showed that if a profiled pin is modified into the design, traverse speed is increased by hundred percent while the weld is of good quality. As summarized by Threadgill [25], the TWI group also successfully welded plate thickness; 'whorl' design can be taken for example, where re-entrant featured, tapered pin is used or a pitch thread of variable type is used that helps and improve downward material flow. Figure 3.3 illustrated tool design examples of Whorl™.

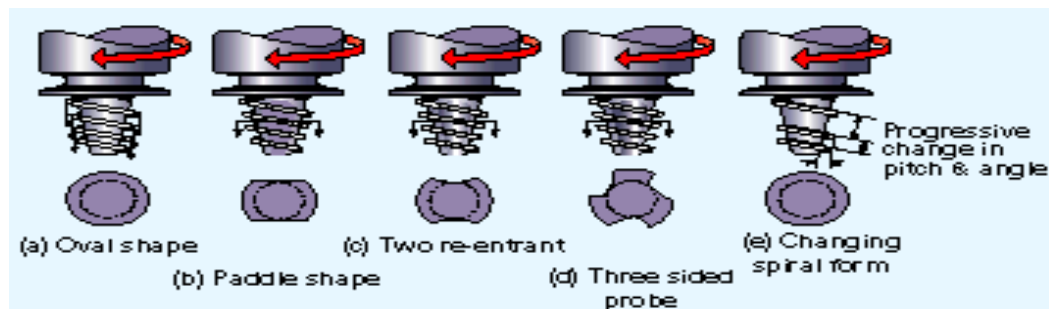


Figure 3.3 Examples of the Whorl™ tool design.

Many additional designs tools including Triflute™, Trivex™ and MX-Trivex™ tools are shown in (Figure 3.4). The Triflute design has a complex system of three tapering, threaded re-entrant flutes that appear to increase material movement around the tool (TWI 2000). The Trivex tools have been found to reduce the forces acting on the tool during welding and, in addition, they offer a much simpler design than the Triflute, which may be an important property if tools are to be made from very high strength materials [32]. The shoulder has also been subject to design improvements. The Triflute tool has a series of concentric grooves machined into the surface that are intended to produce additional movement of material in the upper layers of the weld. The Trivex tools have a concave shoulder profile that acts as an escape volume for the material displaced by the pin prevents material from extruding out of the sides of the shoulder and maintains downwards pressure and hence good forging of the material behind the tool.

NASA has made an improvement on a retractable pin design which, allows the welding of components of variable thickness and prevents exit holes by the gradual retraction of the pin towards the end of the weld.



Figure 3.4 Examples of the MX-Triflute™ (right), TriVex™ (middle) and MX-Trivex™ (left) friction stir welding tools.

3.2.1.3 Tool tilt and plunge depth

Depth of the lowest point of shoulder that is below welded plate's surface is known as the plunge depth. This depth is also considered a critical parameter that tells whether a weld is of high quality or low. In another case where pressure is increased below the tool is because plunging is done below the surface of plate that also helps in forging material at tool's tile rear. This forging process is known to be assisted if the tool is tilted by 2 to 4° and the rear part of tool is brought lower than the front. For this purpose, necessary downward pressure has to be achieved which is achieved through setting plunge depth properly. This also tells whether the tools fully penetrated in the weld or not. It should also be kept in mind that flaws can be generated in weld if the plunge depth is reduced due to supportive structure and deflection of friction stir welder. Conversely, pin rubbing on backing plate surface can be experienced if plunge depth is done excessively. For this reason, changes in tool displacement have to be automatically compensated, which can be done through developed variable load welders. Figure 3.5 shows the Schematic of friction stir welding process and tool travel angle with plunge depth.

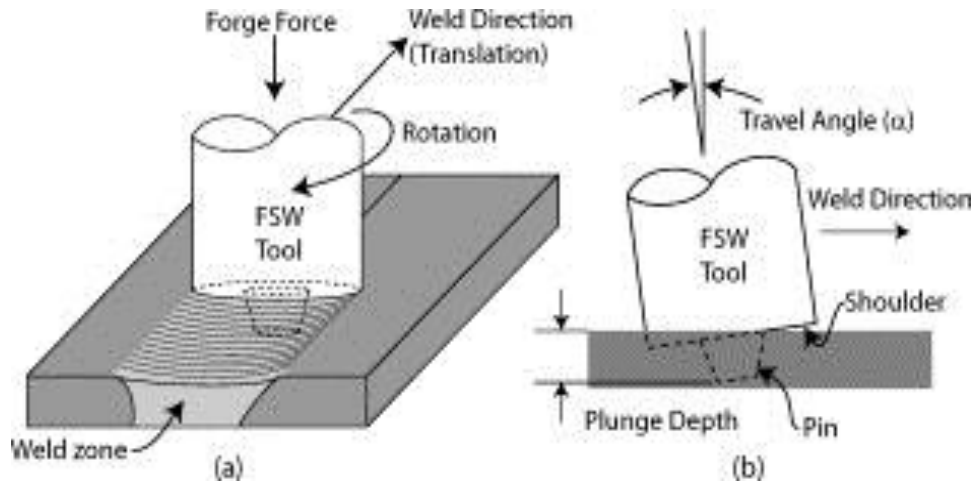


Figure 3.5 Schematic of friction stir welding: „a) process and „b) tool travel angle and plunge depth

3.2.2 Heat generations during Friction Stir welding

The heat input was divided into three contributions (Figure 3.6): a) the tool shoulder, Q_S (a flat annulus in contact with the work-piece surface), b) the tool pin lateral surface, Q_P (cylindrical or conical pin, regardless of the threading geometry or any re-entrant features), and the pin flat base, Q_{pb} . The total heat input (Q_{total}) is thus given as:

$$Q_{total} = Q_S + Q_P + Q_{pb} \quad 3-2$$

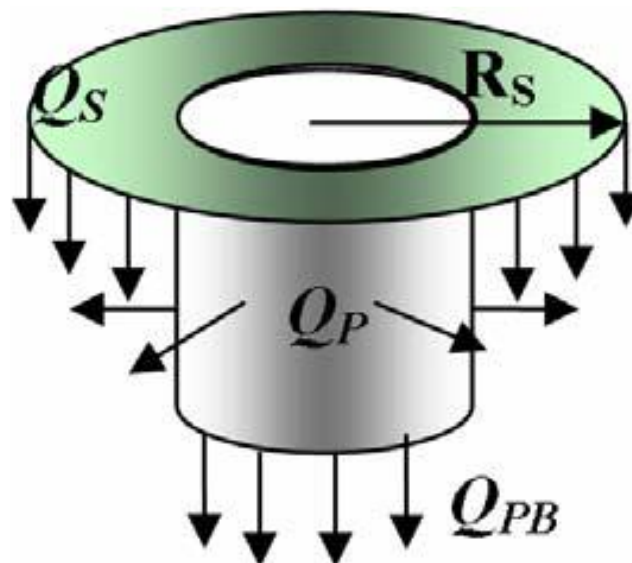


Figure 3.6 FSW heat input contributions due to the shoulder (Q_S), pin lateral side (Q_P), and pin base (Q_{PB})

The FSW heat generation can result from the friction of the ‘slipping’ tool over the work-piece [6-8], or from the adiabatic-deformation of the material sticking to the tool [9, 10]. Although it is now believed that the latter case is the dominant condition [31, 32], the proposed algorithm considers both scenarios. A subroutine is included in the code to adjust the contact condition at the tool/welded metal interface based on Coulomb’s friction law.

If the rotational work by the slipping tool shoulder over the metal surface is converted to frictional heat generation, the shoulder heat input can be expressed as [28]:

$$Q_s = \frac{2\pi}{3} \mu P \omega (R_s^3 - R_p^3) \quad 3-3$$

where P is the pressure experienced under the tool shoulder:

$$P = \frac{F_N}{A_s} = \frac{F_N}{\pi(R_s^2 - R_p^2)} \quad 3-4$$

The change from the friction-induced (slip) to the deformation-induced (stick) condition is governed by the modified Coulomb’s friction law. As stated by this law [33], the friction shear stress (μP) due to the contact normal pressure (P) at a given temperature has a maximum limit value $\tau_{max}(T)$, which is constant regardless of any increase in P . This maximum value is the limit of the sticking friction, and it starts when μP exceeds $\tau_{max}(T)$. In this case, μP will be replaced in equation (3.3) by $\tau_{max}(T)$, which is related to the material ultimate strength σ_{UTS} by (based on the Von Mises criterion between the yield stress in shear and yield stress in tension [33]):

$$\tau_{max} = \frac{\sigma_{UTS}}{\sqrt{3}} \quad 3-5$$

The friction coefficient will be estimated during the fitting stage using the torque and normal force measurements during FSW, using the approach followed by Schmidt and Hattel [29], based on the torque-based model by Khandkar et al. [34]. This approach will also provide an estimate for the average shear stress (τ_{max}), which can be also used to rationalize the dominant contact condition (slip or stick).

Due to the stirring action by the pin, its heat generation will always be deformation-induced.

The heat input of the pin lateral surface and base can be added together, such that:

$$Q_p = \frac{2\pi}{3} \tau \omega (3H_p R_p^3 + R_p^3) \quad 3-6$$

3.2.2.1 Heat generations during Friction Stir welding of aluminum alloy (2024)

The effects of the energy input produced during FSW on the resulting microstructure and mechanical properties have to be considered here for the 2xxx alloys, since over-aging and dissolution of second phase particles can take place.

Viscous dissipation that occurs in workpiece material is usually the main reason for heat production near the tool. A single contact condition is usually invalid since normal contact stresses and temperature is variable over the tool. At the interface, there is a possibility that the material sticks, slips or may be in form of this combination. At the solidus temperature, local melting may occur, which show oscillating stick slip behavior mainly because a significant reduction is seen in shear stress. This eventually leads to a steep drop in self-stabilizing behavior, temperature and local heat input. Sensitivities of heat generation are explored through process modeling software called (Computational Fluid Dynamics) CFD, which also helps in exploring size of deformation, and tool forces as a function of process conditions and tool design. Alloy's deformation constitutive response is usually helpful in determining heat input through a fully coupled heat flow and deformation model. This model does not show work or does not work with respect to the constitutive data, especially near solidus; however, this model can help in identifying deformation regime correspondent to the sound welds production. This may have least weight of machine for each alloy. Taking an example of variation of power generation (Figure 3.7) prediction, where traverse force and peak temperature as well as rotation speed are identified. Through rapid material softening, peak temperature and power saturates due to limited generation of interface heat and temperature. It is also recorded that minimum force is required for intermediate rotation speed. This phenomenon is actually related to early work of Russians, like Vill, who showed that if rotation speed is increased, time for rotary friction weld is reduced to a minimum. This has also been

checked by TWI group and they have showed that plate and alloy thickness have specific operator's remaining process variables such as tool plunge, tool tilt angle, down force, traverse speed and rotation speed. Plunge depth is considered to be a position control preset while down force is force control's preset variable. A process window is defined that is capable of producing sound welds without macroscopic defects and tool breakage through empirical trials that explore variable matrix.

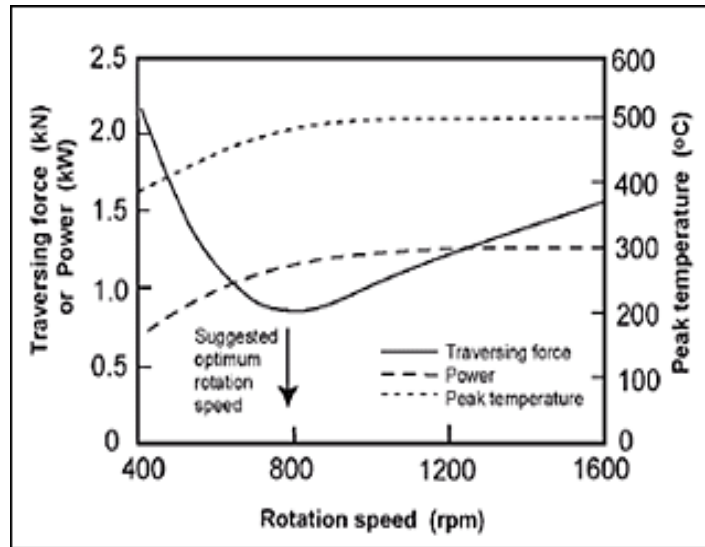


Figure 3.7 Schematic illustration of variations, predicted by CFD, of heat generation, peak temperatures and traversing force with rotation speed for FSW of 2024 aluminum alloy

Figure 3.8 introduces the welding parameters relationship with FSW process window for an aluminum die-casting alloy. By lowering the rotation speeds and increasing the welding (traverse) speeds, the process window is mainly enlarged with an increasing of tool down force. This pattern is broadly typical of aluminum alloys generally. The process operating window is commonly described as being limited by 'hot welds' and 'cold welds' - the former associated with high rotation and low traverse speeds, leading to excessive flash production, the latter with low rotation and high traverse speeds, leading to tool breakages.

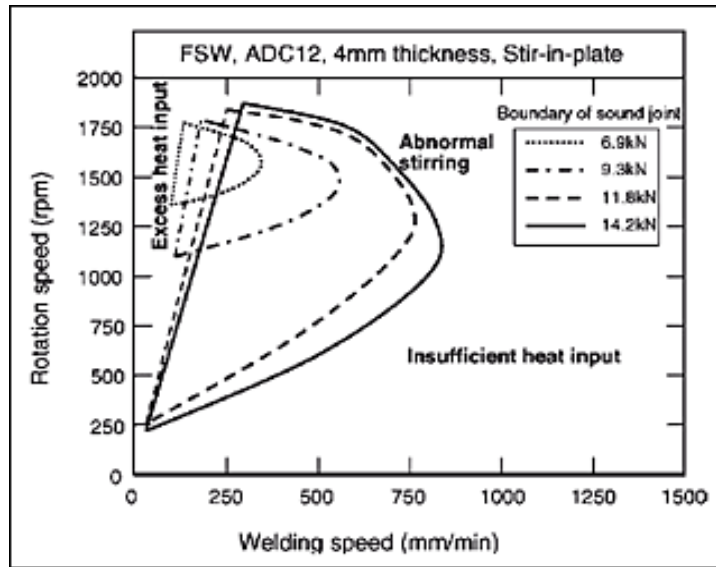


Figure 3.8 Range of optimum FSW conditions for various tool plunge down forces for 4 mm thick ADC12 Al-Si casting alloy welded using 15 mm shoulder, 5 mm diameter, 3.9 mm long threaded pin

3.2.3 Microstructure modification

There is a possibility of discerning four distinct zones, which are the nugget that corresponds to the parent zone (base material or unaffected material), the heat affected zone (HAZ), the thermal mechanically affected zone (TMAZ) and the dynamically recrystallized zone (Nugget). The microstructure of FSW is dependent on the process parameters, such as tool geometry, rotation/travelling speeds, applied pressure and on the alloy properties. FSW is progressed by a complex action of plastic deformation and heat generation due to the direct friction between the rotating tool and the workpieces. The thermomechanical process leads to the recovery, dynamic recrystallization and redistribution of precipitates at the weldment. HAZ and parent alloy have similar grain structures. Deformed grains characterize TMAZ edges, while TMAZ center is featured with equiaxed-recrystallized grains. HAZ exhibits coarse second phase particles because of the heating and cooling cycles. The various microstructural regions found in FSW are shown in Figure 3.9 below.

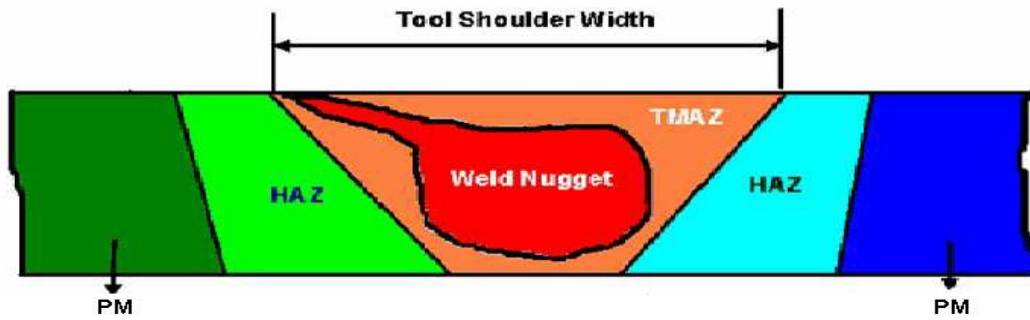


Figure 3.9 Regions in FSW joint

3.2.3.1 Parent material (unaffected material)

Parent material, as the name suggests, is the original material that has not been significantly affected by the FSW process either mechanically or thermally. It should essentially purposes the same as the material that existed before the weld. However, due to the high conductivity of aluminum, it is inevitable that the parent material will experience some additional heat increase, but this is not significant enough to alter its mechanical properties or microstructure.

3.2.3.2 The heat affected zone (HAZ or thermally affected)

The HAZ is another zone at the base of the metal that undergoes intense temperature from the heat generated during plastic deformation in the TMAZ (Thermo Mechanically Affected Zone) and nugget zones [33]. The substantial increase of temperature in the HAZ has the capacity to induce precipitation and coarsening with a negative impact on the technical characteristics. This can be attributed to the fact that residual stresses are reduced by recrystallization that is higher between the heat-affected zone and the mechanical stressed zone. This can also be attributed to the potent mechanical restraints that are required for FSW [23]

3.2.3.3 The thermo-mechanically affected zone (TMAZ)

The transition between the base of the metal and the nugget is referred to as TMAZ. In this situation, deformation happens instead of recrystallization to enable observation of elongated grains with a pattern following the flow of the metal as influenced by the movement of the tool. This zone is also characterized by high temperature to allow for observation of dissolution of precipitates.

3.2.3.4 The dynamically recrystallized zone (Nugget)

The nugget zone is in the recrystallized zone characterized with a fine grain structure in addition to a shape that is dependent on the alloy type and the geometry of the tool and the processing parameters. Usually, the nugget is characterized by the shape of an ellipse or a wide glacial valley [33]. The microstructure usually looks like fine equiaxed grains of the size of a few microns. This is regardless of whether the sub-micrometric grains will be generated with use of specialized means or by instantly cooling the plate after the weld [31]. The various microstructural zones and precipitates in the nugget zone have an option of being dissolved or coarsen with respect to the composition of the alloy and the temperature are shown in Figure 3.10.

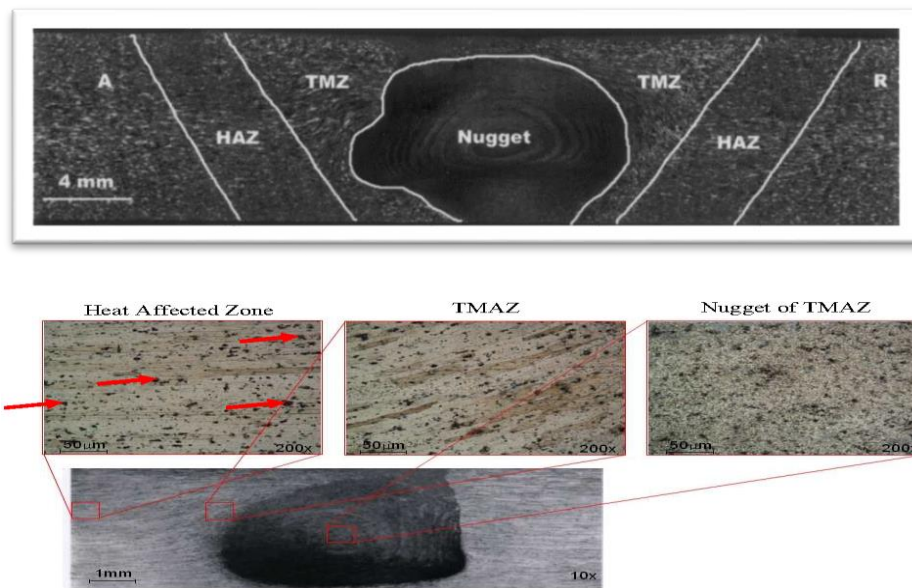


Figure 3.10 the microstructural zones found in demonstrated on a weld

3.3 Advantages and drawbacks of Friction Stir welding

In relation to conventional welding, FSW has several advantages such as free from dangerous electromagnetic radiation, low distortion, no emission of UV, good mechanical properties and specially the capacity to join extreme strong aluminum alloys like the 2000 series. FSW can be industrially applied in shipbuilding, railways and aerospace. This is in addition to panel joining, fuselage and wing manufacturing and the construction of high-speed trains.

There are also several advantages such as minimization of hot cracks, production of porosity, inclusions, low fatigue strength and distortion due to the low temperature of

welding with relation to the melting point of the alloy. There is less shrinkage and distortion observable in FSW in relation to conventional weld technology. The forging, stirring and crushing action of the FSW tool produce a weld with a finer microstructure in relation to the original material. This provides laps and butt joints with a favorable mechanical characteristic. A number of other potential advantages of FSW over conventional fusion welding processes have been identified

- (1) - Low distortion, even in long welds.
- (2) - Excellent mechanical properties as proven by tensile and bend tests
- (3) - One tool can typically be used for up to 1000m of weld length in 6000 series aluminum alloys
- (4) - It is a process that can be easily automated which makes it perfect for industrial use.
- (5) - It has the capacity to operate in unlimited positions since weld pools are not present.
- (6) - It has a generally good-looking weld in appearance in addition to minimal thickness which reduces the need for expensive for post welding.
- (7) - It has a low impact on the environment.

The FSW process has also be known to possess several potential disadvantages.

- (i) Welding speeds are moderately slower than those of some fusion welding processes (up to 750mm/min for welding 5mm thick 6000 series aluminum alloy on commercially available machines)
- (ii) Weld plates must be rigidly clamped
- (iii) Backing bar required to counter to the downward force.
- (iv) Leaving an exit hole in the material when the tool is removed.
- (v) During the welding of materials with different weakness, there is need for tools with different pin lengths in order to avoid defects in the roots.
- (vi) FSW has the capacity to indicate some asymmetry in the weld since existence of tool rotation could influence defects like surface breaking grooves,

wormholes or voids that are known to go along the region of the weld where the tool and welding is in the same direction. A distinct pressure is caused by this process asymmetry around the pin that causes the rotating tool to veer away from the retreating side. Some of other disadvantages identified include:

- (1) - There are also difficulties with variations in the thickness and welds that are nonlinear. In relation to the manual and arc processes, it can be seen as less flexible.
- (2) - It also exhibits a slower transverse rate in relation to some fusion techniques although it may be offset if there is need for fewer welding passes.

3.4 Friction Stir Welding (FSW) of T joints

The fusion welding operations, for instance, MIG or laser welding have been employed in the past era to perform the welding of T geometries. The high temperature values basically describe these procedures and material melting temperatures are surpassed by such values, due to which distortion and residual stress states are affected, which must be controlled verifying and securing the proper stress and geometrical based attributes of the final assembled part. Moreover, the impact of the fusion welding operations on the T-joints has been investigated by many authors and for curtailing both distortions and residual stresses in the welded part, the authors had tried to establish the parameters for useful processes [21–24]. Literature witnesses some FEM based applications, the purpose of whom is to emphasize the final geometrical distortions and the residual stresses in the welded joint [25]. Additionally, T-geometries hold greater significance in various branches of the transportation industries: straightening elements is often required by components and especially panels i.e. through T-joints, on the panel surface. Robust vibrations are normally experienced by the parts produced for transportation industries and subsequently a relevant problem in their manufacturing is believed to be “fatigue resistance”. Besides the effects of the residual stresses on the fatigue behavior [28, 29], the fatigue life of welded T-joints [26, 27] has been examined by many research. Furthermore, to increase the operating life of the joints, corrosion phenomena have to be properly explored with reference to the aircraft applications where stringers and skins are welded at the same time [30]. In FSW of T-joints, we can observe that the clamped blanks

take the input of a specially designed rotating pin with a tilt angle and then it is moved all along the joint [32, 33]. Most of the time, the frictional force work is applied to obtain the heat source in FSW processes and to a degree, it is achieved by the deformation work during tool movement putting into heat along the welding line. In this manner, the most applicable process variables determining the specific thermal contribution conferred to the joint are feed rate (V_f) and the tool rotation speed (R). The local material is softened owing to generated heat flux, however no melting is observed avoiding detrimental metallurgical defects, for example, pores etc. due to which joint performance could be degraded. Sequentially, the material plastic flow gets activated by the tool movement [34,35]: the joint is to regulate an advancing side and a retreating side, the “positive” combination of the peripheral tool velocity and the tool feed rate can be used to describe the former one, while the opposite velocity vectors of rotation and feed are reported in the latter element. We observe that in the parent material of the welded blanks, some metallographic and metallurgical phenomena are established by the FSW processing conditions [36, 37]. At the core of the welding, the supposed “nugget” area is observed at the weld line where the fine area replaces the original grain and sub grain boundaries and this particular events is observed with reference to a “classic” butt joint. Moreover, a nominal dimension of a few micrometers is to describe the equiaxed-recrystallized grains. Initially, a thermo-mechanical affected zone (TMAZ) is developed all around the nugget, where both the determined thermal flux and the stirring mechanical action of the tool pin are experienced by the material. Afterwards, high temperatures reportedly generate a heat-affected zone (HAZ), which sequentially is encircled by the parent material. Most of these studies are associated with the butt joint and a few of them are linked with multifaceted geometries even though the FSW process has been analyzed by several researches in the last years. Mainly, the experts have made several probes into FSW aiming to focus its process mechanics. Additionally, from different views, the mechanical actions of the joints containing residual stress state, crack propagation in addition to static, dynamic and fatigue resistance has been examined by various studies. As a final point, researchers have examined the influence of the most applicable process parameters on the use of the obtained joint and to bring an increase in the mechanical output of the welded joints is the purpose of this study. To follow a systematic computer aided engineering of the process, the development of numerical model of FSW processes

is being recently assisted by a few research activities. Initially, based on the calculated equivalent thermal fluxes, the experts have suggested a simplified approach for thermal analyses by considering the heat generated by both the material deformation work and friction forces work [38]. Afterwards, Deng et al. had presented the finite element thermo-mechanical models for FSW. [39]. In recent times, a 3D continuum based FEM model has been recommended by the authors [40] and this new model has the potential to emphasize the FSW process mechanics and to illustrate the distribution of the key field variables, i.e. strain rate, strain and temperature factors. Selection of proper process conditions besides optimizing the tool design is the core objective of this model. It is important to note that we cannot extend the learned knowledge on FSW process of butt joints to the T-joints.

The preliminary observation is that the surface to be welded in butt joints should be vertical, whereas, it is horizontal in T-joints and it is to be positioned at the base of the top blank to be welded, namely the skin. Additionally, a proper clamping fixture is required in the FSW of T-parts so that the stringer could be fixed during the process. Two radii would be observed here to describe this type of fixture, one for each side of the joints, which is parallel to the radii between stringer and skin in the final welded part (corner-fillets). In fact, the flowing material must fill such radii during the FSW process. As a result, to force the stringer material and the sheet, an actual forging operation is required to meet the radii of the clamping fixture. Thus, the radii of the T-joint can be observed as a result. We can also say that the material flow brought by the tool must be effective so that the fixture radii could be fulfilled besides the purpose of bonding of the two blanks. When the experts choose the material of the blanks to be welded, the operative set of geometrical and operating factors improving the FSW of butt joints will not work for the T-joints. Especially, to acquire bonding conditions and an operative material flow during the FSW process, the scientists need to re-determine the tool geometries in addition to the rotating speed and tool feed rate for effective management of T-joints. The two processes have entirely dissimilar plasto-mechanics Figure 3.11.

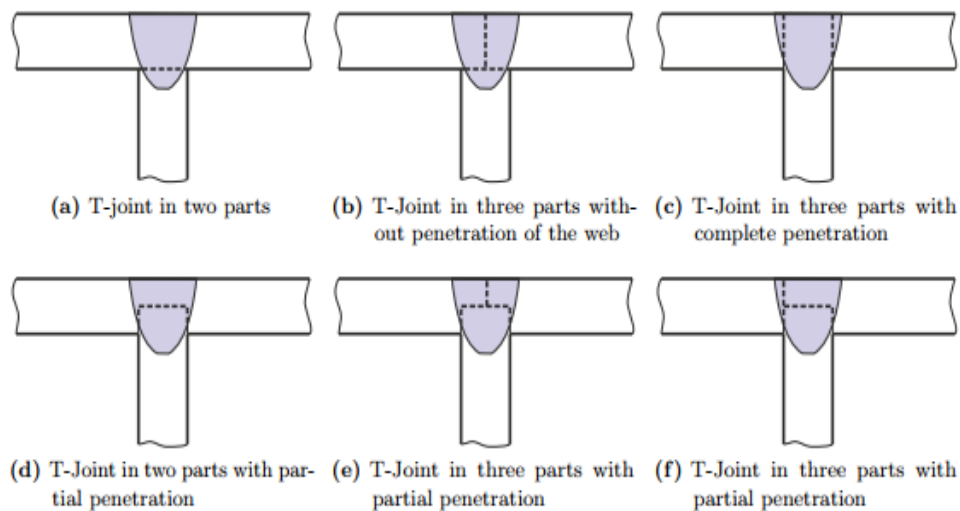


Figure 3.11 Design solutions to produce T-joints by FSW

3.5 Aluminum alloys

Aluminum alloys are widely used to replace steel in many applications, such as automotive production. Aluminum and its salts are not toxic.

Therefore, it is widely employed in food industry. One of the superior aluminum features is its good cryogenic properties. The alloys do not undergo ductile/brittle transformation or severe changes in mechanical properties, when used at low temperatures applications. The atmospheric corrosion resistance of aluminum is excellent and is attributed to a naturally air-formed surface oxide film. Aluminum components can be readily joined with various joining methods, such as bolting and riveting.

The aluminum alloys can be largely divided into two distinct categories, the wrought and cast alloys. Cast alloys will typically take the form of castings and ingots, and wrought alloys, which normally take the form of rolled plates, extrusions, and foils. Within these two main categories, two further subdivisions can be given which are the heat-treated and non-heat treated alloys. The addition of various alloying elements can add certain characteristics such as formability and corrosion resistance to the aluminum alloy. Most significantly, the wrought alloys can be broken down into a further designation system that takes into account their alloying elements, and their thermo-mechanical history, known as the wrought aluminum alloy series. Table 3.1 gives a breakdown overview of the different series.

Table 3.1 an overview of the different wrought aluminum alloy series

Alloy Series	Principle Alloying Element	Applications in Industry
1xxx	99% minimum Aluminium	Electrical and Chemical
2xxx	Copper	Aerospace
3xxx	Manganese	Architectural
4xxx	Silicon	Welding rods and brazing sheets
5xxx	Magnesium	Boat hulls, marine environments
6xxx	Magnesium and Silicon	Architectural extrusions
7xxx	Zinc	Aircraft structural components and high strength application
8xxx	Lithium, tin, and other elements	Miscellaneous components

The Al-Cu-Mg family contains the 2XXX alloys. Its robustness is increased by the addition of copper to aluminum, since; "Duralumin" was developed by Alfred Wilm at the start of the 20th century. The researchers at that time had thoroughly studied the precipitation hardening in these alloys and resultantly a considerable increase was noted in their properties. The AA2024 is the most widely used 2XXX series alloy. The precipitation hardening is carried out to make robustness in the high strength 2XXX aluminum alloys, wherein during the aging process, a fine population of precipitates is developed: suitable thermal processing can be performed to obtain the maximum values of the strength or damage tolerance. Figure 3.12, shows dissolution and re-precipitation in age-hardenable aluminum alloys.

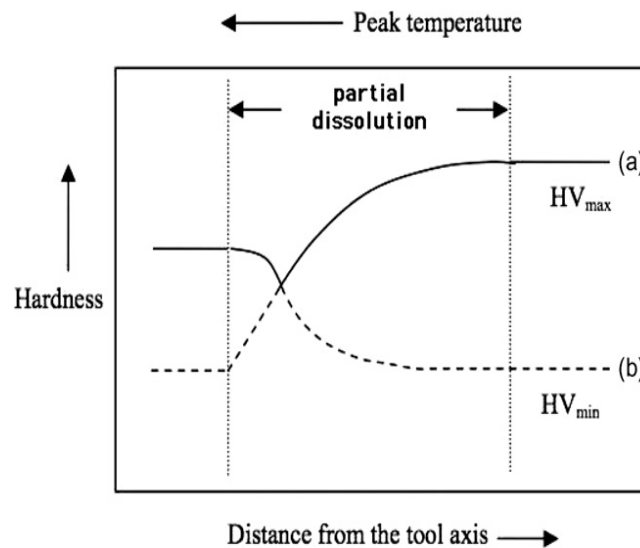


Figure 3.12 A schematic diagram showing dissolution and re-precipitation in age-hardenable aluminum alloys. HV denotes the Vickers hardness number.

During manufacture (tempers), commercial alloy products are given thermal treatments, which aim at attaining the desired mechanical and other attributes and are developed as per the outcome of these microstructural transformations. Following the letter 'T', the use of a number from 1 to 10 is prescribed by the official temper designation, namely age-hardenable aluminum alloys for specifying the thermal treatment that the alloy subjected to the T7 temper employs a supplementary number, so that the specific type of treatment (e.g. T79 or T76) could be specified. Furthermore, a tensile stretching operation is represented by the presence of the digits 'S 1' at the end of a temper designation and after quenching, this particular operation can be directly performed so that the residual stresses could be decreased and the mechanical characteristics in some cases could be enhanced. The T851 or T351 are among the examples [13]. For all tempers, quenching and solution heat treatment are common and an action at high temperature (about 450-550°C) is usually recommended by the experts so that the soluble alloying elements in solid solution could be disseminated and the microstructure could be brought to 'freeze' state.

Natural aging + T3 solution treatment + cold working + quench

Quench + T4 solution treatment + natural aging

Cold working + quench + T8 solution treatment + artificial aging (to peak strength)

T3 temper often features the 2XXX alloys, since, a good mixture of damage tolerance and strength is displayed by this condition regardless of not attaining peak hardness. When there is especially high yield strength for the application, the temper T8 features the 2XXX alloys. Nonetheless, the damage tolerance is penalized by this mechanism. Moreover, as per the most critical design parameters, different aircraft structures are to use different alloys.

Table 3.2 The various sub-divisions of tempers

Temper Designation	Process
T1	Naturally aged after cooling from an elevated temperature shaping process, such as extruding
T2	Cold worked after cooling from an elevated temperature shaping process and then naturally aged
T3	Solution heat treated, cold worked and naturally aged
T4	Solution heat treated and naturally aged
T5	Artificially aged after cooling from an elevated temperature shaping process
T6	Solution heat treated and artificially aged
T7	Solution heat treated and stabilized (overaged)
T8	Solution heat treated, cold worked and artificially aged
T9	Solution heat treated, artificially aged and cold worked
T10	Cold worked after cooling from an elevated temperature shaping process and then artificially aged

3.5.1 Joining of aluminum alloys

Most joining techniques are applicable to aluminum alloys, such as welding, mechanical joining and brazing. Mechanical joints and adhesive bonding are traditional methods, which used to join different work- pieces. Mechanical joints include riveting and bolting. The joint mechanical properties are dependent on joint design).

Welding is achieved when two different components' surfaces are joined together and become one component by complete metallurgical bonding by heating the work-pieces with or without applied stress. Fusion welding can be performed by using a filler metal, which leads to create an interface region between melted zone and bulk alloy.

Aluminum, in earlier days, suffered from limited weldability. The developments of metal inert gas (MIG) and tungsten inert gas (TIG) welding processes facilitate the welding of some of aluminum alloys. The main limitation of these techniques are the formation of porosities and hot cracking, due to both the ingress of the oxygen and the effect of excessive strain at the welding joint, which resulted from the melting and solidification sequences..

The microstructure of the weldment is modified compared to parent alloy. That also leads to changes in the mechanical properties. Welding process needs to be controlled to get optimum properties. Wrought alloys that can be joined by fusion welding are AA1xxx, AA3xxx, AA5xxx, AA6xxx and AA7xxx copper free alloys. AA5xxx alloys have better

welding properties than other alloys. AA2xxx and high strength AA7xxx alloys are difficult to be joined by fusion welding process.

For success of fusion welding, the following points need to be considered: 1) removal of oxide film, 2) avoiding oxygen ingress, achieved by injection of inert gas; and 3) applying of post-heat treatment to obtain homogenous microstructure.

3.6 Residual stress in friction stir welded aluminum alloys

During FSW process, stress is introduced because of heat generation, material deformation and variation of cooling rates at the weldment. The residual stress level is dependent on both welding process parameters and work-piece thickness. The residual stress value is less than that introduced by fusion welding. Therefore, the weld produced by the FSW experienced less distortion and is featured by better mechanical properties compared to fusion welding. The stress is relieved by applying a suitable post-weld heat treatment (PWHT).

Compressive and tensile residual stresses are important factors in fatigue assessment. In fusion welding, complex thermal and mechanical stresses are involved in the welding process and residual stresses can reach the yield strength of the base material, but in friction, stir welding residual stresses are low due to low level of heat input. Tensile residual stresses have been measured at magnitudes of 20-50% of yield strength of the base material. It is known that residual stresses in FS welds are normally higher in the longitudinal direction than in transverse (same as fusion welds). For both longitudinal and transverse directions, stresses exhibit an “M” like distribution across the weld. The peak tensile longitudinal residual stresses normally appear in the HAZ. Residual stresses in base metal or weld nugget might be compressive. Figure 3.13 shows typical distribution of residual stresses across the weld region. As can be seen, residual stresses are higher in HAZ but lower in base metal and weld nugget.

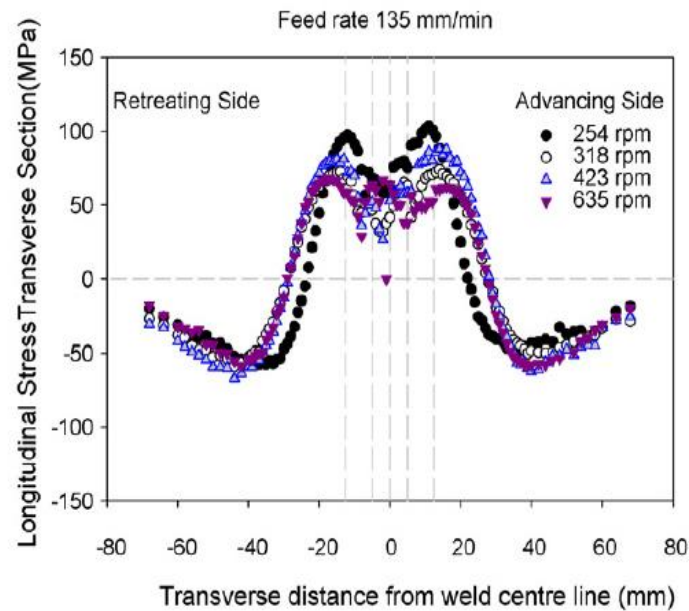


Figure 3.13 Typical distribution of residual stresses across the FS welded region

Residual stresses left after plastic deformation can influence the behavior of cracks or notches close to the weld and result in shorter fatigue life. Mahdavi Shahri and Sandström studied that residual stresses due to plastic deformation close to crack tip is resulted from fatigue failure in the weld.

Donne et al. investigated residual stress distribution through the thickness of FSW 2024Al-T3 and 6013Al-T6 welds by using different measurement techniques such as X-ray diffraction, neutron diffraction and high-energy synchrotron radiation. It was observed that residual stress distribution across the welds was similar at the top and root sides of the welds.

3.7 Fatigue properties of friction stir welds

In the past few years, several investigations have been done on stress-number of cycle (S–N) behavior and fatigue crack propagation (FCP) behavior of FS welds [35]- [39]. These studies show that fatigue strength of FS welds in general are lower than those of the base metal, i.e., the FS welds are susceptible to fatigue crack initiation, however in some cases the fatigue limit was reported comparable to those of base metal [40]. It is also observed that the fatigue strength of the FS welds is higher than fusion welds. Typical S–N curve for FS weld, laser weld, MIG weld, and base metal of 6005Al-T5 are shown

in Figure 3.14. Fine grain microstructures of FS welds contribute to the higher fatigue strength compared to fusion welds.

Several other studies were conducted to evaluate the crack propagation and fatigue threshold for friction stir welds. Ericsson and Sandström [41] showed that crack propagation rate in friction stir weld 6082 matches that of the parent material at high load ratio. Donne et al [34] reported R. Similar results for FS welds of 2024Al-T3 and 6013Al-T6. They observed that at lower loads or lower R-ratio of 0.1, the resistance to fatigue crack propagation of the

Fatigue crack growth of FS welds was higher compared to those of the base metal and at higher R-ratios of 0.7–0.8, base materials and FS welds exhibited similar propagation behavior. Other investigations [36][37] [39] showed that FS weld zone exhibited significantly lower fatigue-crack growth and much higher fatigue threshold, ΔK_{th} , at a stress ratio of 0.1 in both air and 3.5% NaCl solution compare to base metal.

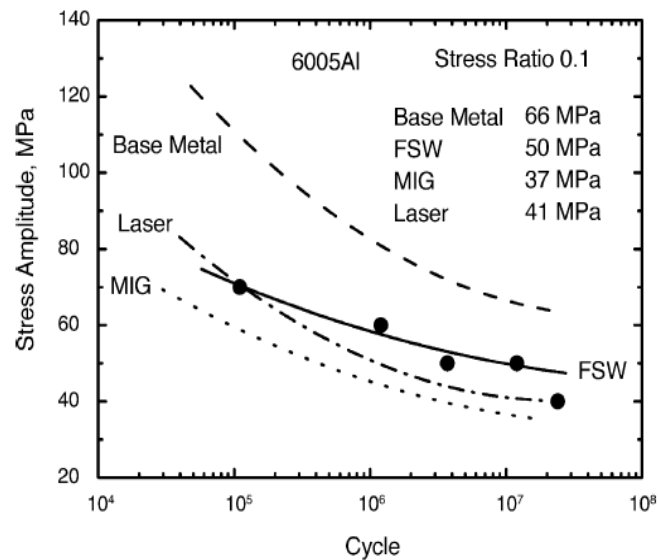


Figure 3.14 S–N curves of base metal, FSW weld, laser weld and MIG weld for 6005Al-T5, FS welds presents fatigue strength higher than MIG and laser welds

The reason for low fatigue crack growth and high threshold value compared to base metal is attributed to the presence of compressive residual stress in the weld and roughness induced crack closure. The overall good fatigue properties of friction stir welds are attributed to fine grain microstructure, the smooth appearance of the weld and low tensile residual stresses in the weld area.

3.8 Concluding Remarks

From the above finding about FSW, monitoring of this process is important and serves as an essential requirement for its application in industries that need long welded joints.

The application of the combined TIG and FSW welding procedure seems to be superior as compared to the classical FSW process alone. This hybrid of TIG and FSW welding is featured by increased output characterized by improved welding speed. Additionally, TIG-FSW welding process helps to reduce the wear-and-tear problem experienced in the welding processes by safeguarding the machine and other FSW tools used in the process.

In engineering field especially in civil engineering, the application of FSW has widely spread due to the durable and strong joints produced which is used on steels and other materials. Production of high quality and stronger steels has greatly assisted in saving costs that would be incurred in case a building or bridge collapsed. Recent advancements in friction stir welding technology have made it possible for a range of materials to be welded.

4 Fracture mechanics concepts

4.1 Introduction

This chapter first gives a brief review of the principles of fracture mechanics and micro-mechanical models employed in structural integrity assessment procedures.

The knowledge and technical mechanism between disaster and safety is referred to as the SI (Structural Integrity) [46]. For building new structures besides restoring and maintaining existing structures, it is necessary to calculate the structural integrity and remaining life of structures (e.g., ship, aircraft, pressure vessel, railways, oil and gas transmission pipelines etc.) so that the economical concern, environmental protection, public safety could be ensured. The development of structural analysis methods has witnessed considerable improvements in recent years. In the production of reliable and economical means of analysis, assessment and restoration, a unique challenge is introduced by the structural integrity of large engineering structures. A number of present structures are getting old and to keep them sustainable, it is essential to develop new technologies and new systems. A remarkable shift has been observed in the maintenance philosophy of large structure in the last twenty years [46]. Economic pressure has forced to extend the service lives of these structures beyond the design life. Life extension of these large structures has become a major growth sector in the related industries. As far as the allied industries are concerned, a major growth sector is none other than the life extension of these large structures. All aspects of industrial components and equipment, such as, structural analysis, nondestructive testing, failure analysis, fatigue and creep analysis corrosion of materials and metallurgy, software development for lifetime assessment, welding metallurgy as well as the fracture mechanics are included in the structural integrity.

The airline companies worldwide are operating several aircraft fleets, which have completed their life span and they are being operated in the environments that are believed to be more difficult than their accommodating capacity [46]. For old commercial and military aircrafts, demand on structural reliability requirements has been increased because of this condition. The assessment of structural integrity of aircraft needs following traditional works. For example, parts drawings for fabrication and installation, structural design analysis and modification, stress analysis of welded components,

external loads development, static/dynamic fatigue testing and vibration, maneuver and stress spectra development, metallurgical and structural failure analysis, full-scale and component damage tolerance testing, structural condition inspection, advanced aerospace materials studies and life extension for aircraft, application and development.

4.2 Fatigue behavior of metallic materials

Fatigue is defined as the overload, which can be observed during the happening of too many load applications simultaneously. Multiple loads do not necessarily represent the fatigue since the same load can result in fatigue, if applied continuously. In single grains of the metal, the fatigue crack nucleation entails the cyclic slipping of crystallographic planes at comparatively small cyclic loads. Without any trouble, the procedure of crystallographic plane slipping is happened and the element receives the micro-crack during this stage. As the micro-crack is developed to the extents of some grains, propagation course is perpendicular to the highest value of tensile stress. Hence, it is determined that the progress of micro-crack is controlled by the local shear stress. When the crack propagation is long enough, it leads to the fatigue failure. Some of the attributes administering the nature of fatigue of a structural element are the geometry (stress concentrations), characteristics of the material (namely static strength and microstructure) and loading (stress range, mean stress, loading history and frequency). During a constant amplitude (CA) loading, the stress (σ) varies between a maximum (σ_{max}) and a minimum (σ_{min}) value. Fatigue strength of an element subjected to CA loading is influenced by stress range $\Delta\sigma'$ and mean stress σ_m , defined as:

$$\Delta\sigma = \sigma_{max} - \sigma_{min} \quad 4-1$$

And

$$\sigma_m = \frac{\sigma_{max} + \sigma_{min}}{2} \quad 4-2$$

The influence of stress range and mean stress on fatigue can be represented by plotting the stress values versus the corresponding fatigue lives. The plot, known as an S-N curve, can be obtained for constant mean stress or constant stress ratio (R), defined as $\frac{\sigma_{mi}}{\sigma_{max}}$.

Some of the attributes of the material regulating the strength of resultant fatigue are believed to be the tensile strength and microstructure. Generally, the rigidity and strength of the material are directly proportional to the fatigue strength. We can only evaluate the fatigue limit at a basic level while the experts have demonstrated the useful connections between the tensile strength and the fatigue limit. The lower fatigue strength takes place in metals because of a granular microstructure. Through heat treatment and cold working, the microstructure and the size of the grain is transformed to raise the strength of a fatigue in metals. Since fatigue cracks are seen in aircraft structures, it is extremely important to manage and estimate the formation and development of fatigue cracks.

4.3 Fracture mechanics approach on fatigue

The more multifaceted the technological society, the more chances there are of problems like fractures occurring. Society has encountered this issue for as long as manmade constructions have existed. Cutting-edge aerospace technology is responsible for several huge crashes that may otherwise have not been possible, had it not existed. The duration (cycles) for an early crack to grow to a dangerous length can be calculated by fracture mechanics.

The first type is Linear Elastic Fracture Mechanics (LEFM). It is based on the theory of elasticity and is used as long as nonlinear deformation is limited to a small region surrounding the crack tip. LEFM is suitable for brittle materials, such as glass, ceramics, polymers and high strength steels. The second approach is Elastic-plastic Fracture Mechanics (EPFM), which can be applied to materials exhibiting non-linear behavior, e.g. aluminum, titanium and medium strength steels. EPFM is based on concepts, which assume that the stress-strain curve of the material is nonlinear.

Each type of fracture mechanics provides criteria, e.g. K, CTOD and J, which represent the driving force for crack propagation and the crack initiation is predicted to occur when the value of these parameters exceeds the resistance of the material to fracture. This section introduces the principles of LEFM and EPFM, focusing on one the parameter K

and two basic criteria CTOD and J, and shows how to employ these criteria for predicting failure in engineering structures and components.

4.3.1 Linear Elastic Fracture Mechanics (LEFM)

The local effects controlling the fatigue of welded structures are believed to be the flaws, local stress field and material characteristics. The nature and extent of fatigue crack development is calculated by the applying the LEFM (Linear Elastic Fracture Mechanics), which results in the assessments about the fatigue life of welded structures. Since, in most cases, the faulty situations of welded structures are so intense, the crack initiation stage might be ignored. While the cracks are being emerged, their development can be successfully determined by having the precise marks for the solutions of stress intensity factor. For a welded joint crack, the stress intensity factor is usually determined by the complete geometry of the joint containing the weld profile, crack geometry, loading nature and residual stress conditions [47].

4.3.1.1 Stress concentration factor

The first quantitative evidence for the stress concentration effect of flaws was provided by Inglis (1913). Inglis (1913) considered the effect of stress concentrations, focusing on an infinite plate under tensile stress σ_a , with a central elliptical crack, with semi-axes a and c as shown in Figure 4.1. The maximum stress occurs at the end of the major axis can be expressed simply as:

$$\sigma_{max} = \sigma_a \left(1 + \frac{2c}{a} \right) \quad 4-3$$

When σ_a is a remote applied stress, When $a = c$ (a circular hole) the maximum stress will occur at the edges of the hole and is three times the applied stress ($\sigma_{max} = 3\sigma_a$). The Inglis solution is particularly important because in the limit it addresses the stress distribution associated with a sharp crack ($a = 0$) when the stress concentration becomes infinite. The implication is that in a perfectly elastic plate containing a sharp crack the failure will occur at an infinitesimal small stress. It should also be noted that the stress concentration is independent of the crack length [47].

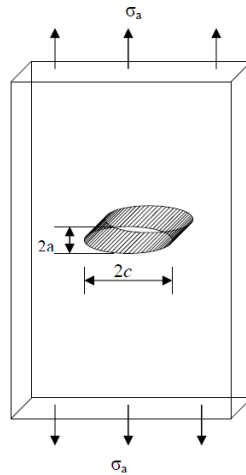


Figure 4.1 Infinite plate with a central elliptical crack

4.3.1.2 Energy balance approach

The energy balance related to the fracture of fragile materials was reflected on by Griffith in 1921 to settle the problem caused by the infinite stress concentration factor. A basic thermodynamics concept declaring that the alteration from non-equilibrium state to equilibrium is complemented by potential energy loss. This leads to the assumption that when the elastic energy was more than the surface energy necessary for the development of a new surface, crack propagation occurs.

The total energy of a system U that consists of a plate with a crack subjected to remote loading can be written (56):

$$U = U_0 + U_a + U_\gamma - W \quad 4-4$$

Where, U_0 is the total energy of the whole system without a crack, U_a is the change in the elastic energy of the plate due to the presence of the crack, U_γ is change in surface energy due to the crack, and W is work performed by the loading system during introducing the crack.

When the total energy U reaches a maximum value, the crack is no longer stable, thus:

$$dU/da < 0 \quad 4-5$$

Since U_0 is constant, then

$$\frac{d}{da} (U_a + U_\gamma - W) < 0 \quad 4-6$$

After rearranging, the equation becomes:

$$\frac{d}{da} (W - U_a) > \frac{dU_\gamma}{da} \quad 4-7$$

The potential energy Up to introduce a crack:

$$Up = U_0 + Ua - W \quad 4-8$$

$$G = \frac{-dUp}{da} = \frac{d}{da} (W - Ua) \quad 4-9$$

Where, G is the energy release rate. Substituting G , in equation (3.9), this gives:

$$\frac{-dUp}{da} > \frac{dU_\gamma}{da} = R \quad 4-10$$

This indicates that increasing the crack length by Δa leads to a decrease in the potential energy, and an increase in the surface energy.

Where, R is defined as the energy required to resist crack growth, and can be related to the energy release rate. When fracture occurs, $R = G$ and we can define G as the critical value of strain energy release, and equate this to R . Therefore, for a crack to propagate.

$$G > R \quad 4-11$$

Consider an infinite solid plate containing a center crack of length $2a$ as illustrated in Figure 4.2.

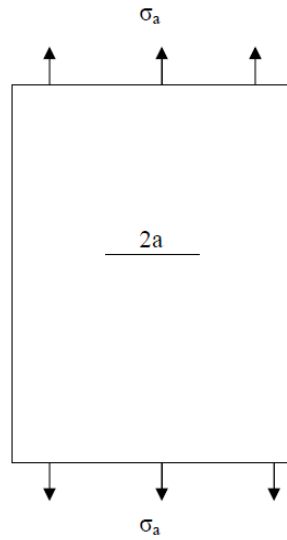


Figure 4.2 Infinite plate with a central sharp crack

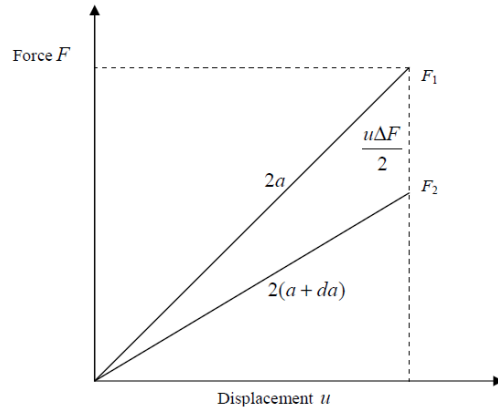
For a crack extending under fixed displacement, the force-displacement diagram is shown in Figure 4.3. The strain energy accumulated for a crack length $2a$ is:

$$U_{strain} = \frac{F_1 u}{2} \quad 4-12$$

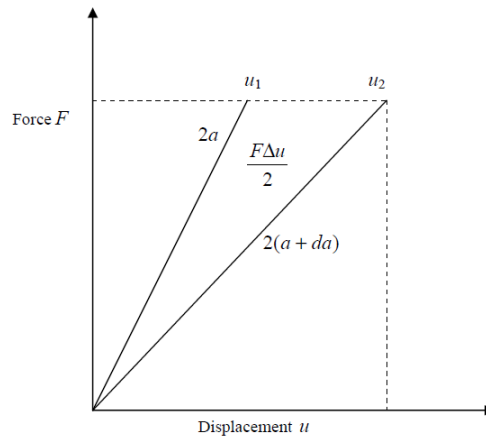
Where u is fixed displacement, and F_1 is the load corresponding to the crack length $2a$. If the same displacement is applied to a plate with a longer crack of length $2(a + da)$, the strain energy is decreased by $\frac{1}{2} \cdot u(F_1 - F_2)$, since the work (W) done by external force is zero, ($W = F \cdot \Delta u = F \cdot 0 = 0$). the whole potential energy of the system U_T is:

$$U_T = U_{strain} - W = \frac{F u}{2} \quad 4-13$$

Similar results are obtained under fixed load conditions as shown in Figure 4.3.



(a)



(b)

Figure 4.3 crack extended under fixed displacement (a), and under fixed load (b).

The work done by external force is:

$$W = Fu \quad 4-14$$

And the potential energy of the system as crack extends by da is:

$$U_T = U_{strain} - W \quad 4-15$$

$$= \frac{1}{2} Fu - Fu = -\frac{Fu}{2} \quad 4-16$$

It can be seen that the magnitude of change in potential energy is the same whether the crack is extended under fixed displacement or fixed load conditions.

Based on Inglis' (1913) results, the elastic energy released by introducing a central crack of length $2a$ can be written as:

$$U_{strain} = \pi a^2 t \frac{\sigma_a^2}{\dot{E}} \quad 4-17$$

In plane stress $\dot{E} = E$, whereas in plane strain $\dot{E} = \frac{E}{1-\nu^2}$. Here ν is Poisson's ratio and t is the thickness of the plate.

The increase in surface energy due to introducing the crack is:

$$U_{surface} = 4at\gamma_s \quad 4-18$$

Where γ_s is the surface energy of the material per unit area and $(4at)$ is the area of the two surfaces that are created by the crack.

The net change in potential energy of the system can be written as:

$$U_T = U_{surface} - U_{strain} \quad 4-19$$

$$U_T = 4at\gamma_s - \pi a^2 t \frac{\sigma_a^2}{\dot{E}} \quad 4-20$$

Based on the hypothesis that crack extension occurs when the potential energy of the system remains constant or decreases:

$$\frac{dU_T}{da} = 0 \quad 4-21$$

$$4t\gamma_s - 2\pi a t \frac{\sigma_a^2}{\dot{E}} = 0 \quad 4-22$$

The fracture criteria can now be expressed by a critical remote stress ($\sigma_a = \sigma_f$) which is a function of crack length [2]:

$$\sigma_f = \sqrt{\frac{2\gamma_s \dot{E}}{\pi a}} \quad 4-23$$

Equation 4-23 depends on the assumption that fracture occurs under perfectly elastic conditions. Irwin (1948) and Orowan (1952) argued that the fracture process occurring at the crack tip is associated with plasticity even in very brittle materials. Thus, the energy absorbed by plastic deformation γ_p must be considered, and the fracture stress can be approximated:

$$\sigma_f = \sqrt{\frac{2\dot{E} (\gamma_s + \gamma_p)}{\pi a}} \quad 4-24$$

Where, γ_p the specific surface energy associated with plastic deformation.

Irwin (1957) formalized this concept by arguing that the rate of change of potential energy characterizes crack extension. This is defined as a critical energy release rate, G_c :

$$G_c = \frac{\pi \sigma_f^2 a}{\dot{E}} \quad 4-25$$

4.3.1.3 Stress Intensity Factor

For a homogeneous linear-elastic body, the magnitude of the elastic stress field singularity is known as the SIF (Stress Intensity Factor). It is the numerical representation of applied force, crack length and specimen geometry. A detailed analysis of all the loading systems and geometric parameters must be performed first to accomplish the calculations of the stress intensity factor for weldments of any type. As far as the cracks in weldments are concerned, the two most commonly employed approaches for the evaluation of stress intensity factors are known as the FEM (finite element method) and the weight function method.

The K is a function of both stress, strain conditions of the tip of an infinitely sharp crack within an elastic material. This equation quantifies the size of the crack, the stress applied and loading mode and the structure of the component is elucidated. The mode of loading influences the stress conditions at the crack tip as shown in Figure 4.4 where Mode I loading is considered the most severe condition. The stress distribution ahead of the crack tip is related to the value of K via the Westergaard functions in Equation 4-30 and reaches

a singularity immediately at the crack tip as shown schematically in Figure 4.4. The K parameter for Mode I loading is defined by the applied stress (σ), a geometric factor (Y) and the crack-length (a) as shown in Equation 4-31.

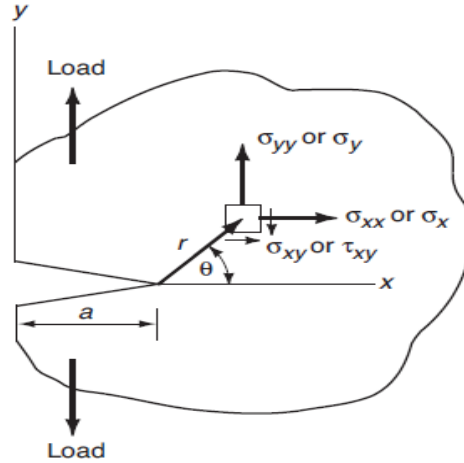


Figure 4.4 Stresses in polar co-ordinate system ahead of the crack.

$$\sigma_{XX} = \frac{\sigma \sqrt{\pi a}}{\sqrt{2\pi r}} \cos\left(\frac{\theta}{2}\right) \left[1 - \sin\left(\frac{\theta}{2}\right) \sin\left(\frac{3\theta}{2}\right)\right] \quad 4-26$$

$$\sigma_{YY} = \frac{\sigma \sqrt{\pi a}}{\sqrt{2\pi r}} \cos\left(\frac{\theta}{2}\right) \left[1 + \sin\left(\frac{\theta}{2}\right) \sin\left(\frac{3\theta}{2}\right)\right] + \dots \quad r \ll a \quad 4-27$$

$$\sigma_{ZZ} = \nu(\sigma_{XX} - \sigma_{YY}) \dots \quad 4-28$$

$$\tau_{XY} = \frac{\sigma \sqrt{\pi a}}{\sqrt{2\pi r}} \sin\left(\frac{\theta}{2}\right) \cos\left(\frac{\theta}{2}\right) \cos\left(\frac{3\theta}{2}\right) + \dots \quad 4-29$$

Where: r and θ denote the polar coordinates of the point of interest centered on the crack tip σ_{XX} ,

σ_{YY} , σ_{ZZ} = denote the direct stresses τ_{XY} = shear stress

Irwin (1957) showed that the magnitude of stress at a crack tip could be characterized by a single parameter, the stress intensity factor, K :

$$\sigma_{ij} = \frac{K}{\sqrt{2\pi r}} f_{ij}(\theta) \quad 4-30$$

The magnitude of stress intensity factor depends on sample geometry, the size and location of the crack and the level of loading, and it may be rewritten in form.

$$K_I = \sigma Y \sqrt{\pi a} \quad 4-31$$

Where Y is the dimensionless factor of geometry and loading. Stress intensity factors for many crack problems are tabulated by [16, 17].

The associated displacements (u_1, u_2) in (x_1, x_2) co-ordinate system can be written [6]:

$$u_1 = \frac{K_I}{2G} \sqrt{\frac{r}{2\pi}} \left\{ \cos \frac{\theta}{2} \left[k - 1 + 2 \sin^2 \frac{\theta}{2} \right] \right\} \quad 4-32$$

$$u_2 = \frac{K_I}{2G} \sqrt{\frac{r}{2\pi}} \left\{ \sin \frac{\theta}{2} \left[k + 1 - 2 \cos^2 \frac{\theta}{2} \right] \right\} \quad 4-33$$

Where $k = (3-4\nu)$ for plane strain and $k = (3 - \nu)/(1+\nu)$ for plane stress.

The stress field near the sharp crack is also described by Williams' (1957) asymptotic expansion:

$$\sigma_{ij} = A_{ij}(\theta)r^{-\frac{1}{2}} + B_{ij}(\theta)r^0 + C_{ij}(\theta)r^{\frac{1}{2}} \quad 4-34$$

As the distance between the crack tip and r becomes less ($r \rightarrow 0$) the leading term is in unit form, but the second term is finite, and the following high order terms in the series are negligible at the crack tip. Figure 4.5 shows the three types of loading, which can be considered on the crack. Mode I is an opening load here the load acts as the normal to the crack plane, Mode II is in-plane shear when the load is present parallel to the crack plane and perpendicular to the crack front, in this mode one crack surface slides over the other. Mode III is employed for the out-of-plane loading is associated with torsional loading or shear parallel to the crack front.

Each mode of loading produces the relation $\frac{1}{\sqrt{r}}$ singularity at the crack tip, but the proportionality constants k and f_{ij} varies with each mode. It is convenient at this to replace k by the stress intensity factor K , where $K = k\sqrt{2\pi}$. This stress intensity factor

is usually given a subscript to denote the mode of loading, i.e. K_I, K_{II} , or K_{III} . Thus, the stress fields ahead of a crack tip in an isotropic linear elastic can be written:

$$\lim_{r \rightarrow 0} \sigma_{ij}^{(I)} = \frac{K_I}{\sqrt{2\pi r}} f_{ij}^{(I)}(\theta) \quad 4-35$$

$$\lim_{r \rightarrow 0} \sigma_{ij}^{(II)} = \frac{K_{II}}{\sqrt{2\pi r}} f_{ij}^{(II)}(\theta) \quad 4-36$$

$$\lim_{r \rightarrow 0} \sigma_{ij}^{(III)} = \frac{K_{III}}{\sqrt{2\pi r}} f_{ij}^{(III)}(\theta) \quad 4-37$$

For mode I, II, and III, respectively.

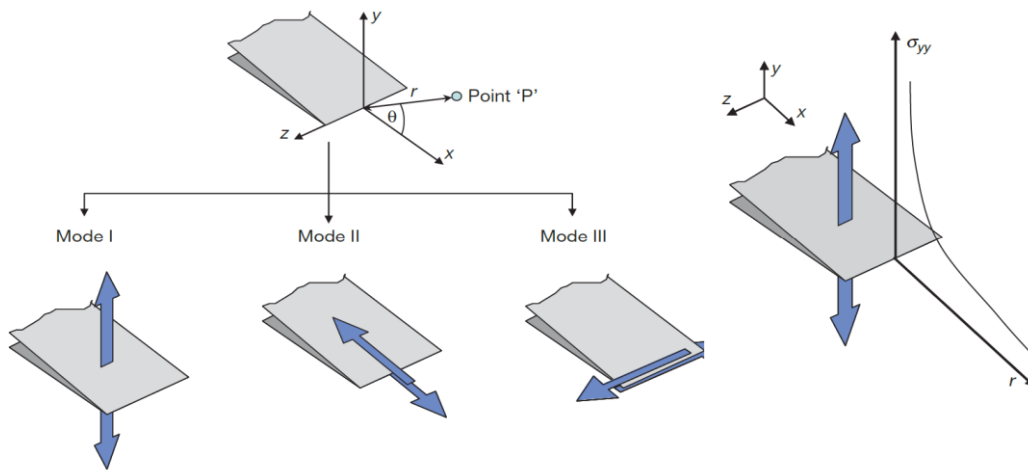


Figure 4.5 Modes of loading: Mode I (opening), Mode II (in-plane shear) and Mode III (out-of-Plane).

4.3.2 Elastic – Plastic Fracture mechanics

As soon as the plastic zone around the crack tip and other body dimensions turn out to be identical, the concept of linear elastic fracture mechanics becomes invalid. For estimating the crack tip loading, the CTOD (Crack Tip Opening Displacement) and the J-integral are used by the elastic-plastic fracture mechanics under these circumstances.

4.3.2.1 Crack-Tip Opening Displacement

The CTOD was introduced when material failure conditions could not be solely described by purely linear elastic fracture mechanics (LEFM). The infinitely sharp crack-tip dampens and gradually disappears when the degree of blunting is directly related with the applied load and plastic deformation is taken into account. When LEFM is unable to define the conditions of stress and strains at the crack tip, then we consequently observe permanent plasticity.

In terms of practicality, the CTOD (δ_p) can be very difficult to measure but the value can be inferred by adopting a “hinged model” with a plastic rotational factor simulating an extended crack length at r_p and measuring the displacement at the crack mouth (V_p) as a function of load (P) as shown in Figure 4.6.

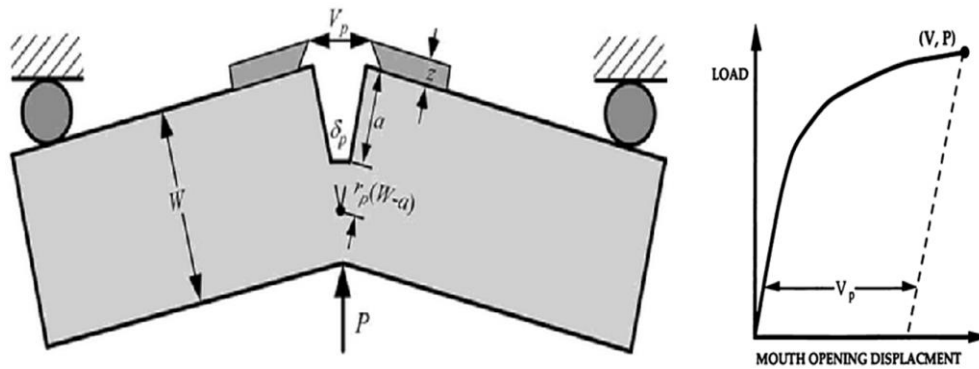


Figure 4.6 Hinged Model showing the simulated extended crack length at r_p accounting for small amounts of plasticity and the inferred crack mouth opening displacement as a function of load

To remain valid, the plastic zone r_p has to remain small 1/50 compared to the characteristic dimensions of a test specimen such as the crack length (a), the thickness (B) or the remaining ligament ($W - a$). The radius of r_p for plane strain conditions is defined by Equation 4-38.

$$r_p = \frac{1}{6\pi} \left(\frac{K_I}{\sigma_{Ys}} \right)^2 \quad 4-38$$

Where:

K_I = fracture toughness for mode I

σ_{Y_S} = yield strength of material

4.3.2.2 J-Controlled Fracture

For structural steels in the presence of large-scale plasticity, linear elastic fracture mechanics cannot accurately characterize the fracture behavior. Consequently, another detailed nonlinear fracture mechanics model needs to be implemented. The Figure 4.7 illustrates the contour integral, which is observed near the crack tip to describe the J-integral. A new fracture parameter called the J integral was proposed by Rice. This parameter uses the source of the deformation theory of plasticity. At present, Rice is serving in the Harvard University; when J integral was proposed, he was then affiliated with Brown University:

$$J = \int_{\Gamma} w \, dy - T_i \frac{\partial u_i}{\partial x} \, ds \quad 4-39$$

Where:

Γ = Arbitrary path around a crack tip

w = Strain energy density defined by: $w = \int_0^{\varepsilon_{ij}} \sigma_{ij} \, d\varepsilon_{ij}$

σ_{ij} = stress tensor

ε_{ij} = strain tensor

T_i = components of the traction vector. This would define the stresses acting on the boundaries of a free body diagram.

u_i = displacement vector components

ds = length increment along the contour Γ

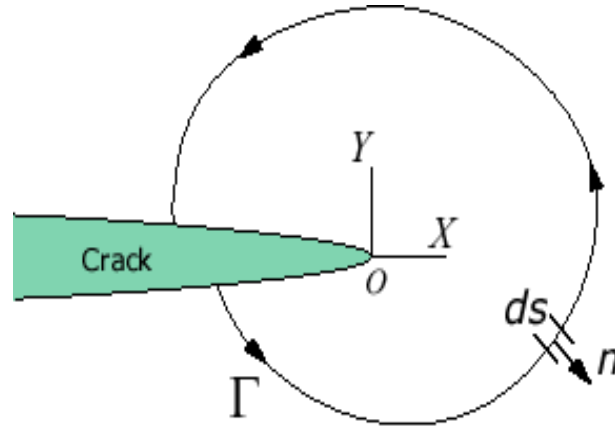


Figure 4.7 Contour integral around crack tip used to define the J-integral.

With the J-integral, Rice and Rosengren at Brown University and Hutchinson at Harvard University freely estimated the character of crack-tip stress fields for power-law hardening materials. The plane strain and plane stress conditions both were taken into account by Hutchinson. Whereas, only the plane strain conditions were analyzed by Rice and Rosengren. Findings of these studies reveal that the product of stress strain near the crack tip is inversely proportional to 'r'. Hutchinson's paper has mathematically proved this relationship. The power-law hardening materials were discovered by McClintock. Moreover, this information was used by Hutchinson to obtain an equation for asymptotic solutions of crack-tip stress strain fields:

$$\sigma_{ij} = \sigma_0 \left(\frac{J}{\alpha \sigma_0 \varepsilon_0 l_n r} \right)^{\frac{1}{n+1}} \sigma'_{ij}(n, \theta) \quad 4-40$$

$$\varepsilon_{ij} = \alpha \varepsilon_0 \left(\frac{J}{\alpha \sigma_0 \varepsilon_0 l_n r} \right)^{\frac{n}{n+1}} \varepsilon'_{ij}(n, \theta) \quad 4-41$$

Where:

σ_{ij} and ε_{ij} = stress and strain distributions

l_n = is an integration constant that depends on plane stress and plane strain conditions and on n .

σ'_{ij} and ε'_{ij} = dimensionless functions of n and θ

J = defines the amplitude of the HRR singularity similar to the K for LEFM.

$$\frac{\varepsilon}{\varepsilon_0} = \frac{\sigma}{\sigma_0} + \alpha \left(\frac{\sigma}{\sigma_0} \right)^n \quad 4-42$$

Where:

σ_0 = reference stress value that is usually the yield strength

$\varepsilon_0 = \sigma_0/E$

α = dimensionless constant

n = strain-hardening exponent

4.4 Fatigue crack growth

Fatigue crack propagation can be divided into three stages: stage **I** (short cracks), stage **II** (long cracks) and stage **III** (final fracture)

4.4.1 Initiation and stage I fatigue crack growth

The formation of surface cracks and their growth are better interpreted as specifying the number of cycles to an “engineering” size (3 mm deep) constitute the fatigue life of a material, which is represented by the fatigue σ - N curves. Fatigue life has conventionally been divided into two stages: initiation, expressed as the cycles required forming micro-cracks on the surface; and propagation, expressed as cycles required to propagate the surface cracks to engineering size. During cyclic loading of smooth test specimens, surface cracks of 10 μm or longer form quite early in life (i.e., <10% of life) at surface irregularities or discontinuities either already in existence or produced by slip bands, grain boundaries, second- phase particles, etc. consequently, fatigue life may be considered to be composed entirely of propagation of cracks from 10 to 3000 μm long.

The initiation stage involves growth of microstructurally small cracks (MSCs), characterized by decelerating crack growth (Region AB in Figure 4.8). The propagation stage involves growth of mechanically small cracks, characterized by accelerating crack growth (Region BC in Figure 4.8a). The growth of MSCs is very sensitive to microstructure. Fatigue cracks greater than the critical length of MSCs show little or no influence of microstructure, and are termed mechanically small cracks. Mechanically small cracks correspond to Stage II (tensile) cracks, which are characterized by striated crack growth, with a fracture surface normal to the maximum principal stress. Once a

microcrack forms on the surface, it continues to grow along its slip plane as a Mode II (shear) crack in Stage I growth (orientation of the crack is usually at 45° to the stress axis) as schematically represented in Figure 4.8. At low strain amplitudes, a Stage I crack may extend across several grain diameters before the increasing stress intensity of the crack promotes slip on systems other than the primary slip system. A dislocation cell structure normally forms at the crack tip. Because slip is no longer confined to planes at 45° to the stress axis, the crack begins to propagate as a Mode I (tensile) crack, normal to the stress axis in Stage II growth. At high strain amplitudes, the stress intensity is quite large, and the crack propagates entirely by the Stage II process. Stage II continues until the crack reaches engineering size (3 mm deep).

4.4.2 Stage II fatigue crack growth

When the stress intensity factor K increases as a consequence of crack growth or higher applied loads, slips start to develop in different planes close to the crack tip, initiating stage II. Whilst stage I is orientated 45 degrees in relation to the applied load, propagation in stage II is perpendicular to the load direction, as depicted in Figure 4.8.

An important characteristic of stage II is the presence of surface ripples known as “striations,” which are visible with the aid of a scanning electron microscope. Not all engineering materials exhibit striations; however, they are clearly seen in pure metals and many ductile alloys such as aluminum. In steels, they are frequently observed in cold-worked alloys. The most commonly accepted mechanism for the formation of “striations” on the fatigue fracture surface of ductile metals, is the successive blunting and re-sharpening of the crack tip, as represented in Figure 4.8 and Figure 4.9.

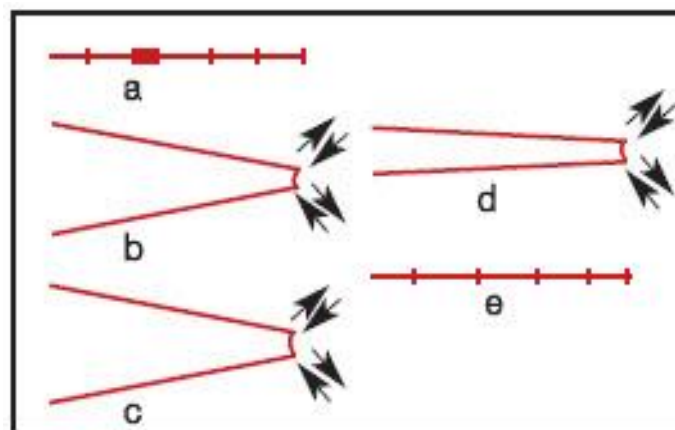


Figure 4.8 Stage I and II of fatigue crack propagation

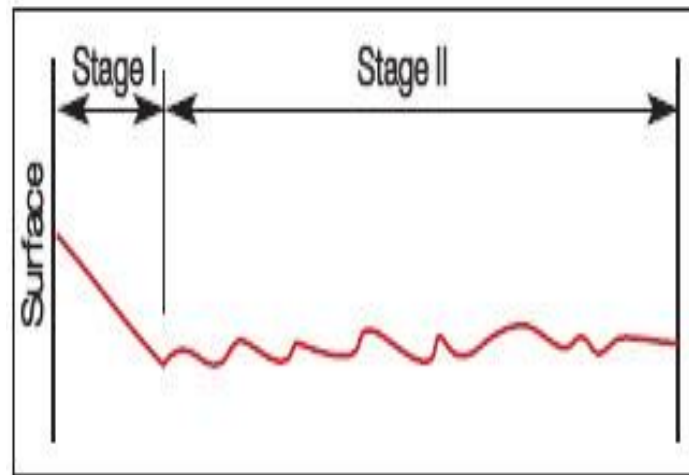


Figure 4.9 mechanisms of striation formation in the stage II of propagation: (a) no load (b) tensile load (c) maximum tensile load (d) load reversion and (e) compressive load

4.4.3 Stage III fatigue crack growth (final fracture)

Finally, stage **III** is related to unstable crack growth as K_{max} approaches K_{Ic} . At this stage, crack growth is controlled by static modes of failure and is very sensitive to the microstructure, load ratio, and stress state (plane stress or plane strain loading). Macroscopically, the fatigue fracture surface can be divided into two distinct regions, as shown by Figure 4.10.

The first region (the lower region depicted in each example in Figure 4.10) corresponds to the stable fatigue crack growth and presents a smooth appearance due to the friction between the crack wake faces. Sometimes, concentric marks known as “beach marks” can be seen on the fatigue fracture surface, because of successive arrests or a decrease in the rate of fatigue crack growth due to a temporary load drop, or due to an overload, that introduces a compressive residual stress field ahead of the crack tip.

Final fracture: The other region (the upper region depicted in each example in Figure 4.10) corresponds to the final fracture and presents a fibrous and irregular appearance. In this region, the fracture can be either brittle or ductile, depending on the mechanical properties of the material, dimensions of the material under stress, and loading conditions. The exact area of fraction of each region depends on the applied load level. High applied loads result in a small stable crack propagation area, as depicted in Figure 4.10a. On the other hand, if lower loads are applied, the crack will have to grow

for longer before the applied stress intensity factor K , reaches the fracture toughness value of the material, resulting in a smaller area of fast fracture Figure 4.10b.

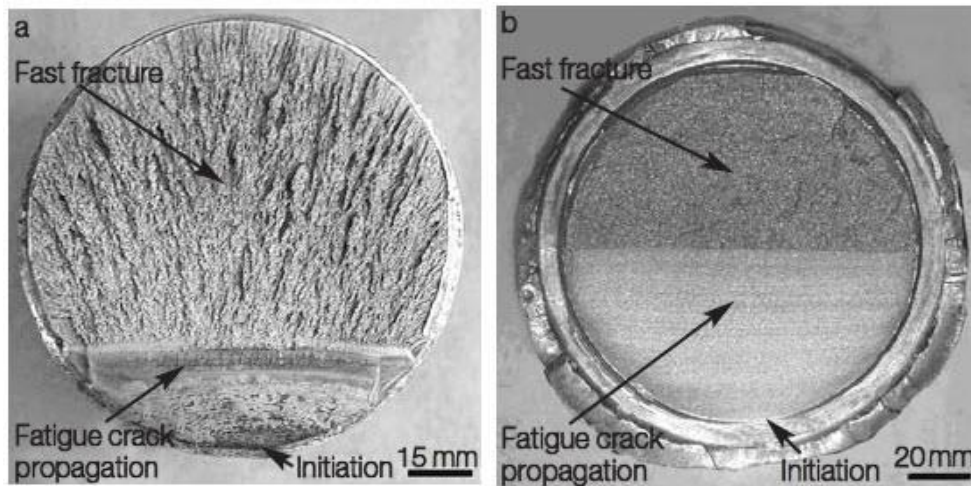


Figure 4.10 Fatigue fracture surface: (a) high applied load; (b) low applied load

4.5 Fatigue Life Prediction

It is important to gain an insight with the behavior of fatigue crack growth and the allied mechanisms to develop techniques for predicting fatigue lifetime. To handle and address this particular issue, ‘Damage-Tolerance’ and ‘Total Life’ are the two basic methodologies, which are generally used in fatigue design.

The total life approach involves characterization of total fatigue life of specimens in inert and aqueous environments. The Stress-Life (S-N) or Strain-Life (E-N) curves depict the relationship between the stress or strain range and the fatigue life, which can be applied for design purposes so that the design or residual lives of engineering modules could be calculated. Concerning the quantitative assessment of fatigue damage, it is quite easy to apply the S-N method. Nonetheless, the experimental data is an obstacle, which can exhibit considerable and scattered distribution because of various factors including flaw distribution and surface finish etc., which can have significant impact on the crack nucleation stage. Moreover, identifying the damage mechanisms, through which these two stages of the fatigue life is administered, is always a challenging task because the propagation life and the crack initiation life are not detached. Therefore, it is usually a traditional methodology to fatigue design and analysis.

4.5.1 High cycle fatigue

At low stress levels, total deformation in the material is elastic so the material can undergo high number of cycles. Hence, fatigue resistance is usually characterized in terms of the stress range. The S-N curve can be described empirically using the Basquin relationship expressed below

$$\Delta\sigma/2 = \sigma_f'(2N_f)^b \quad 4-43$$

where $\Delta\sigma$ represents the stress range, σ_f' , the fatigue strength coefficient, b , the fatigue strength exponent and N_f is the number of cycles to failure.

4.5.2 Low cycle fatigue

In contrast to high cycle fatigue, low cycle fatigue involves stress levels that are high enough to cause plastic deformation; hence, the material can only sustain low number of cycles. Because deformation is no more elastic, the strain range is used to characterize the fatigue behavior of the material. The Coffin-Manson relationship provides method for describing the fatigue behavior of materials.

$$\Delta\varepsilon_p/2 = \varepsilon_f'(2N_f)^c \quad 4-44$$

where $\Delta\varepsilon_p$ represents the plastic strain range ε_f' , the fatigue ductility coefficient, c , the fatigue ductility exponent and N_f is the number of cycles to failure.

Since the total strain can be decomposed into the elastic and plastic components (Equation 4-45), both Equations 4-43 and 4-44 can be summed as expressed below:

$$\frac{\Delta\varepsilon}{2} = \frac{\Delta\varepsilon_e}{2} + \frac{\Delta\varepsilon_p}{2} \quad 4-45$$

$$\frac{\Delta\varepsilon}{2} = \frac{\sigma_f'}{E} (2N_f)^b + \varepsilon_f' (2N_f)^c \quad 4-46$$

where $\Delta\varepsilon$ is the total strain range and E is the Young's modulus.

4.6 Fatigue Assessment of Welded structures

Due to fatigue, impairment in all engineering materials such as welded aluminum structures starts from the micro-level. Afterwards, this damage becomes clear and evident because formation of micro-cracks is observed on the slip bands because of plastic deformation. Coalescence and propagation of mini-cracks is indicative of [42, 43]. In aircraft structures, the general causes of mechanical failure are none other than the fatigue failures [42]. Since some shortcoming is left in welds, the welds usually reveal the fatigue failures in these structures and not generally in the base material, even when clear notches and re-entrant corners are seen in the latter. Therefore, it is essential to carry out a reliable and good fatigue assessment in all structures where we anticipate the cyclic loads, because the safety, particularly in aero-structures cannot be ensured without fatigue assessment [43, 44]. A number of factors, such as, synthesis, analysis and testing with or without computer-aided design, are included in the proper fatigue design [49].

In fatigue assessment, the stresses and environmental influences are compared, which are required by the airframe structures to maintain their possible resistance. Therefore, to endure these stresses without failing, resistance must be possessed by the welded structures. In the design of welded structures, the given below techniques evaluate the fatigue lives [50]:

S-N curves for specific welded joints are used alongside nominal stresses,

S-N curves for welds are used together local notch stresses, and

S-N curves for welds are used with hotspot stresses.

The S-N curve generally represents the fatigue resistance data, which is a design scheme containing nominal applied cyclic stress range, 'S', and the corresponding number of cycles, 'N', to failure. The maximum amount of load fluctuations ensured by a structure prior to failure in design life is indicated by these statistics. The linear regression analysis of log S versus log N results in the S-N curves.

For the material (welded joint), the stress levels corresponding to the static design limit to a fatigue endurance limit are entailed in the curves. The differences in stress amplitudes are not considered, which is believed to be one of the disadvantages.

Palmgren-Miner's rule is usually applied where it is assumed that the fatigue damage due to n_i cycles is directly proportional to n_i/N_i . From the FEA (finite element analysis) or strain gauge measurement, the loading history is found to calculate the stress history experienced by the structure (airframe). Afterwards, the recognizable stress cycles are extracted from stress spectrum.

The integrity of FSWs is evaluated by the fatigue assessment method, which is standardized and well established, [51]. Here, S-N curves are obtained from fatigue tests, which are performed on specimens having the relevant weld detail (FSW). By considering the scatter of fatigue behavior, we obtain the fatigue design curves, and a reference curve is provided with a probability of survival at least equal to 97.7 % [52]. We usually consider the design curve as the mean having two standard deviation extensions on either side of log N.

In codes and standards, the curves are identified by the fatigue strength at $2 * 10^6$. The slope of m at the S-N curve as in the draft Euro-code [53], which are most consistent experimental data, or by arbitrary letters such as Class A, B, and C by the Aluminum Association [51].

However, for FSW, no general overview is available to assist structural designers in determining design strength values or their dependence on welding parameters and material specification [55].

4.6.1 Fatigue Behavior of FSW Aluminum Joints

Improvement in fatigue strength of FSW over other processes: according to Lomolino et al. [55], the lack of filler materials supports this supremacy, which can be answerable for the misalignment features and likely notch effects. The base material values are approached by the fatigue values obtained from various tests [55]. The pronounced tool marks or lips, surface roughness, typical defects, for instance, lack of penetration (LOP) and flash on surface of the joint generally result in the fatigue failures in FSW.

The characteristics influencing the fatigue strength of FSW aluminum joint are given as: Parent material condition; Stress ratio 'R'; Surface condition; Temper condition; Residual stresses and Presence of defects.

The speed is intercepted and crossed due to the increase in FSW. Moreover, slight increases in high cycle fatigue is linked with the decrease in welding speed, because the low heat inputs are associated with them, which leads to the high-speed cooling rates of the welded joints [44, 45]. The micro-structural changes are restrained as a result, thus local strength is affected across the weld. As compared to the artificially aged FSW joints, superior fatigue performance is exhibited by the naturally aged ones for the same alloy composition. One of the factors influencing fatigue performance was the stress ratio, for example, in AA6082 (tested with $R = 0.5$ and $R = -1$) [45]. The tests performed with a negative stress ratio yielded in the improvements in fatigue strength at $2 * 10^{-6}$, cycles, because stress applied are compressive to some extent [53]. As per Kahl et al. [59], surface conditions have great importance; the time of crack initiation was determined by the height of burrs and the transition from large grains in the statically recrystallized layer on the profile surface to small grains of dynamically recrystallized nugget. Therefore, lower fatigue strength associated with as-weld surfaces corresponding to polished specimens needs clarification. The experts advise mechanical machining of the weld surface to improve fatigue properties, as the fatigue strength is reduced by the surface roughness because a stress concentration linked with the weld flash or the spiral features created by the tool are generally related to the crack initiation. For practical objectives, advantages are still presented by a slightly rough surface or small undercut over traditional welding methods. A key role is also played by the occurrence of defects. It has been revealed that AA6082-T6 specimens, with weak bands of oxides than those with strong bands of oxides, excluding for tests carried out at the highest test amplitudes [54], possessed higher fatigue resistance. According to the mathematical explanation of Zhou et al. [54], kissing bonds (joint line remnants made of oxides) produced a decrease in the fatigue attributes of Al2024 and Al 5083 at $2 * 10^{-6}$, cycles from 100.3 MPa to 65.6. In addition, the root flaws caused a decline from 120.6 MPa to 54.7 MPa.

5 Extended Finite Element Method (XFEM)–Numerical simulation

5.1 Introduction

In the field of mechanics, the study that deals with the propagation of cracks in materials is known as Fracture Mechanics. With the purpose of forecasting the macroscopic automated disasters of figures accurately, the concepts of plasticity and elasticity and physics of stress strain is practically used for the microscopic crystallographic shortcomings present in actual supplies.

When learning fracture mechanics, Finite Element Method (FEM) takes a significant place since in the arrangement of structural elements of challenging geometric form this technique has specified its substantial involvement.

The only method to hold non-smooth fracture tip grounds with regard to stress strain is through a locally developed network while for fracture mechanics the finite element method has proved to be generally compatible. Thus, it has subsequently resulted in the rise of simulation run time and digit of degrees of elements. To demonstrate progressing incoherence, the network has to be redeveloped at each time stage and this is the reason why FEM discretization needs to imitate the incoherence. The damage value of outcomes and computational expenses are vividly increased due to the clarification needed on the reorganized network and is requisite to be proposed for every time phase. Numerous numerical methodologies have been suggested because of the boundaries to examine fracture mechanics complications [62]. Hence, the fracture propagation analysis in industrial exhibiting application is so far a problematic task. In order to examine fracture difficulties, the extended finite element method (XFEM) has developed to be an influential numerical process recently. We can perceive a great recognition for linear elastic fracture mechanics (LEFM), a method that has simplified fracture growth modeling. After 1999, several fresh additions and presentations can be observed specially after the foundation of this process in the scientific works [62]. The fracture is supposed to trail element edges in order to model a fracture according to the old-style construction of the FEM. The X-FEM delivers numerous advances in the numerical modeling fracture circulation as paralleled to finite element method. Figure 5.1 explained the contrast of 2D solid fracture examination model by enriched S-FEM (left) and extended S-FEM (right)

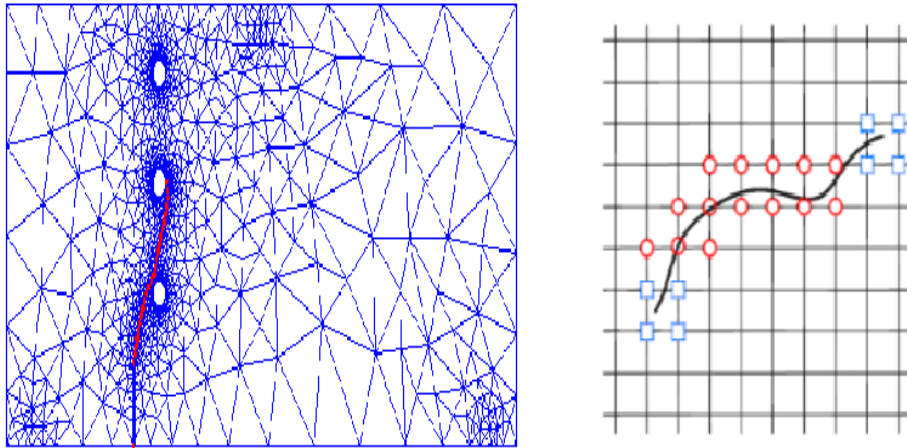


Figure 5.1 Comparison of 2D solid fracture analysis model using enriched S-FEM (left) and extended S-FEM (right)

Through addition of extra units of freedom in the nodes of elements cut by the fracture, the updated version of FE model known as the XFEM is structured. The network is produced entirely autonomous of the fracture, this way there is no requirement to change the area discretization of the fracture that is incorporated in the numerical model. However, for every fracture interval and positioning merely a single network is required. The function that generates the asymptotic fracture tip action can be found in great volume in the fracture tip, which the node surrounds. This sources correctness in the calculation of pressure concentration and features are increased, allowing the model of the fracture within the fracture-tip element.

5.2 Basics of extended finite element method

Modelling of cracks in the structure, using classical finite elements, requires matching the geometry discontinuities of finite element mesh. The problem is compounded in the case of modeling crack growth, which requires successive generation mesh in order to monitor ongoing changes in structure (geometric discontinuity in space).

XFEM allows the modeling of arbitrary shape cracks. In simulation quasistatic and fatigue crack growth, it is not necessary to change the mesh around the same crack during its progression [60].

XFEM is based on:

- Generating finite element mesh, while the discontinuity (Cracks) is not included, use of additional functions for the approximation of discontinuity, ie. Displacement. Additional features include a set of function enhancements. with analysis of crack growth, two types of feature enhancements are used:
 - discontinuous Heaviside's function- $H(x)$, which defines the field moving to the sides of the crack,
 - A set of linear elastic asymptotic scroll function, which describes the displacement field around the crack tip-called. Near Tip (NT) FUNCTIONS.

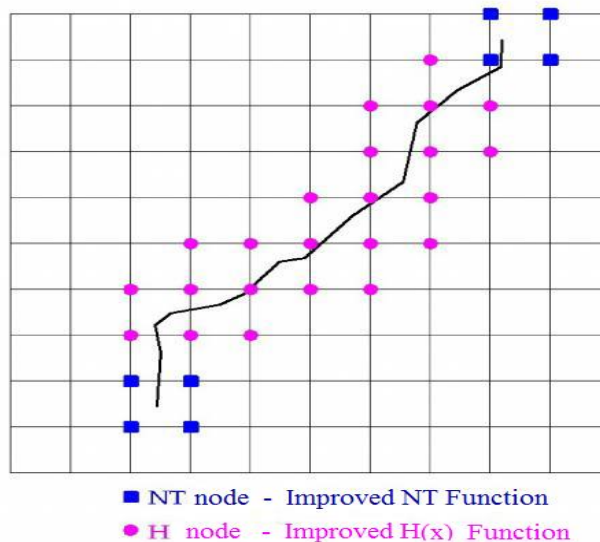


Figure 5.2 Nodes NT and $H(x)$ improved function

There are two node types:

1. H Node - Node improved Heaviside's springboard function - $H(x)$ is applied to the node only if at least one associated element transversal crack (Figure 5.2), and that neither one of them is not in top crack. This type of node has 4 degrees of freedom.
2. NT node - the node that has been enhanced with four functions asymptotic field displacements around the crack tip. NT nodes are nodes in the element that have 10 degrees of freedom.

5.2.1 Defining of the displacement field $XFEM - u$

Elements that contain at least one enriched node are known as enriched elements. Nodes with two additional DOFs (one for each coordinate direction) have shape functions that multiply the Heaviside function $H(x)$ (function of unit magnitude whose sign changes

across the crack, $H(x) = \pm 1$). Physically, this function introduces the discontinuity across the crack faces. Nodes with eight additional DOFs are enriched in the two Cartesian directions with four crack tip functions $F_\alpha(x)$ [61]:

$$\begin{aligned}
 & [F_\alpha(r, \theta), \alpha = 1 - 4] \\
 & = \left[\sqrt{r} \sin \frac{\theta}{2}, \sqrt{r} \cos \frac{\theta}{2}, \sqrt{r} \sin \frac{\theta}{2} \sin \theta, \sqrt{r} \cos \frac{\theta}{2} \sin \theta \right] \dots \quad 5-1
 \end{aligned}$$

where (r, θ) are local polar coordinates defined at the crack tip. We note that the span of the above functions can reproduce the asymptotic mode I and mode II displacement fields in LEFM, which gives rise to the near-tip singular behavior in strains and stresses [61].

The displacement approximation for crack modelling in the extended finite element method takes the form [60]:

$$\begin{aligned}
 u_{x_{FEM}}(x) = & \sum_{i \in I} N_i(x) u_i + \sum_{i \in J} N_i(x) H(x) a_j \\
 & + \sum_{i \in K} \left[N_i(x) \sum_{\alpha=1}^4 F_\alpha(x) b_k^\alpha \right] \dots \quad 5-2
 \end{aligned}$$

where I is the set of all nodes in the mesh, $N_i(x)$ is the nodal shape function and u_i is the standard DOF of node i (u_i represents the physical nodal displacement for non-enriched nodes only). The subsets J and K contain the nodes enriched with Heaviside function $H(x)$ or crack-tip functions $F_\alpha(x)$, respectively, and $a_i, b_{i\alpha}$ are the corresponding DOFs. If there is no enrichment, then the above equation reduces to the classical finite element approximation $u_{FE}(x) = \sum_i N_i(x) u_i$.

Hence, X-FEM retains many of the advantages of the It is important to note that the additional DOFs a_j, b_k^α in 5-2 are only added to the nodes that are enriched. Moreover, in this implementation no nodes are enriched with DOFs a_j, b_k^α simultaneously (they are mutually exclusive) and hence the Heaviside functions that introduce the crack discontinuity are not used at the nodes of the crack-tip element. The crack discontinuity

C – Constitutive matrix of isotropic linear elastic material

B_u – Classical shape functions matrix

B_a – Improved shape functions matrix

Matrix B_u and B_a are summarized in general terms:

$$B_u = \begin{bmatrix} N_{i,x} & 0 & 0 \\ 0 & N_{i,y} & 0 \\ 0 & 0 & N_{i,z} \\ 0 & N_{i,z} & N_{i,y} \\ N_{i,z} & 0 & N_{i,x} \\ N_{i,y} & N_{i,x} & 0 \end{bmatrix} \dots \dots \dots \quad 5-6$$

$$B_a = \begin{bmatrix} (N_i \Psi_i^\alpha)_{,x} & 0 & 0 \\ 0 & (N_i \Psi_i^\alpha)_{,y} & 0 \\ 0 & 0 & (N_i \Psi_i^\alpha)_{,z} \\ 0 & (N_i \Psi_i^\alpha)_{,z} & (N_i \Psi_i^\alpha)_{,y} \\ (N_i \Psi_i^\alpha)_{,z} & 0 & N_{i,x} \\ (N_i \Psi_i^\alpha)_{,y} & (N_i \Psi_i^\alpha)_{,x} & 0 \end{bmatrix} \dots \dots \dots \quad 5-7$$

Where:

$$N_{i,k} = \frac{\partial(N_i(x))}{\partial x_k}$$

$$(N_i \Psi_i^\alpha)_{,k} = \frac{\partial(N_i(x)\Psi_i^\alpha)}{\partial x_k}$$

$(N_i \Psi_i^\alpha)_{,k}$ – Can be calculated using:

$$\frac{\partial(N_i(x)\Psi_i^\alpha)}{\partial x_k} = \frac{\partial(N_i(x))}{\partial x_k} \Psi_i^\alpha(x) + N_i(x) \frac{\partial(\Psi_i^\alpha(x))}{\partial x_k} \dots \dots \dots \quad 5-8$$

q and f Matrixes can be expressed as follows:

$$q^T = \{u \quad a\}^T \quad \dots \dots \dots \dots \dots \dots \quad 5-9$$

$$f^T = \{f_u^T \quad f_a^T\} \quad \dots \dots \dots \dots \dots \dots \quad 5-10$$

Where:

u and a – Classical displacement and additional degrees of freedom vectors

f_u and f_a – Classical applied force and improved approximation of displacement components vectors

It is possible to calculate the relative strain and stress vectors, using the enhancement features and additional degrees of freedom

$$\varepsilon = [B_u \quad B_a] \{u \quad a\}^T \quad \dots \dots \dots \dots \dots \dots \quad 5-11$$

$$\sigma = C . \varepsilon \quad \dots \dots \dots \dots \dots \dots \dots \dots \dots \quad 5-12$$

5.3 XFEM Implementation in Abaqus

The XFEM is included in the multi-purpose commercial FEM software as there are some massive developments delivered by the XFEM. The lack of commercial software evidence of the practice of a method like XFEM is because of the fact that it was generated and expended in 1999. Softwares like Morfeo and ASTER are softwares that have the ability but Abaqus, LS-DYNA and ANSYS are the most prominent amongst commercial softwares and with the Abaqus 6.9 announcement [67] the XFEM segment was primarily announced in Abaqus in 2009. The phantom nodes method [64] are the foundation of the XFEM application in Abaqus/Standard in which to replicate the existence of the incoherence it requires the phantom nodes to be superposed by the actual ones. Established on the Level Set Method the fracture tip location and the fracture exteriors in Abaqus are recognized with a statistical technique. Every node of the finite element grid is branded along with the three coordinates concerning the global coordinate system and further two constraints, called PHILSM and PSILSM when once the network

discretization has been shaped. These constraints have the ability to be effortlessly taken as the nodal coordinates in a coordinate structure of the developed nodes focused at the fracture tip and respectively having axes of tangent and normal, to the fracture surfaces at the fracture tip and only for the enriched elements, these parameters are nonzero [67].

5.3.1 Modeling Approach

The insufficiencies that were linked with enmeshing fracture exteriors have been explained by the extended finite element method (XFEM) additional to degrees of freedom and special enriched functions simulated the presence of incoherence. The upgrading purposes usually comprise of the uniqueness around the fracture tip, which signifies near-tip asymptotic functions, and the jump in dislocation across the fracture surfaces is replicated by Heaviside function for the purpose of fracture analysis. A constant fracture tracing is mandatory for modeling the fracture-tip individuality. Modeling stationary cracks in Abaqus/Standard is the lone condition when the asymptotic singularity functions are deliberated [67] as the position of the fracture is in control for the amount of individuality of the fracture which makes the procedure challenging. To learn moving fractures there are two types of methodologies that are considered. The first one practices the concept of Fracture Mechanics where a blend of mechanisms of the energy release rate is equivalent to, or above, an acute rate that forecasts fracture growth. Calculation of ERR have been carried out through methods such as virtual crack extension, J-integral method and virtual crack closure technique (VCCT). However the expansion of the second one practices cohesive zone theory and is built on Damage Mechanics in which the interface containing the fracture is modeled by a damageable material and when a damage criterion touches its extreme value [65] the fracture is commenced. To model moving fracture in Abaqus, arrangement with phantom node technique, cohesive segment method and VCCT technique are used.

5.3.2 Virtual Crack Closure Technique

Both, separation of anisotropic layers and Fracture propagation phenomena can have resemblances. Thus, to govern the circumstances for the fracture launch and progress and to learn the behavior of fracture we can practice fracture mechanics principles [63]. The energy that is unconfined for unit width and length of fracture exterior (called Strain Energy Release Rate, G) and fracture sturdiness or acute level that is a material property

[63] must be equivalent for the fracture diffusion to be conceivable. The theory saying that for a diminutive fracture opening, the amount of effort needed to seal the fracture is equivalent to the extent of pressure energy unconstrained is the foundation of Virtual Crack Closure Technique. For a fracture that is of length a , the work W compulsory to seal the fracture can be assessed by estimating the pressure ground at the fracture tip, further attaining dislocations as illustrated in Figure 5.3 when the fracture visible prolonged from a to $a+\Delta a$.

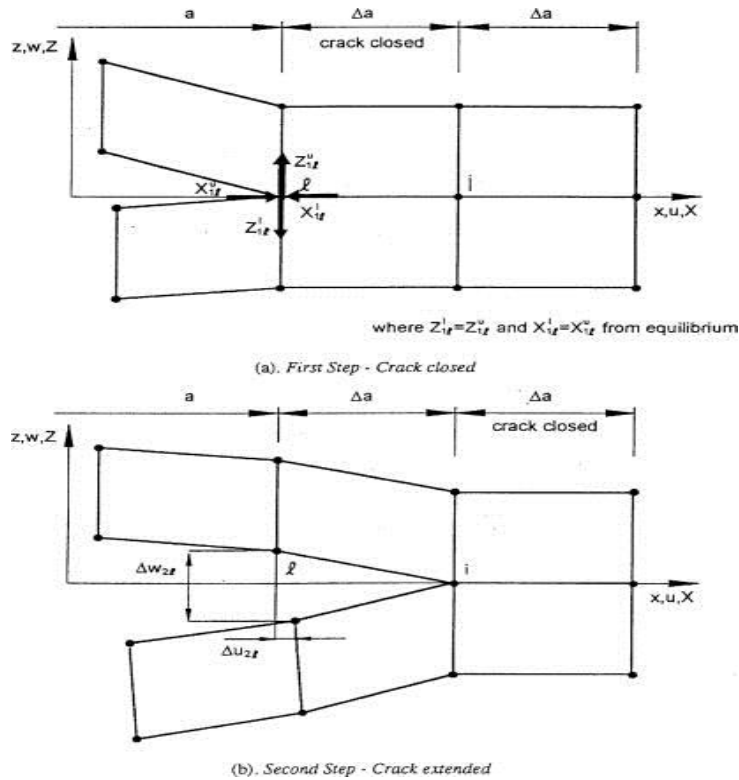


Figure 5.3 Crack closure method ~two-step method, a) First step—crack closed and b) Second step—crack extended.

Virtual Crack Closure Technique is based on the assumption that for a very small fracture opening. Additionally, however, it is assumed that a crack extension of Δa from $a + \Delta a$ (node i) to $a + 2\Delta a$ node (k) does not significantly alter the state at the crack tip Fig.3. Therefore, when the crack tip is located at node k , the displacements behind the crack tip at node i are approximately equal to the displacements behind the crack tip at node l , when the crack tip is located at node i . Further, the energy ΔE released when the crack is extended by Δa from $a + \Delta a$ to $a + 2\Delta a$ is identical to the energy required to close the crack between locations i and k . for a crack modeled with two-dimensional, four-

nodded elements, the work ΔE required to close the crack along one element side therefore can be calculated as

$$\Delta E = \frac{1}{2} [X_i \Delta u_l + Z_i \Delta w_l] \quad \dots \dots \dots \dots \dots \dots \quad 5-13$$

where X_i and Z_i are the shear and opening forces at nodal point i and Δu_l , and Δw_l , are the shear and opening displacements at node l

The expression of the work W based on this two-step Virtual Crack Closure Technique is given by

$$W = \frac{1}{2} \left(\int_0^{\Delta a} \sigma_{yy}^{(a)}(x) \delta u_y^{(b)}(x) dx + \int_0^{\Delta a} \sigma_{yx}^{(a)}(x) \delta u_x^{(b)}(x) dx + \int_0^{\Delta a} \sigma_{yz}^{(a)}(x) \delta u_z^{(b)}(x) dx \right) \quad 5-14$$

Another approach, which is the one-step Virtual Crack Closure Technique. It is based on the assumption that a very small fracture extension has negligible effects on the fracture front. In this case, stress and displacement can be calculated in the same step by performing one analysis. Using this technique, the expression of the work W needed to close the fracture becomes:

$$W = \frac{1}{2} \left(\int_0^{\Delta a} \sigma_{yy}^{(a)}(x) \delta u_y^{(b)}(x - \Delta a) dx + \int_0^{\Delta a} \sigma_{yx}^{(a)}(x) \delta u_x^{(b)}(x - \Delta a) dx + \int_0^{\Delta a} \sigma_{yz}^{(a)}(x) \delta u_z^{(b)}(x - \Delta a) dx \right) \quad 5-15$$

where both displacements and stress are evaluated in the step (a) of Figure 5.3. Based on the definitions given, the Energy Release Rate can be written as

$$G = \lim_{\Delta a \rightarrow 0} \frac{W}{\Delta a} \quad 5-16$$

5.4 Fracture Growth Criteria

In fracture mechanics, the Strain Energy Release Rate (G) is compared with the material fracture toughness (G_C), as the criterion for the fracture initiation and propagation. When G is larger than G_C , fracture initiates ($G > G_C$). Experimental tests are usually used to measure G_C . However, for an accurate and comprehensive test, several different types of

samples are needed to generate fracture toughness data over a desired range of mixed-mode combinations [70]. Therefore, several empirical criteria have been offered to calculate fracture toughness for mixed mode. One of the most used criteria is the power law that may be used to represent a wide range of material responses by selecting the two exponents, α and β . Power law criterion is expressed as

$$\left(\frac{G_I}{G_{IC}}\right)^\alpha + \left(\frac{G_{II}}{G_{IIC}}\right)^{\alpha\beta} + \left(\frac{G_{III}}{G_{IIIC}}\right)^\gamma = 1 \quad 5-17$$

Another one is the B-K criterion [9], which requires the selection of only one fitting parameter η . The B-K criterion is

$$\frac{G_T}{G_{IC} + \left[(G_{IIC} - G_{IC}) \frac{G_{II}}{G_T} + (G_{IIIC} - G_{IC}) \frac{G_{III}}{G_T} \left(\frac{G_{II} + G_{III}}{G_T} \right)^{\eta-1} \right]} = 1 \quad 5-18$$

These criteria are empirical mathematical expressions to represent different material responses by varying the values assigned to the fitting parameters. Thus, the selection of these parameters requires that mixed-mode testing be performed during the characterization of the material [69].

5.4.1 Evaluation of the stress intensity factors

The disaster forecast of material because of the existence of cracks is calculated and nearby, the crack tip thorough stress distribution is categorized, in fracture mechanics this constraint is known as Stress intensity factor (SIF). To manage the uniqueness at dissimilar stages of intricacy of the stress field nearby the crack tip following approaches can be supportive. A number of numerical approaches for instance the element free Galerkin method (EFG) [66–68], the boundary element method (BEM) [63–65] and the finite element method (FEM) [60–62], have been used in complex geometric structures to assess the singular field close to the crack-tip by the researchers to study the crack behavior. It seems like in stress analysis around a crack there is a massive extent of consideration towards extended finite element method (XFEM) lately compatible to the crack minus exhausting a network. The constraint for incoherence to follow to element restrictions is abolished in XFEM and it permits autonomous modeling of discontinuities

for network, nothing like the crack modeling in FEM. In consequence, without openly interconnecting the incoherence, supporting the domain to be discretized and permitting a disjointedness to be subjectively positioned in an element. Griffith energy method [66], the virtual crack extension technique and the path-independent J-integral [64], etc. are the most prominently applied methods. With the purpose of calculating stress intensity factors for numerous fracture problems, many investigators have established and practically used a number of methods that are constructed centering the numerical systems. The conclusion of the boundary value problem is used in the interaction integral in which auxiliary fields are placed over onto the authentic fields. Conversion of the energy integral of contour collaboration from the general 2D crack tip contour integral can be observed once the auxiliary fields are selected in the correct arrangement.

$$I = \int_{\Gamma} (\sigma_{ik} \varepsilon_{ik}^{aux} \delta_{1j} - \sigma_{ij} u_{i,1}^{aux} - \sigma_{ij}^{aux} u_{i,1}) n_j d\Gamma \quad 5-19$$

Where $u_{i,1}^{aux}$, ε_{ik}^{aux} and σ_{ij}^{aux} are the auxiliary displacements, strain, and stress fields respectively. The domain form of this interaction integral changes the evaluation of a line integral into the calculation of an integral over an area - a technique ideally suited to a finite element framework.

$$I = \int_A (\sigma_{ik} \varepsilon_{ik}^{aux} \delta_{1j} - \sigma_{ij} u_{i,1}^{aux} - \sigma_{ij}^{aux} u_{i,1}) q_j dA \quad 5-20$$

where q is a smooth scalar weighting function that is unity at the crack tip and becomes zero at the edge of the domain area.

5.4.2 Difficulties in the XFEM

As the method permits arbitrary functions to be incorporated in the FEM approximation basis, the partition of unity (PU) enrichment leads to greater flexibility in modelling moving boundary problems, without changing the underlying mesh, while the set of enrichment functions evolve (and/or their supports) with the interface geometry. Although XFEM is robust and applied to a wide variety of moving boundary problems and interface problems, the flexibility provided by this class of methods also leads to associated difficulties:

-
- Singular and discontinuous integrands

When the approximation is discontinuous or non-polynomial in an element, special care must be taken to numerical integrate over enriched elements.

- Blending the different partitions of unity

The local enrichment used in the conventional element leads to oscillations in the results over the elements that are partially enriched.

- Poor convergence rate

In the conventional XFEM, the obtained convergence error of XFEM remains only in \sqrt{h} , when linear finite elements are used, where h is the element size.

- Stress intensity factor computation

XFEM requires a post-processing stage to extract the stress intensity factors (SIFs) from the computed displacement field. Although not a major difficulty, but this particular point has been addressed by some researchers.

- ILL-conditioning

The addition of enrichment functions to the FE approximation basis could result in a severely ill conditioned stiffness matrix.

- Additional unknowns

With extrinsic enrichment, additional degrees of freedom (DOFs) are introduced and the number of additional DOFs depends on the number of enrichment functions and the number of such enrichments required.

5.5 Morfeo/crack for Abaqus

5.5.1 Extended description of Morfeo/crack for Abaqus

Ever since version 6.10, the application of XFEM method existing in Abaqus is the technique, on which Morfeo/Crack for Abaqus depends on. In difficult geometries, Morfeo/Crack for Abaqus has the ability to accomplish crack propagation models and furthermore improves Abaqus, while calculation of stationary cracks is the maximum edge when it comes to the purpose of Abacusd. Every stage of transmission step in the system is requisite to call upon Abaqus/Standard. Amongst every step, Abaqus solution

is recited, a richer is recovered, in a minor extent adjacent to the crack by using, a tailored integration rule improves XFEM solution, regulation of crack advancement is prepared through calculating stress concentration factors precisely and with the different crack location, it apprises the Abaqus input file. Furthermore, CAE/Abaqus, the interface for user supports the Morfeo/Crack for Abaqus. The primary crack position combined with the fatigue crack propagation is used as a plug-in for the setup. Lastly, the freely available post processor (gms) and the post-processing of results in Abaqus/CAE are some of the choices offered by Morfeo/Crack for Abaqus. The advantages of Morfeo/Crack include easy realization of crack propagation movies and accurate solution at the crack tip.

5.5.1.1 Features

- Problem definition and initial crack positioning in Abaqus/CAE
- Automatic Abaqus/Standard execution at each propagation step with an input file updated with the current crack position
- Recovered extended finite element solution in a small area surrounding the crack, called the crack area hereafter
- Improved solution visualization in gms with respect to the visualization in Abaqus/CAE
- J-integral computation with the equivalent domain integral method
- Stress intensity factors extraction with the interaction integral method
- Crack representation with the level-set method
- Crack update with the fast marching method

5.6 Stress intensity factor calculation using 3D finite element models

5.6.1 Introduction

The aerospace industries show an increased interest in friction stir welding as a new joining technology for fuselage structures. The complex geometry of some kinds of joints and their three dimensional nature make it difficult to develop an overall system of governing equations for theoretical analyzing the behavior of the friction stir welded joints. The experiments are often time consuming and costly. To overcome these problems, numerical analysis has frequently been used since the 2000s. Numerical analysis of friction stir welding will allow many different welding processes to be simulated in order to understand the effects of changes in different system parameters

before physical testing, which would be time-consuming or prohibitively expensive in practice [71]. The main methods used in numerical analysis of friction stir welding are discussed and illustrated with brief case studies. In addition, Due to the extreme condition encountered during Friction stir Welded joints and the highly fatigue life of Friction stir Welded joints common problems, finite element methods have been widely developed to study fatigue crack growth behavior of friction stir welded T-joint.

FEA is a computational tool for performing engineering analysis. It includes the use of mesh generation techniques for dividing a complex problem into small elements, as well as the use of software program coded with FEM algorithm. In applying FEA, the complex problem is usually a physical system with the underlying physics, while the divided small elements of the complex problem represent different areas in the physical system. In this study, FEA is carried out by using the Extended FEA analysis. A 3D solid 84 brick element with eight nodes is used to mesh the geometry of the specimen. The meshing type of Element is second order Hexahedron.

All numerical modelling plates consist of one material region of aluminum alloy AA2024- T351, with different mechanical properties as shown in Table 5.1 and Figure 5.4.

Table 5.1 Material properties used in ABAQUS analysis

Elasticity				
FSW zones	NZ	TMAZ	HAZ	BM
Young's modulus of elasticity – E [GPa]	68	68	68	68
Poisson's ration - ν	0.33	0.33	0.33	0.33
Yield strength – σ_Y [MPa]	320	302	398	370

Plasticity								
	NZ		HAZ		TMAZ		BM	
σ [MPa]	ϵ	[-]	ϵ	[-]	ϵ	[-]	ϵ	[-]
20.4	0.0003		0.0003		0.0003		0.0003	
41.3	0.0006		0.0006		0.0006		0.0006	
59.6	0.0008		0.0008		0.0008		0.0009	
79	0.001		0.001		0.001		0.0011	
100.4	0.0014		0.0014		0.0015		0.0015	
136.9	0.0019		0.002		0.0021		0.0022	
186.6	0.0023		0.0025		0.0028		0.0028	
231.9	0.0035		0.0038		0.0048		0.0046	
323.4	0.0056		0.0086		0.0158		0.0104	
415.7	0.0198		0.0228		0.0398		0.032	

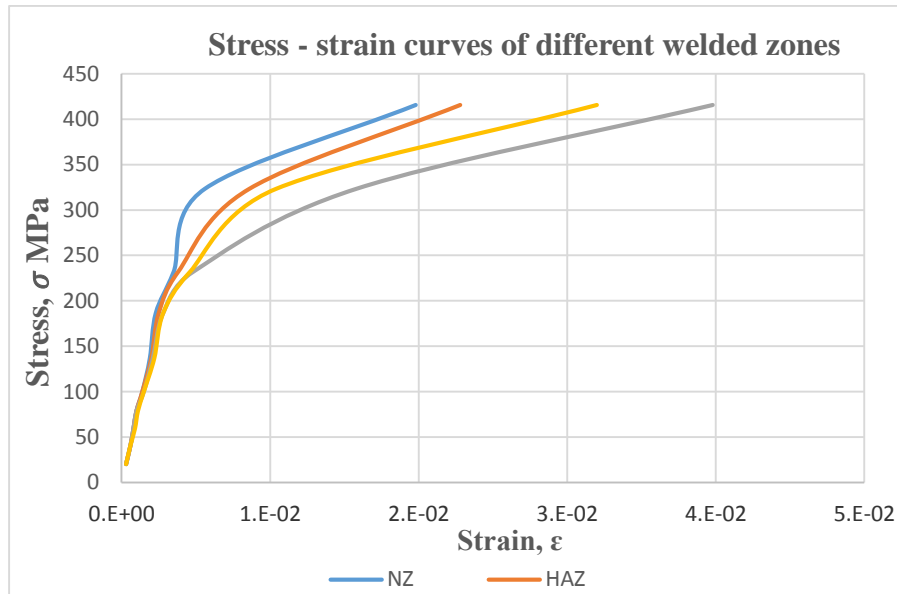


Figure 5.4 Stress–strain curves for different regions in welded joint

Because of this research, the fatigue initiation life at different loading cycles and crack length was found. 3D numerical simulations are performed using Abaqus code for analyses of Fatigue crack growth in friction stir welded T-joint. The analysis is performed using both Abaqus FEA and Morfeo engineering softwares.

There are two different kinds of testing were numerically modelled with different geometry including crack length and location:-

- Static pure Three - point bending test specimen with crack located in the center edge of the specimen opposite to the applied loading with same loading level 10 MPa and crack length of $a = 2.5$ mm for both butt and T welded joint.
- Pure Tensile test specimen with crack located in the area of TMAZ with tension stress 50 MPa and crack length of $2a = 6$ mm for all cases.

5.6.2 Finite element modelling of T welded joint under static pure Three - Point Bending Load

This study presents three-point bending analysis of butt and T welded joint plate using the finite element method. The plate geometry was recreated and a finite element mesh was generated using software ABAQUS. The finite element model of the welded

structure was developed and a quasi-static three-point bending test was simulated in ABAQUS.

5.6.2.1 Finite element model of a Three - Point Bending sample (butt welded plate)

In this study, the fatigue of welded butt joint under constant cyclic loading was numerically modeled. For this purpose, fatigue three point bending test were applied; the fatigue life and crack growth rate in specimens were examined. Subsequently, the fatigue behavior of welded joint and crack growth in specimens numerically modeled using ABAQUS.

Below is the analysis of crack propagation in butt-welded plate. The aim of the analysis is to observe the crack propagation in the structure, as well as consideration values of the stress intensity factor when crossing a crack from base material into the welded regime.

Fatigue pre-cracked specimens for three-point bending were machined from the welded butt joints so that they could be used in the fatigue crack propagation tests, using length $L = 176$ mm, width $W = 30$ mm and thickness $B = 5$ mm in accordance with ASTM E-399 (Figure 5.5). An initial crack was made in the opposite side of the applied load that allowed the specimen to be pre-cracked up to an initial length (a_0) 2.5mm at stress ratio $R=0$ and fatigue loading of 10MPa.

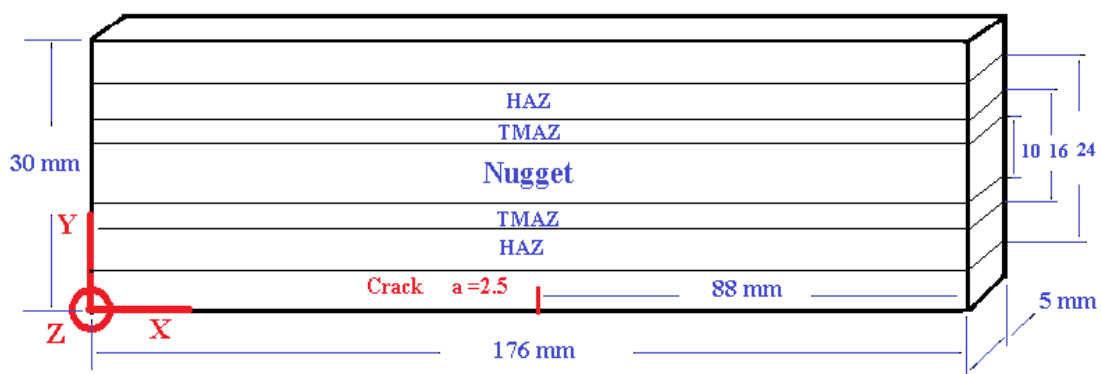


Figure 5.5 Crack welded plate model

5.6.2.2 Mesh

In Abaqus, a plate with a transitional initial crack is formed (Figure 5.6). The boundary conditions (clamping) are defined on the side. Hexahedra mesh is generated (Figure 5.7), where it is executed shrinking in the vicinity of the tips of the initial crack, as well as in the region assumed for further propagation.

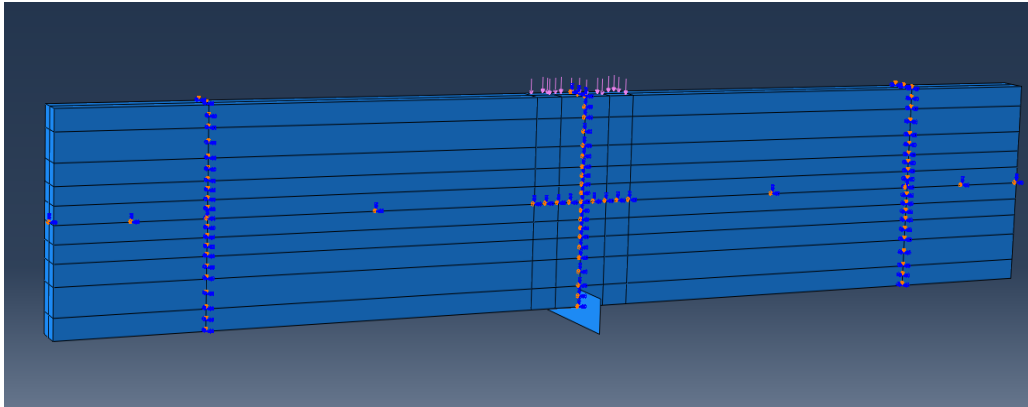


Figure 5.6 3D model of butt joint with all boundary conditions (ABAQUS model)

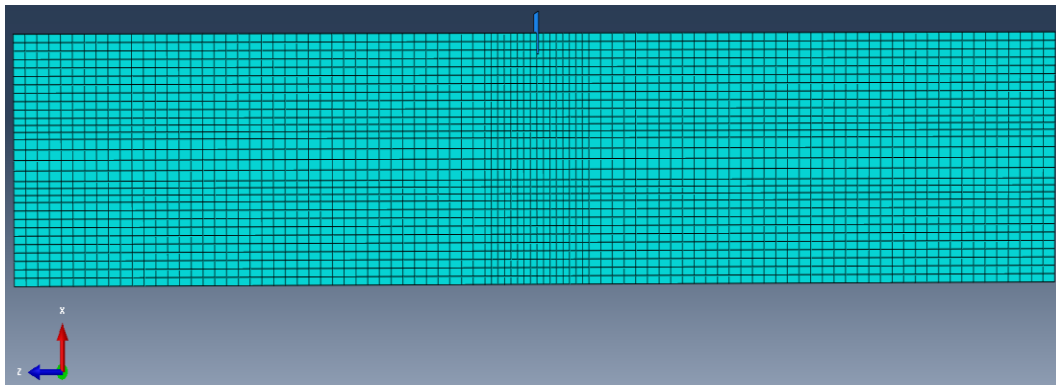


Figure 5.7 Finite Element mesh

5.6.2.2.1 SIF evaluation for the case of an unstiffened plate (butt joint)

The applied loading is a relatively small value (10MPa), and the reason for this is to analyze the behavior of the plate under the action of small loads, as well as the analysis of the increase in the crack length- a with the change in the number of load cycles- N (Figure 5.15). Since the crack propagates in all three directions (xyz), the crack propagation rate depends on the initial crack values, as well as the density of the generated mesh in the cracked area.

Furthermore, the cracks propagation in the panel is considered in a thin-walled plate (elasticity region)

The calculations obtained including stress intensity factors and crack growth data given as a function of load cycles N and crack length are shown in Table 5.2, Table 5.3, Figure 5.12 and Figure 5.13.

Table 5.2 Numerical data: change of stress intensity factor and crack growth rate with crack length

Butt welded joint			
Crack length a, mm	KI	da/dN	N
2.5	209.458	0.001659	0
3.4997	245.22	0.002498	602.422
4.4994	274.469	0.003412	1002.612
5.49904	302.415	0.004425	1295.622
6.48942	329.132	0.005753	1519.436
7.48906	359.395	0.007458	1693.2
8.48821	392.894	0.009737	1827.172
9.48761	430.985	0.013338	1929.815
10.48659	489.56	0.018155	2004.7134
11.47802	530.526	0.02316	2059.3225
12.47548	575.425	0.031552	2102.3912
13.47891	657.385	0.045871	2134.1939
14.476064	744.127	0.063876	2155.9323
15.47346	819.736	0.087666	2171.5468
16.46999	927.463	0.119391	2182.9141
17.48009	994.56	0.156511	2191.37452
18.43767	1175.85	0.261979	2197.49283
19.45764	1342.37	0.371825	2201.38615
20.43901	1531.56	0.594995	2204.02548
21.43474	1856.26	1.102931	2205.69899
22.42933	2370.59	2.235592	2206.60076
23.42817	2976.13	4.992743	2207.04755
24.42571	4384.8	20.60424	2207.247348

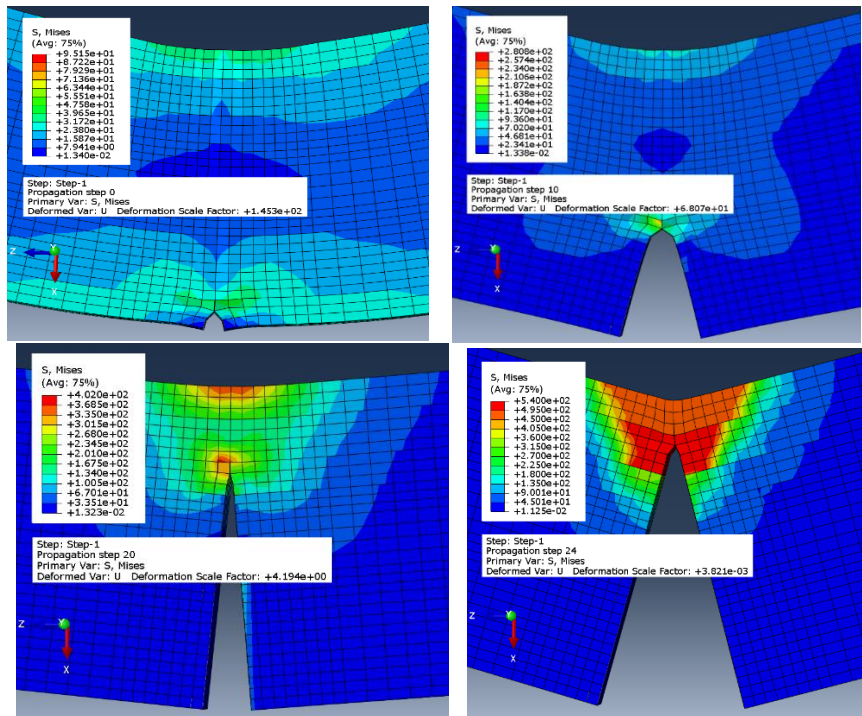


Figure 5.8 Von Mises stresses at crack tip and crack opening at different steps

5.6.2.3 Finite element model of a Three - Point Bending sample (T joint welded plate)

This part focuses on T-joints because of their complex behavior and their extensive application in engineering structures, such as T-stiffeners in aeronautical structure.

The fatigue of welded T joint under constant cyclic loading was numerically modeled. For this purpose, fatigue three point bending test were applied; the fatigue life and crack growth rate in specimens were examined. The stiffener and the base plate have the same dimensions, $L = 176$ mm, width $W = 30$ mm and thickness $B = 5$ mm in accordance with ASTM E-399 (Figure 5.9). The plate consists of one material region of aluminum alloy AA2024- T351, with mechanical properties as shown in Table 5.1 and Figure 5.4. An initial crack was made in the opposite side of the applied load that allowed the specimen to be pre-cracked up to an initial length (a_0) 2.5mm at stress ratio $R=0$ and fatigue loading of 10MPa. width of 30mm and thickness of 5mm to be welded to the same dimensions of base material butt joint. The fatigue loading and the loading ratio are the same as the Butt joint.

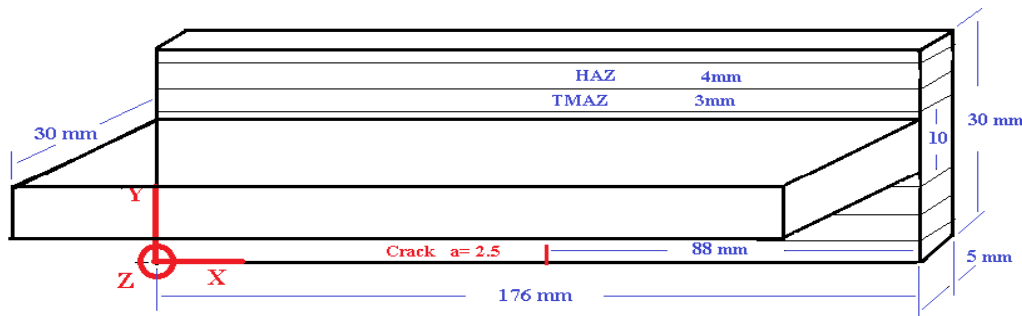


Figure 5.9 Crack welded plate

5.6.2.3.1 SIF evaluation for the case of stiffened plate (T welded joint)

In Abaqus, a plate with a transitional initial crack is formed (Figure 5.10). The boundary conditions (clamping) are defined on the side. Hexahedra mesh is generated (Figure 5.11), where it is executed shrinking in the vicinity of the tips of the initial crack, as well as in the region assumed for further propagation.

In order to obtain precise results, experience knowledge is necessary from the field of FEM-Finite Element Method. It is necessary to define the type of elements that will apply to generate the final mesh, or whether the mesh will be tetrahedral or hexahedra. If it is about simpler models, the hexahedral mesh is the most acceptable. However, if the model

has slanted edges, curves, circular openings and / or holes and the like, the best is to use a tetrahedron mesh.

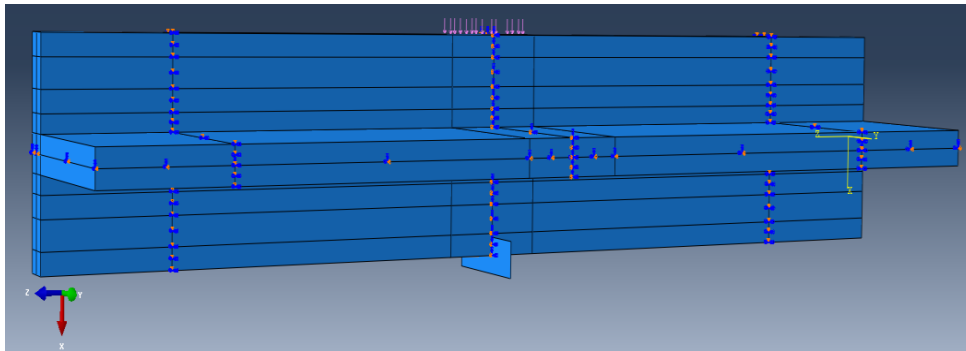


Figure 5.10 3D model of T welded joint

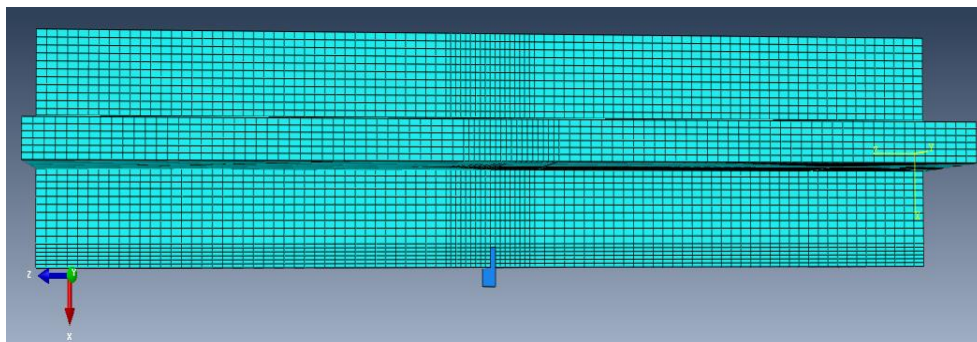


Figure 5.11 Finite Element mesh

The applied loading is a relatively small value (10MPa), and the reason for this is to analyze the behavior of the plate under the action of small loads, as well as the analysis of the increase in the crack length- a with the change in the number of load cycles- N (Figure 5.15). Since the crack propagates in all three directions (xyz), the crack propagation rate depends on the initial crack values, as well as the density of the generated mesh in the cracked area.

Furthermore, the cracks propagation in the panel is considered in a thin-walled plate (elasticity region)

In this example, an absolute elastic material is considered. It has been observed that the crack grows from one region to another and through stiffener, as well as the stress intensity factor calculations KI (Figure 5.12 and Figure 5.13).

Table 5.3 Numerical data: change of stress intensity factor and crack growth rate with crack length

T welded joint subjected to pure three point bending			
Crack length a, mm	KI	da/dN	N cycles
2.5	197.939	0.001351628	0
3.4986	224.59	0.00158048	738.813
4.3297	248.385	0.002488261	1264.666
5.32859	269.158	0.003083672	1666.107
6.33482	285.361	0.003551499	1992.416
7.33147	297.894	0.004143493	2273.044
8.36644	308.751	0.004179201	2522.826
9.32224	316.098	0.00455904	2751.53
10.36135	309.444	0.004029743	2979.453
11.31191	308.735	0.003585346	3215.339
12.23196	292.802	0.002821117	3471.953
13.20254	255.786	0.001845504	3815.994
14.226001	213.736	0.000767826	4370.564
15	172.141	0.000698402	5378.604
16.00176	162.915	0.000581348	6812.964
17.0023	152.244	0.000479402	8534.034
18.0025	142.865	0.000415235	10620.384
19.00254	137.803	0.000370846	13028.754
20.00254	132.325	0.000329067	15725.294
21.00244	127.051	0.000294263	18763.884
22.00234	122.602	0.000272047	22161.864
23.00234	120.355	0.000253874	25837.704
24.00214	117.023	0.000253874	29775.884
25.00204	113.935	0.000253874	34044.134
26.00194	111.259	0.000253874	38640.554
27.00184	108.53	0.000253874	43577.614
28.00184	106.021	0.000253874	48876.954

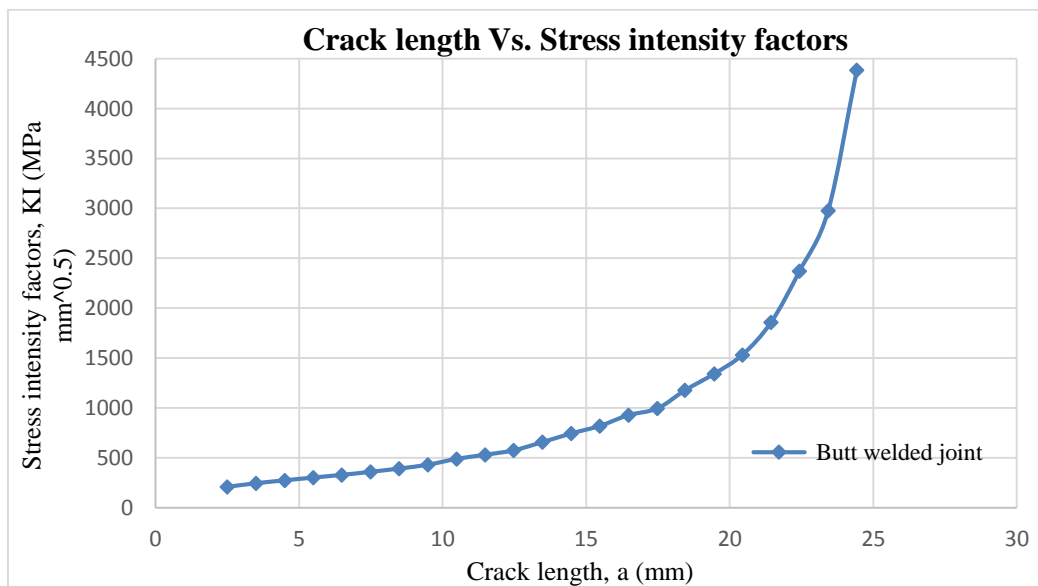


Figure 5.12 Change of stress intensity factor vs. crack length

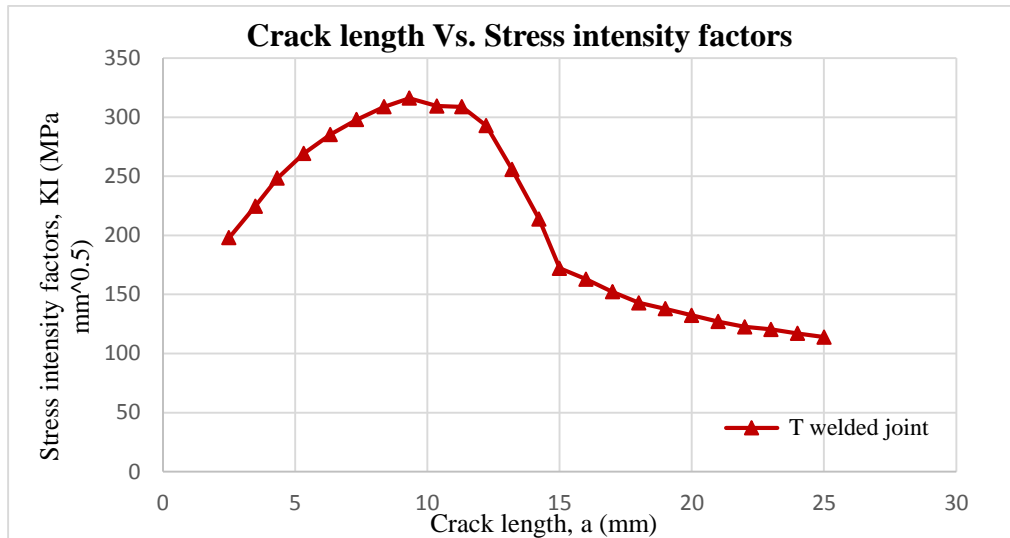


Figure 5.13 Change of stress intensity factor vs. crack length

In (Figure 5.12) butt-welded joint, one can notice that a large increase in stress intensity factor with an increase of crack length. This means that the growth of the cracks in the panel after a certain number of steps (reaching a certain crack length around crack length of 20mm) is no longer stable. Thus, there is a sudden progression of the crack in the structure, which leads to fracture. However, Figure 5.13, with one stiffener plate, it can be seen that the stress intensity factors are increased with the increase of crack length until reaches the stiffener then the SIFs decrease rapidly. After reaching the stiffener, the crack starts to propagate through stiffener by slowing the decrease in SIFs from crack length 15 to 20mm.

Figure 5.14 , a large increase in crack growth rate and SIFs in butt-welded plate comparing with a very small growth and increase of SIFs in the stiffened welded plate

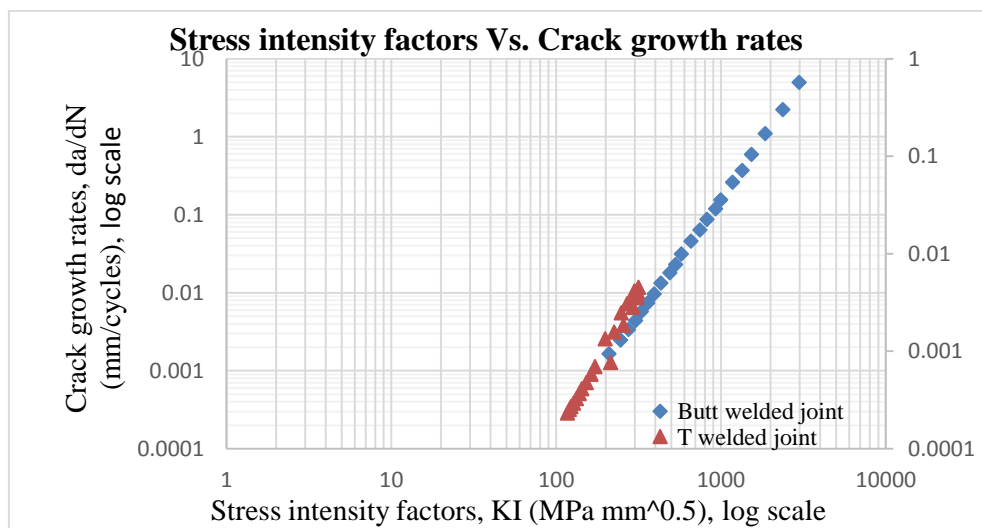


Figure 5.14 Change of stress intensity factor with crack growth rate da/dN

In Figure 5.15, it can be noticed that the fatigue life of butt welded plate is lower than in T welded plate that means the number of load cycles for crack length around 15mm is about (2160 cycles) for butt welded plate. For T welded plate with the same crack length (15mm) the number of load, cycles are larger (5378 cycles). The reason for the increase in number of load cycles is the stiffener (stringer) effect. The stiffeners can increase the life of the component by more than three times comparing with unstiffened components.

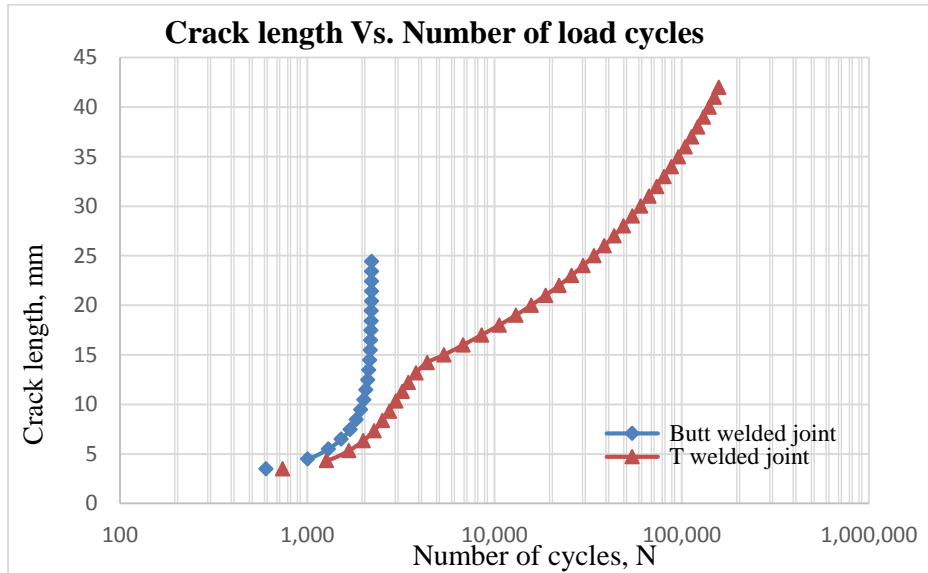


Figure 5.15 Crack propagation vs. cycle number – N

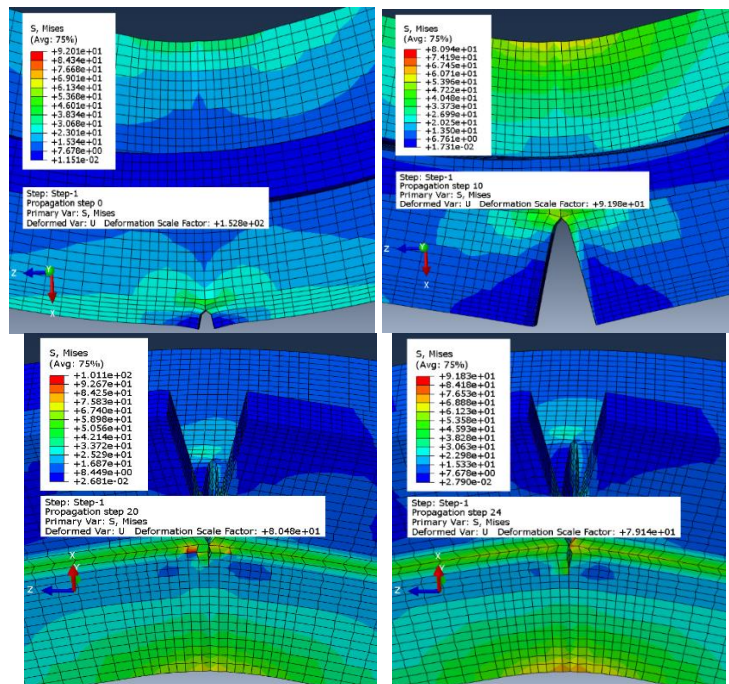


Figure 5.16 Von Mises stresses at crack tip and crack opening at different steps

Results and discussion

All simulation analyzes are performed using ABAQUS/Morfeo software. The calculations obtained including stress intensity factors and crack growth data given as a function of load cycles N and crack length. The stiffeners (stringers) indicate redistribute load, and increasing of the structural life of the material welded structure, at the same time stress intensity factors decrease when the crack reaches the stringer compared to unreinforced welded structure. Faster crack growth occurs in butt joint after load cycles number of approximately (1600 cycles and crack length of 7mm) because the crack tip reached the Nugget zone, as shown in the change of the curve slope in Figure 5.15. Figure 5.15 shows that during the propagation of the crack through the structure, change of its direction can be clearly seen after the crack propagation reaches the stringer; it grows vertically within the stringer and horizontally within the base material as it is shown in Figure 5.16. This is related to shear stresses within the structure leads to two additional fracture modes introduced by their stress intensity factors (KII,KIII) Stress intensity factors distribution with crack propagation steps for all modes (Mode I) can be seen in Table 5.2 and Table 5.3. The structure will maintain its integrity since the stress intensity factors is still smaller than the critical stress intensity factors (fracture toughness).

5.6.3 Finite element modelling of welded joint under static Tensile Load

This part aims to evaluate and simulate the mechanical behavior of friction stir welded plate made of AA 2024-T351 aluminum alloy under uniaxial tensile loading with crack located in the area of TMAZ and tension stress of 50 MPa with initial crack length of $2a = 6$ mm for all case studies.

A 3D numerical model, using FE analysis Abaqus/ CAE software package, was created to simulate the transverse tensile test of the welded aluminum plate. Isotropic, homogeneous and linear elastic behavior of material property was assumed. A symmetric about the longitudinal and transverse directions of the tensile sample was also considered to develop this model. The model was considered as a deformable body with appropriate yield criterion and stress–strain relations during nonlinear plastic. In the next part, effect of stiffeners and stress ratio was modelled and Abaqus/ Morefeo were used to display fatigue crack propagation results.

5.6.3.1 Effect of stiffeners on fatigue crack propagation of welded plate

In this section, the effects of stiffeners and mesh refinement on the values of stress intensity factor through the thickness of center-cracked plates are presented.

The main purpose of this analysis is to model the tensile behavior of a cracked stiffened panel in order to identify special features of that behavior, in particular as concerns bending effects.

When a crack is detected at a weld joint, it is necessary to assess the service life remaining until the crack grows and leads to the failure.

This part of the study focuses on the most typical fatigue cracks that start at the weld joint in TMAZ. The crack propagation was investigated under uniaxial tensile loading with constant amplitude (50 MPa).

5.6.3.1.1 Finite element model of tensile loading sample (butt welded plate)

Fatigue behavior of butt-welded plate under static tensile loading was numerically modeled. For this purpose, fatigue life and crack growth rate in specimens were examined.

Below is the analysis of crack propagation in butt-welded plate. The aim of the analysis is to observe the crack propagation in the structure, as well as consideration values of the stress intensity factor when crossing a crack from TMAZ and HAZ into the NUGGET and BM.

Fatigue pre-cracked specimens for tensile loading were machined from the welded butt joints so that they could be used in the fatigue crack propagation tests, using length $L = 170$ mm, width $W = 67$ mm and thickness $B = 5$ mm in accordance with ASTM E-399 (Figure 5.17). An initial crack was made in TMAZ that allowed the specimen to be pre-cracked up to an initial length (a_0) 3mm at stress ration $R=0$ and fatigue loading of 50MPa.

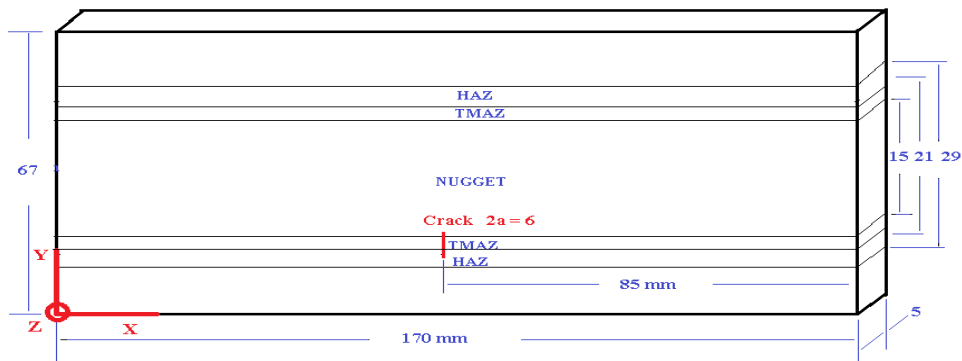


Figure 5.17 Crack welded plate

In Abaqus, a plate with a transitional initial crack is formed (Figure 5.18). The boundary conditions (clamping) are defined on the side. Hexahedra mesh is generated (Figure 5.19), where it is executed shrinking in the vicinity of the tips of the initial crack, as well as in the region assumed for further propagation.

In order to obtain precise results, experience knowledge is necessary from the field of FEM-Finite Element Method. It is necessary to define the type of elements that will apply to generate the final mesh, or whether the mesh will be tetrahedral or hexahedra. If it is about simpler models, the hexahedral mesh is the most acceptable.

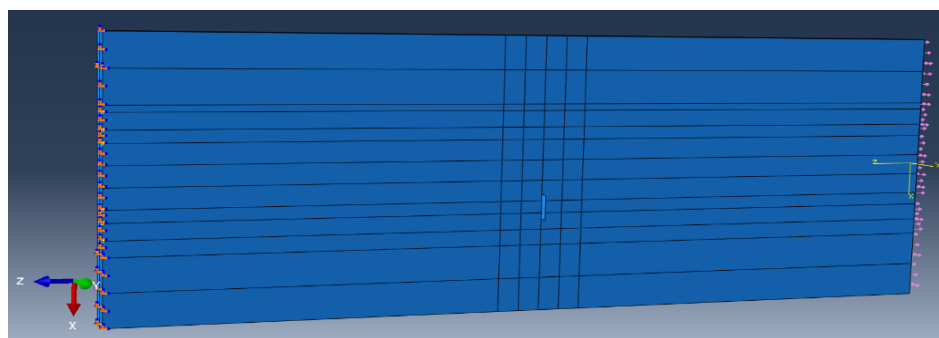


Figure 5.18 3D model of butt-welded joint

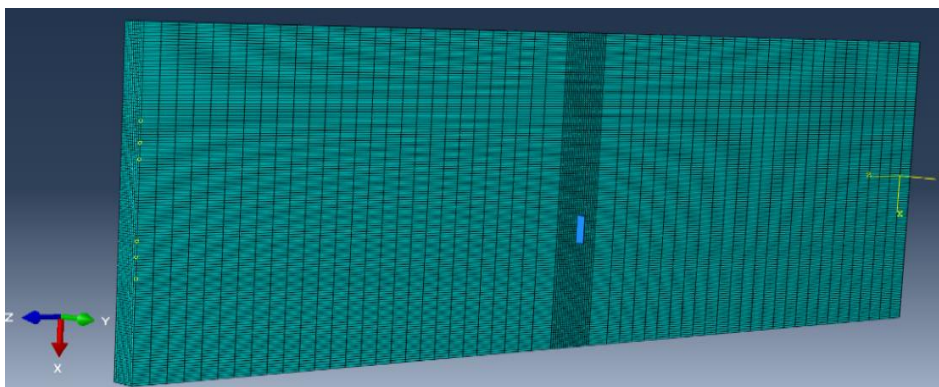


Figure 5.19 finite element mesh

5.6.3.1.2 SIF evaluation for the case of an unstiffened plate (butt joint)

Table 5.4 Numerical data of butt welded joint: change of stress intensity factor and crack growth rate with crack length

Right crack Tip (butt joint)				
Crack length, a mm	X	KI	da/dN	N, cycles
3	12	363.378	0.007416	0
3.8734	12.8734	402.638	0.011314	117.771
4.8349	13.8349	460.88	0.015215	202.7531
5.81	14.81	494.23	0.017796	266.8392
6.7084	15.7084	534.185	0.021174	317.3232
7.5527	16.5527	583.193	0.02991	357.1976
8.5256	17.5256	618.939	0.035684	389.7255
9.4837	18.4837	666.958	0.044643	416.5749
10.4662	19.4662	719.182	0.053266	438.5829
11.435	20.435	761.038	0.065026	456.7708
12.4343	21.4343	806.071	0.073422	472.1384
13.3883	22.3883	853.482	0.091492	485.1317
14.3953	23.3953	902.571	0.109144	496.1381
15.3763	24.3763	981.342	0.125833	505.1262
16.2801	25.2801	1048.38	0.167277	512.3088
17.275	26.275	1116.39	0.203559	518.2564
18.2792	27.2792	1188.9	0.244515	523.1896
19.3034	28.3034	1239.16	0.259274	527.3783
20.2933	29.2933	1265.93	0.273095	531.1963
21.2337	30.2337	1304.46	0.166466	534.6398

Left crack Tip (butt joint)			
Crack length, a mm	X	KI	da/dN
3	5.99995	372.023	0.008166
3.96176	5.03819	415.732	0.011557
4.94391	4.05604	463.961	0.015465
5.93501	3.06494	501.533	0.019667
6.92787	2.07208	546.84	0.025046
7.92658	1.07337	587.821	0.030686
8.92473	0.07521	627.821	0.037205
9.923676	-0.9237	669.763	0.044734
10.90819	-1.90824	712.208	0.052029
11.85448	-2.85453	760.81	0.064829
12.85075	-3.8508	804.178	0.075931
13.83734	-4.83739	847.323	0.08791
14.80491	-5.80496	876.521	0.101128
15.71386	-6.71391	907.524	0.110637
16.50851	-7.50856	945.641	0.109793
17.16152	-8.16157	991.295	0.139728
17.85083	-8.85088	1024.28	0.16503
18.54209	-9.54214	1066	0.165418
19.17365	-10.1737	1087.23	0.189343
19.82565	-10.8257	1106.47	0.211862
20.41135	-11.4114	1145.48	0.199304

5.6.3.1.3 Finite element model of tensile loading sample (T welded joint plate)

A typical aircraft fuselage is a stiffened shell structure, consisting of an external skin, stiffened by longitudinal stringer and lateral frame stiffeners. For current designs the skin and stringer are welded together to perform a T joint. Both stiffener and the skin plate have the same dimensions, $L = 170$ mm, width $W = 67$ mm and thickness $B = 5$ mm in accordance with ASTM E-399 (Figure 5.20). The T welded plate consists of one material region of aluminum alloy AA2024-T351, with mechanical properties as in the first case of butt-welded plate. An initial crack was made in the opposite side of the applied load that allowed the specimen to be pre-cracked up to an initial length (a_0) 3mm at stress ratio $R=0$ and fatigue loading of 50MPa.

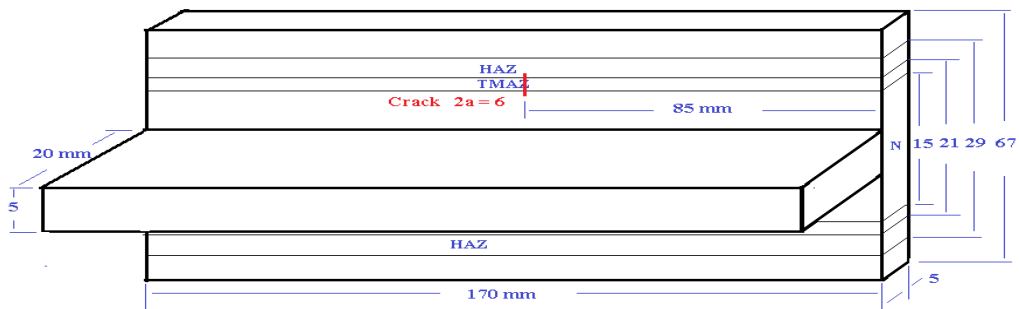


Figure 5.20 Crack welded plate

Figure 5.21 shows that applied tensile loading is introduced to one end and the other end is fixed. The crack is introduced in TMAZ with length of $2a = 6$ mm. mesh is generated where it is executed shrinking in the vicinity of the tips of the initial crack, as well as in the region assumed for further propagation Figure 5.22.

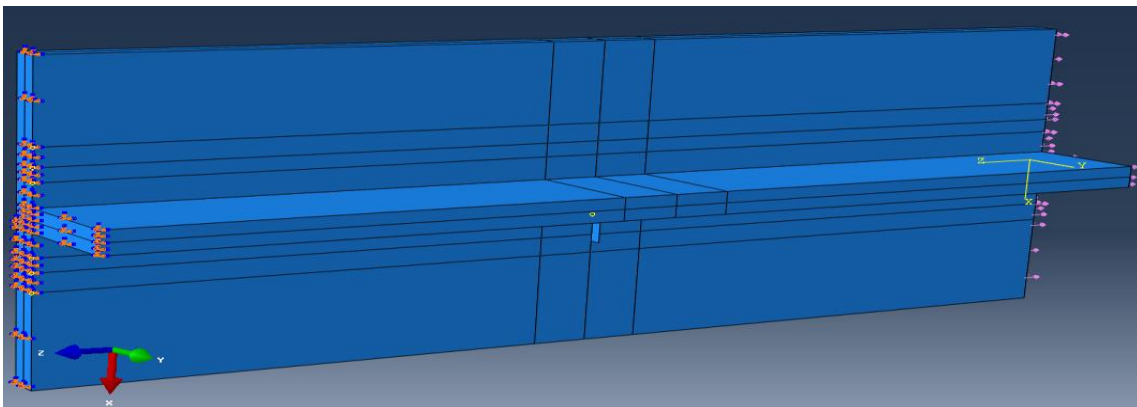


Figure 5.21 3D model of butt welded joint

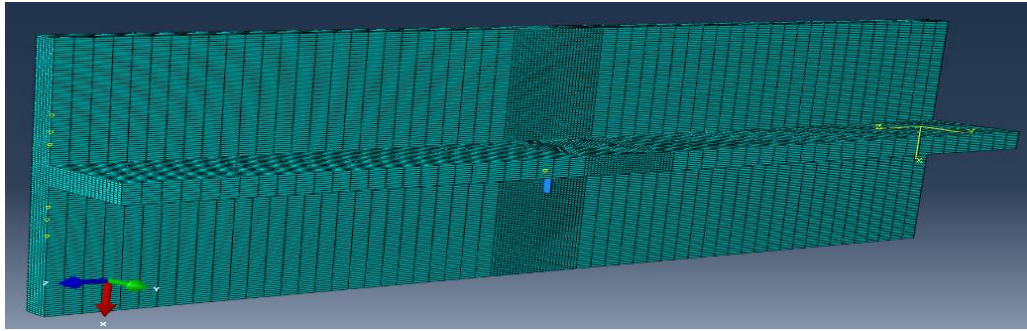


Figure 5.22 finite element mesh

5.6.3.1.4 SIF evaluation for the case of stiffened plate (one stiffener T joint)

Table 5.5 Numerical data of one stiffener(T welded joint): change of stress intensity factor and crack growth rate with crack length

Right crack Tip (one stiffener T joint plate)				
Crack length, a mm	X	KI	da/dN	N, cycles
3	12	360.31	0.00760	0
3.923	12.9232	396.159	0.01014	121.455
4.8108	13.8108	459.035	0.01533	208.9137
5.8094	14.8094	503.027	0.01937	274.0116
6.8096	15.8096	535.749	0.02318	325.6339
7.809	16.809	568.425	0.02723	368.7399
8.808	17.808	597.362	0.03034	405.4272
9.7792	18.7792	623.454	0.03714	437.4365
10.806	19.8065	660.62	0.04249	465.0919
11.8058	20.8058	695.816	0.04954	488.6079
12.8048	21.8048	733.498	0.05779	508.7726
13.804	22.804	772.575	0.06032	526.0605
14.754	23.7544	809.785	0.07450	543.3484
15.742	24.7426	845.828	0.08844	558.452
16.730	25.7309	881.872	0.09831	571.753
17.719	26.7191	917.916	0.11034	584.153
18.707	27.7073	953.959	0.12314	594.624

Left crack Tip (one stiffener T joint plate)			
Crack length, a mm	X	KI	da/dN
3	5.99995	367.577	0.008162529
3.99138	5.00857	412.276	0.011432596
4.99126	4.00869	456.654	0.015131364
5.97628	3.02367	490.826	0.017907958
6.90073	2.09922	524.809	0.021828284
7.84166	1.15829	545.432	0.024075225
8.724915	0.27503	551.82	0.024612503
9.512744	-0.51279	564.581	0.026697354
10.25107	-1.25112	586.933	0.030841129
10.97633	-1.97638	604.287	0.03051372
11.59163	-2.59168	629.68	0.038022548
12.24896	-3.24901	660.167	0.079634643
13.5035	-4.50357	736.474	0.063827413
14.3501	-5.35018	791.337	0.075765778
15.1967	-6.1967	837.674	0.084222723
16.0433	-7.0433	859.564	0.094529568
16.8899	-7.8900	911.439	0.105494861

5.6.3.1.5 Finite element model of tensile loading sample (double T welded joint plate)

Stiffeners improve the strength and stability of the structure and provide a means of slowing down or arresting the growth of cracks in a panel. Most commonly, stiffeners are connected to the skin by means of fasteners.

For current designs the skin and stringers are welded together to perform the doublet joint. Both stiffeners and have the same dimensions, $L = 170$ mm, width $W = 20$ mm and thickness $B = 5$ mm in accordance with ASTM E-399 (Figure 5.23). The T welded plate consists of one material region of aluminum alloy AA2024- T351, with mechanical properties as in the first case of butt-welded plate. An initial crack was made in TMAZ that allowed the specimen to be pre-cracked up to an initial length (a_0) 3mm at stress ration $R=0$ and fatigue loading of 50MPa.

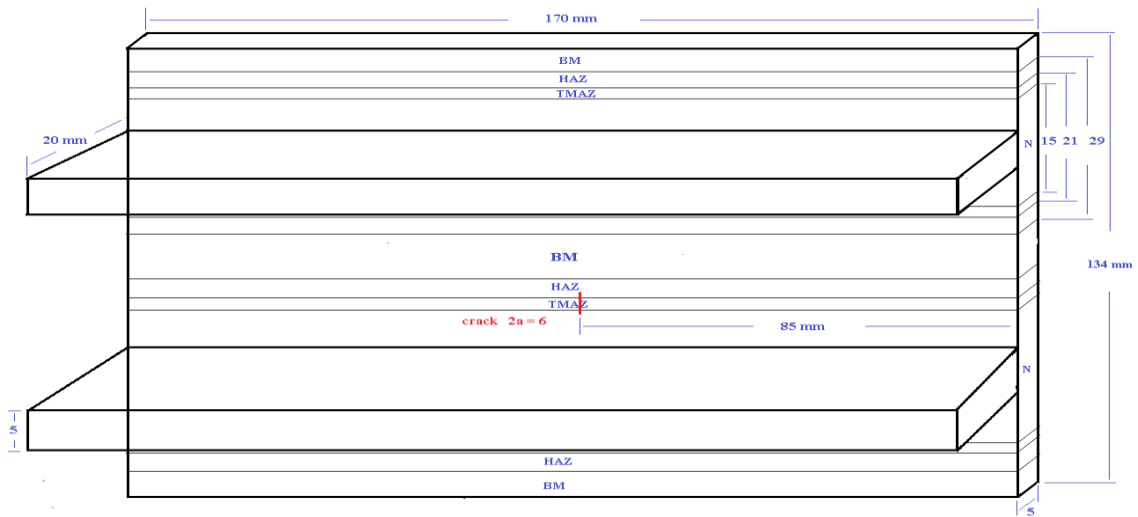


Figure 5.23 Crack welded plate

Figure 5.24 shows that applied tensile loading is introduced to one end and the other end is fixed. Two welded stiffeners connected to the skin producing double T welded joint plate. mesh is generated where it is executed shrinking in the vicinity of the tips of the initial crack, as well as in the region assumed for further propagation Figure 5.25.

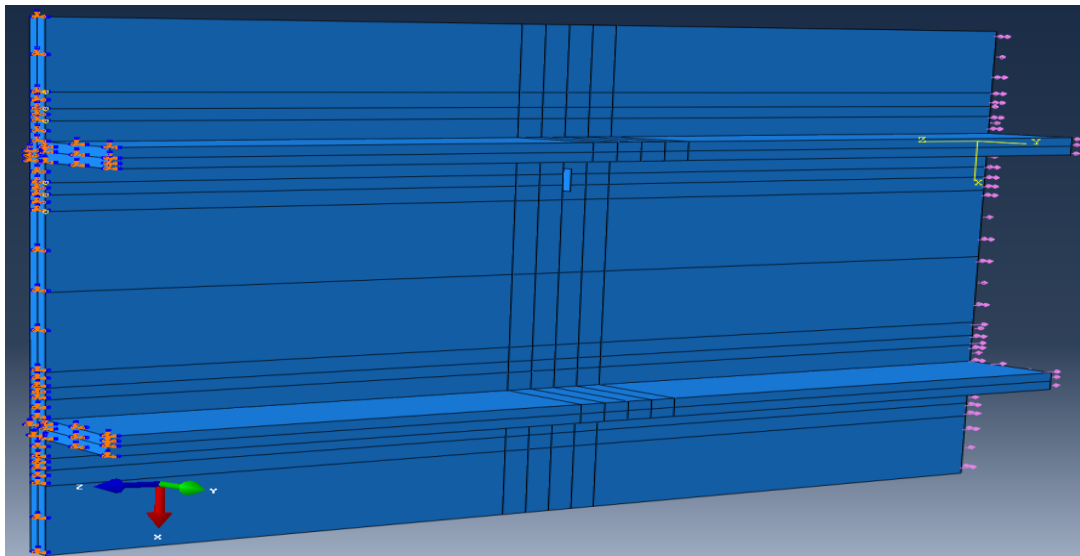


Figure 5.24 3D model of T welded joint

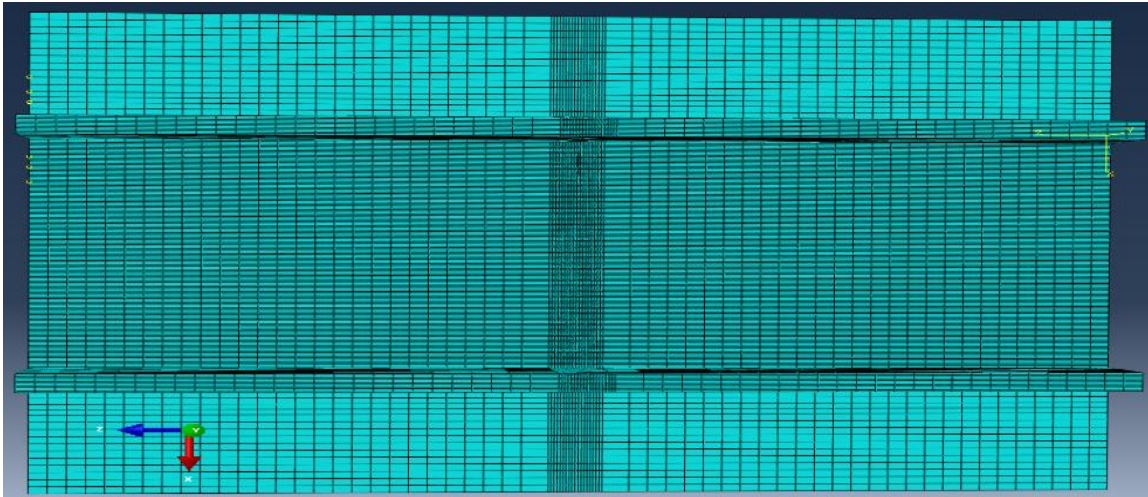


Figure 5.25 finite element mesh

5.6.3.1.6 SIF evaluation for the case of stiffened plate (Two stiffeners T joint)

Table 5.6 Numerical data of welded double T joint: change of stress intensity factor and crack growth rate with crack length

Right crack Tip (two stiffeners double T joint plate)				
Crack length , a mm	X	KI	da/dN	N
3	12	372.124	0.007411795	0
3.9071	12.9071	403.136	0.010876136	122.386
4.9093	13.9093	450.072	0.014533354	214.5327
5.8898	14.8898	496.353	0.019093241	281.9982
6.9006	15.9006	524.135	0.023013832	334.9384
7.9012	16.9012	549.832	0.026834588	378.4166
8.9003	17.9003	548.041	0.03033064	415.6484
9.899	18.899	615.88	0.033933565	448.5755
10.8989	19.8989	639.59	0.038030248	478.0419
11.8987	20.8987	665.654	0.042617681	504.3315
12.8984	21.8984	627.149	0.047497327	527.7889
13.8981	22.8981	649.815	0.052739856	548.8364
14.8979	23.8979	656.329	0.058655121	567.7936
15.8977	24.8977	688.035	0.065209729	584.839
16.8967	25.8967	797.312	0.07235013	600.1588
17.896	26.896	799.658	0.080254051	613.9708
18.8955	27.8955	802.018	0.089012183	626.425
19.895	28.895	868.256	0.099399328	637.6538
20.8945	29.8945	885.843	0.114310294	647.7092
21.8937	30.8937	976.614	0.124838106	656.4503
22.8412	31.8412	998.958	0.153328143	664.0402
23.7984	32.7984	1032.41	0.141332849	670.283

Left crack Tip (two stiffeners double T joint plate)			
Crack length , a mm	X	KI	da/dN
3	5.99995	365.806	0.007877617
3.96411	5.03584	402.041	0.01068112
4.94834	4.05161	453.86	0.015099273
5.96702	3.03293	488.456	0.018008432
6.92039	2.07956	534.226	0.02172261
7.86485	1.1351	566.749	0.024473407
8.776039	0.2239	593.057	0.023911489
9.563375	-0.5634	565.25	0.026543283
10.34551	-1.34556	576.24	0.027631078
11.07192	-2.07197	594.18	0.031018783
11.79954	-2.79959	691.047	0.035327711
12.5431	-3.54315	716.504	0.040077649
13.30286	-4.3029	741.851	0.040402689
13.99154	-4.9915	770.141	0.045376571
14.6867	-5.6867	719.541	0.053799595
15.42978	-6.4298	826.105	0.071456216
16.31971	-7.319	855.087	0.058863814
16.98068	-7.980	886.052	0.107137458
18.05799	-9.058	921.719	0.099742367
18.92985	-9.929	958.319	0.130371827
19.91935	-10.919	1014.34	0.162602798
20.93445	-11.934	1123.1	0.176288647

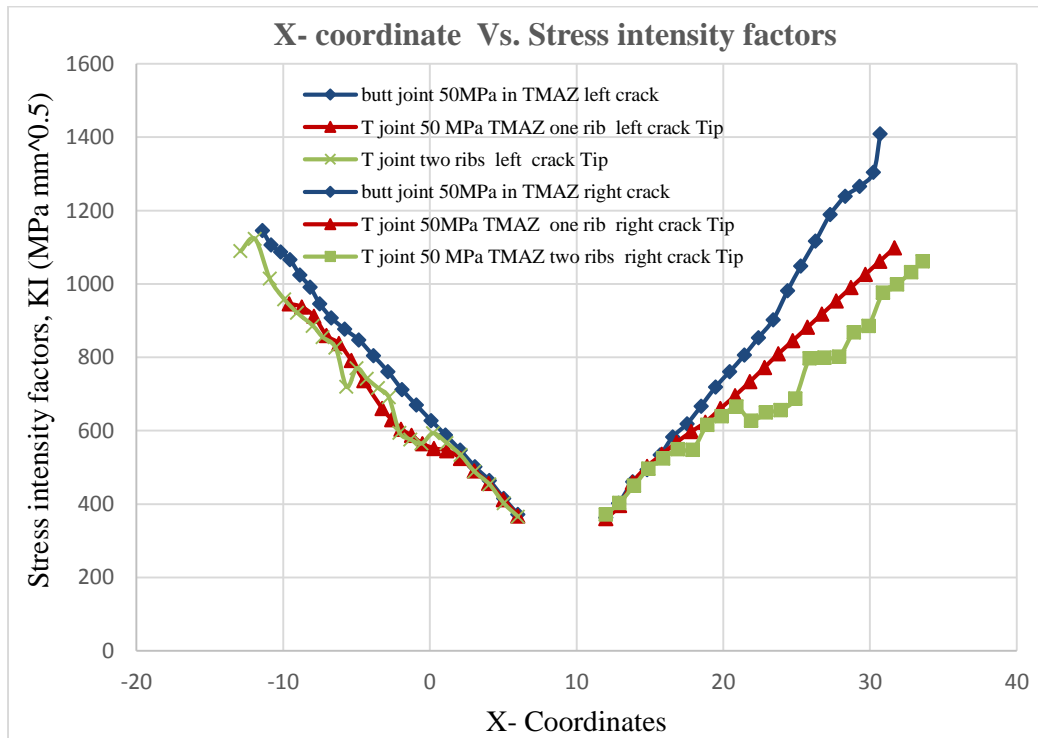


Figure 5.26 Change of stress intensity factor vs. X coordinates of crack

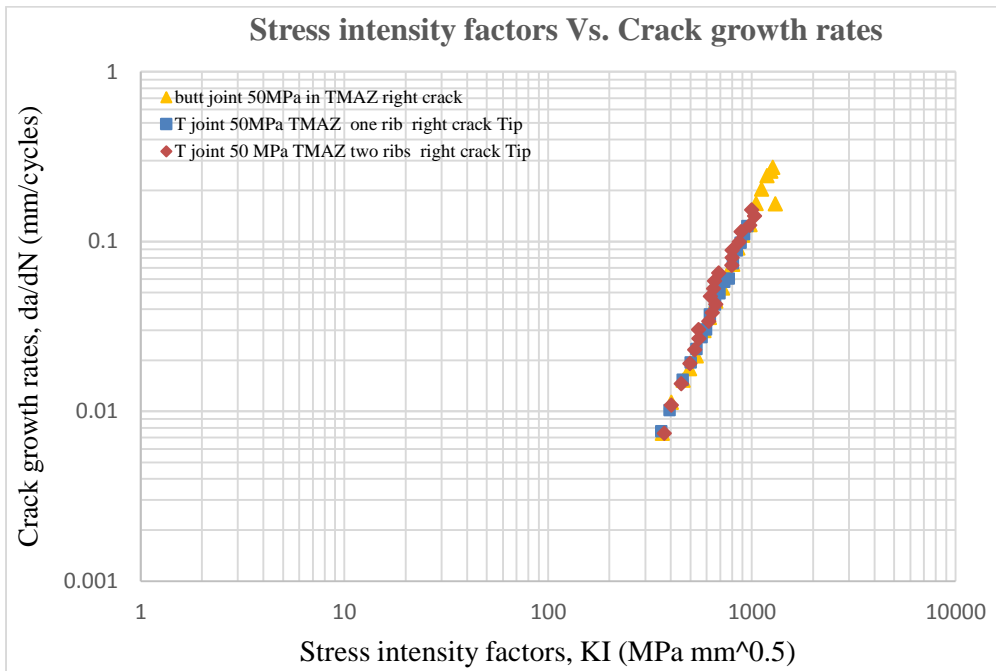


Figure 5.27 Change of stress intensity factor with crack growth rate da/dN- right crack Tip

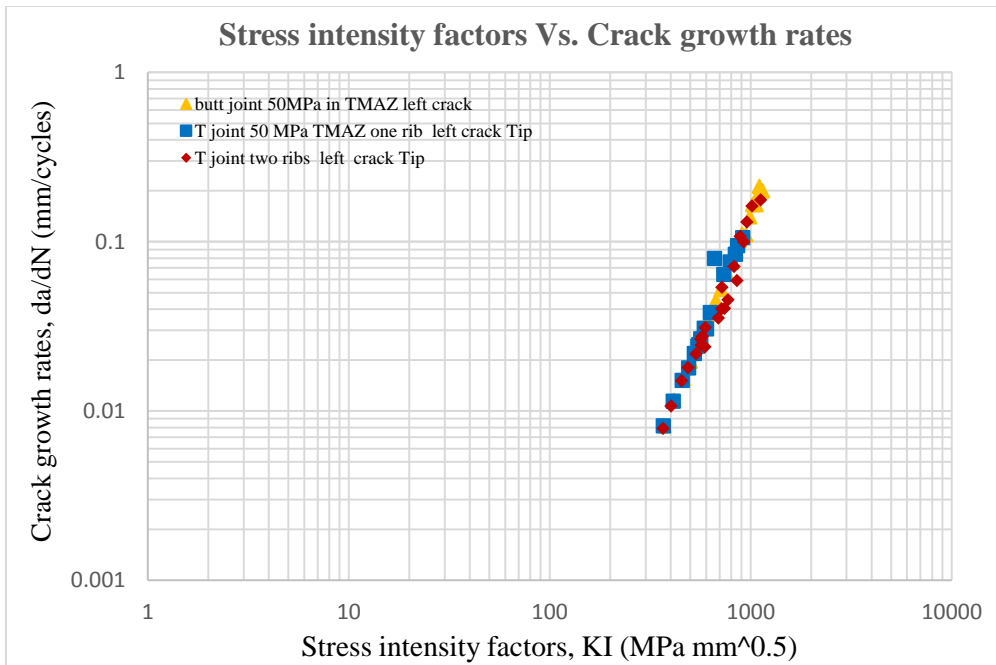


Figure 5.28 Change of stress intensity factor with crack growth rate da/dN- left crack Tip

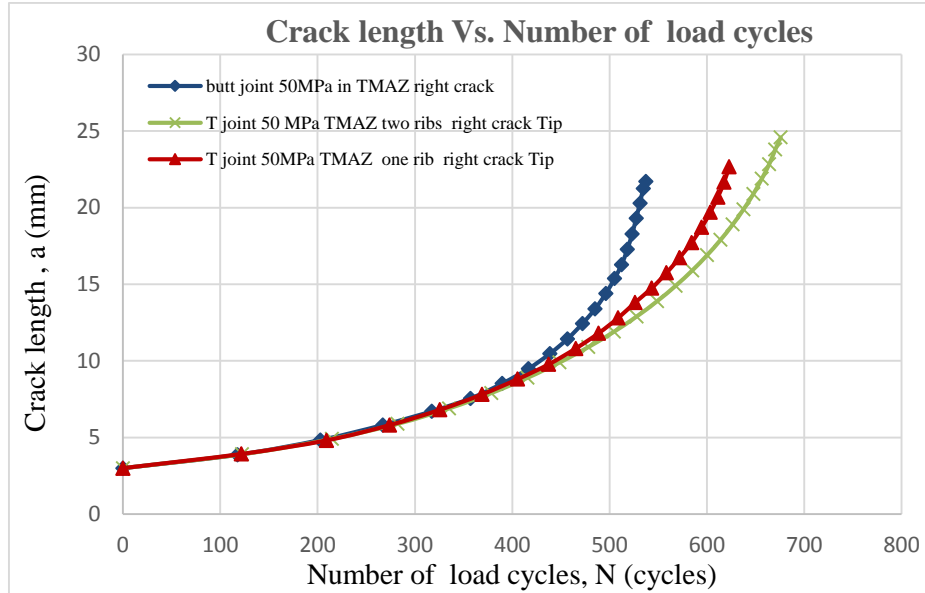


Figure 5.29 Crack propagation vs. cycle number – N

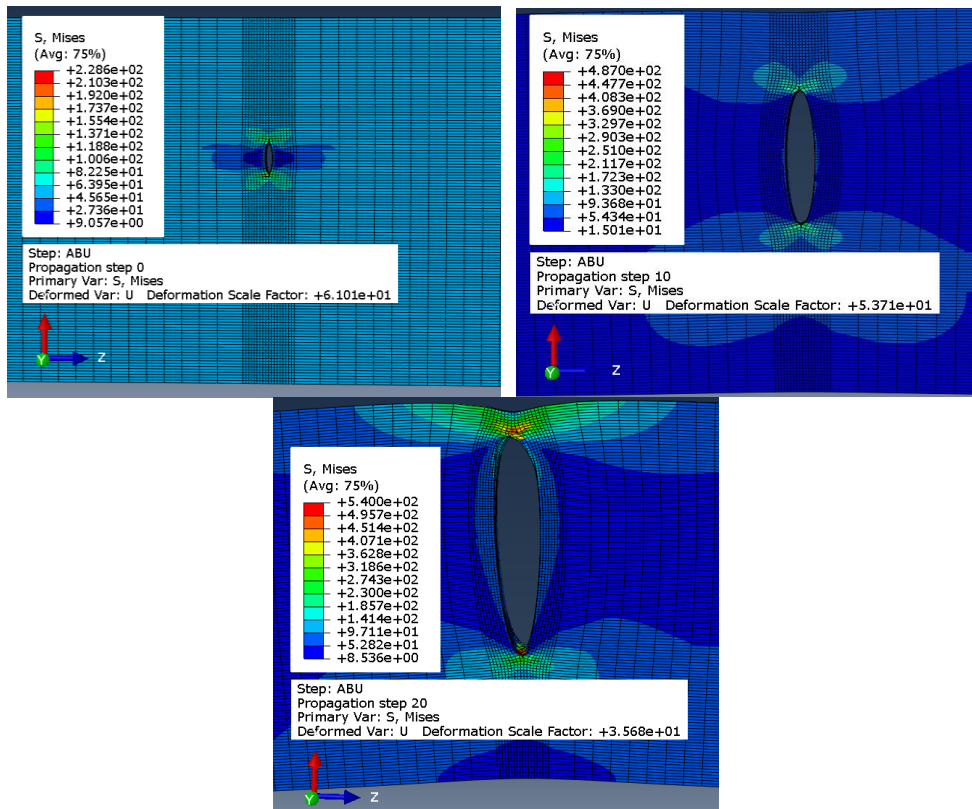


Figure 5.30 Von Mises stresses at crack tip and crack opening at different steps (butt welded plate)

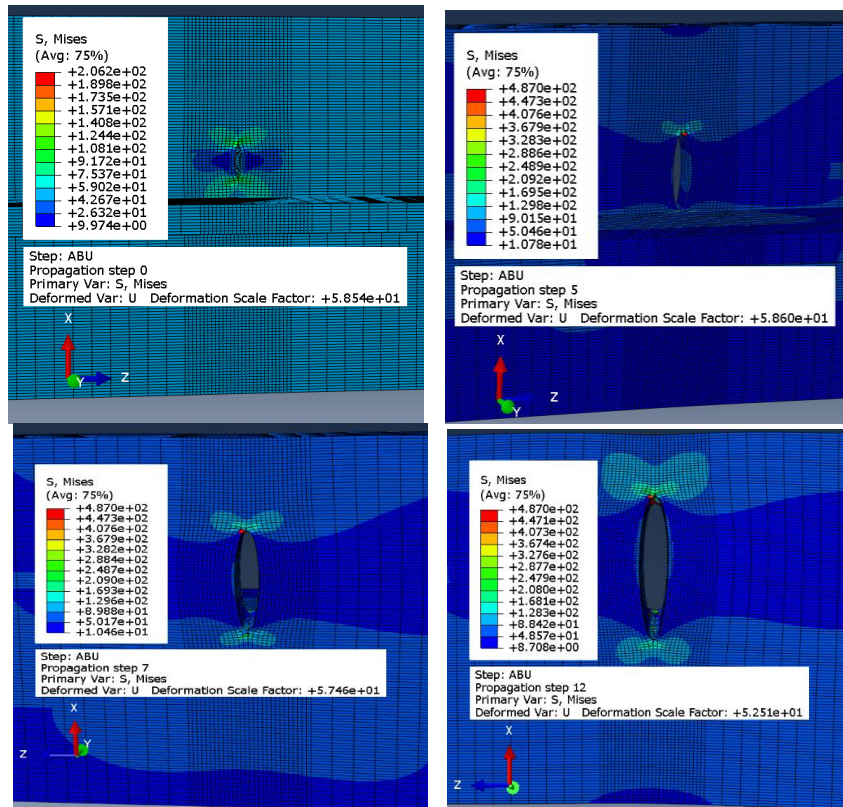


Figure 5.31 Von Mises stresses at crack tip and crack opening at different steps (T welded joint plate)

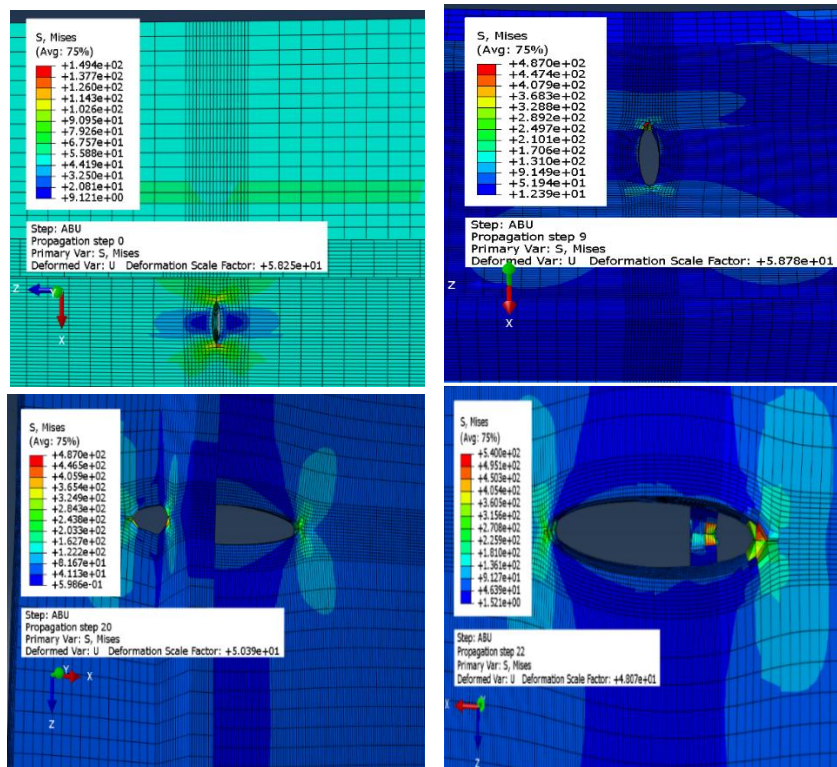


Figure 5.32 Von Mises stresses at crack tip and crack opening at different steps double T welded joint plate)

Results and discussion

Figure 5.26 shows comparison of the three cases (butt joint, one stiffener T joint and two stiffeners T joint) for both crack tips (right and left crack tips). Stress intensity factors have the same values for a small crack length (lower than 10mm) in both crack tips (right and left). However, at higher crack length (higher than 10mm), the values of SIF are increased differently. The calculations obtained including stress intensity factors and crack growth data given as a function of load cycles N and crack length for all different structures are shown in Table 5.4, Table 5.5 and Table 5.6, respectively.

During the propagation of the crack through the structure, change of its direction can be clearly seen after the crack propagation reaches the stringer; it grows vertically within the stringer and horizontally within the base material.

Crack length as a function of load cycles N is also given in Figure 5.29. It was decided to count the number of cycles from initial crack, until reaches the specific values and compare this value with the number of cycles in all three different welded joint. For butt-welded joint, faster crack growth, occurs after load cycles number of 400 and total number of cycle to reach a value of crack length 18mm is 520 cycles, as shown in the change of the curve slope.

For one stiffener T welded joint, faster crack growth occurs after load cycles number of 550 and total number of cycle to reach a crack length value of 18mm is 588 cycles.

For two stiffeners T welded joint, faster crack growth occurs after load cycles number of 650 and total number of cycle to reach a crack length value of 18mm is 615 cycles.

The stiffeners (stringers) indicate redistribute load, and increasing of the structural life of the material welded structure, at the same time stress intensity factors decrease when the crack reaches the stringer compared to unreinforced welded structure.

Finally, crack growth and von Mises stress distribution of different cases studied (butt, one stiffener and two stiffeners) are shown in Figure 5.30, Figure 5.31 and Figure 5.32, respectively for different steps, i.e. at the beginning (0 step) and after certain number of steps

5.6.3.2 Effect of stress ratio on fatigue crack propagation of double T welded joint plate

Fatigue cracks frequently grow during a large portion of the cyclically loaded components. Therefore, any parameter that significantly affects the growth of fatigue cracks can have a major effect on the total fatigue behavior of the components. One such parameter is the stress ratio (ratio of the minimum stress to the maximum stress). Accordingly, an investigation has been conducted to determine the effects of a wide range of values and stresses on fatigue-crack growth in 2024-T351 aluminum-alloy plate specimens. This material was selected because of its frequent use in aircraft construction.

Uniaxial-load fatigue-crack-propagation tests were conducted at stress ratios ranging from -1 to 0.5. Generally, tests were conducted at stress level (50 MPa) for a given stress ratio.

5.6.3.2.1 Finite element model of tensile loading sample (double T welded joint plate)

In the present work, fatigue crack growth rate of aluminum alloy AA2024 T351 plate welded by friction stir welding (FSW) has been studied under constant amplitude load with different values of R-ratio.

In order to investigate the effect of stress ratio on fatigue strength of welded joints, fatigue tests were carried out at stress ratio (R) of 0, 0.5, and -1 on double T joint plate previously studied.

The fatigue-crack-propagation data are presented in Table 5.7 plots of rate against the stress intensity range.

5.6.3.2.2 SIF evaluation for the case of stiffened plate (two stiffener T joint)

Table 5.7 Numerical data: change of stress intensity factor and crack growth rate with crack length

Right crack , R=-1			
Crack length, a mm	KI	da/dN, mm/cycles	N
3	365.806	0.056877536	0
3.9071	403.134	0.083688664	15.9483
4.912	450.026	0.111224608	27.9559
5.8898	496.356	0.146687251	36.74712
6.9017	534.234	0.17640476	43.64547
7.9011	566.753	0.205940129	49.31085
8.9002	593.071	0.232800434	54.16226
9.899	615.895	0.260399168	58.45263
10.8988	639.599	0.29191348	62.29212
11.8987	665.705	0.327055713	65.71745
12.8983	691.046	0.362668417	68.77381
13.8929	716.555	0.404959949	71.51626
14.8929	742.008	0.45225814	73.98564
15.8977	769.839	0.499887424	76.20738
16.8968	797.006	0.55415687	78.20603
17.8961	825.373	0.614007605	80.00931
18.8956	854.083	0.680924706	81.63714
19.895	885.256	0.760119211	83.10485
20.8948	920.264	0.87179174	84.42017
21.8941	957.267	0.956947902	85.56643
22.8458	997.839	1.16935405	86.560946

Right crack , R=0			
Crack length, a mm	KI	da/dN, mm/cycles	N
3	372.124	0.007411795	0
3.9071	403.136	0.010876136	122.386
4.9093	450.072	0.014533354	214.5327
5.8898	496.353	0.019093241	281.9982
6.9006	524.135	0.023013832	334.9384
7.9012	549.832	0.026834588	378.4166
8.9003	548.041	0.03033064	415.6484
9.899	615.88	0.033933565	448.5755
10.8989	639.59	0.038030248	478.0419
11.8987	665.654	0.042617681	504.3315
12.8984	627.149	0.047497327	527.7889
13.8981	649.815	0.052739856	548.8364
14.8979	656.329	0.058655121	567.7936
15.8977	688.035	0.065209729	584.839
16.8967	797.312	0.07235013	600.1588
17.896	799.658	0.080254051	613.9708
18.8955	802.018	0.089012183	626.425
19.895	868.256	0.099399328	637.6538
20.8945	885.843	0.114310294	647.7092
21.8937	976.614	0.124838106	656.45032
22.8412	998.958	0.153328143	664.04015

Right crack , R=0.5			
Crack length, a mm	KI	da/dN	N Cycles
3	365.806	0.000965814	0
3.9071	403.136	0.001417248	939.208
4.9093	450.072	0.001893815	1646.353
5.8898	496.353	0.002490714	2164.091
6.9017	534.226	0.0029956	2570.36
7.9012	566.749	0.003496768	2904.016
8.9003	593.057	0.00395232	3189.737
9.899	615.88	0.004421832	3442.424
10.8989	639.59	0.004956134	3668.552
11.8988	665.654	0.005552901	3870.302
12.8984	691.049	0.006158332	4050.316
13.8931	716.502	0.006873655	4211.837
14.8931	741.843	0.007680487	4357.32
15.8977	770.191	0.00849909	4488.119
16.8967	797.37	0.009429227	4605.661
17.896	826.131	0.010459583	4711.64
18.8955	855.172	0.01160695	4807.1983
19.895	886.399	0.012969083	4893.3105
20.8945	922.184	0.01493943	4970.3784
21.8938	958.472	0.016265292	5037.2685
22.8374	999.626	0.019931802	5095.2816

Left crack , R=-1		
Crack length a ,mm	KI	da/dN
3	372.121	0.060453465
3.96413	402.044	0.081970585
4.9484	453.861	0.115878115
5.96711	488.465	0.138208412
6.92052	524.159	0.16671962
7.86505	549.785	0.187769329
8.775996	548.049	0.18350422
9.563297	565.243	0.203689292
10.34536	576.32	0.212137225
11.072	594.188	0.23804133
11.79954	627.191	0.271169939
12.54321	649.82	0.307644024
13.3029	656.284	0.262780523
13.88673	687.971	0.323523378
14.53334	718.738	0.49698882
15.42955	798.866	0.196193706
15.74892	798.964	0.929625062
16.5261	837.1807	0.71521759
17.11334	865.674	0.757192958
18.05408	882.842	-19.02636056
18.92202	974.07	25.57832118

Left crack , R=0		
Crack length a , mm	KI	da/dN,mm/cycles
3	365.806	0.007877617
3.96411	402.041	0.01068112
4.94834	453.86	0.015099273
5.96702	488.456	0.018008432
6.92039	534.226	0.02172261
7.86485	566.749	0.024473407
8.776039	593.057	0.023911489
9.563375	565.25	0.026543283
10.34551	576.24	0.027631078
11.07192	594.18	0.031018783
11.79954	691.047	0.035327711
12.5431	716.504	0.040077649
13.30286	741.851	0.040402689
13.99154	770.141	0.045376571
14.6867	719.541	0.053799595
15.42978	826.105	0.071456216
16.31971	855.087	0.058863814
16.98068	886.052	0.107137458
18.05799	921.719	0.099742367
18.92985	958.319	0.130371827
19.91935	1014.34	-3.190761547

Left crack , R=0.5		
Crack length a, mm	KI	da/dN,mm/cycles
3	372.124	0.001026514
3.96411	402.041	0.00140001
4.95412	453.732	0.001956414
5.96703	488.456	0.002346647
6.9204	524.138	0.00283067
7.86487	549.824	0.003188982
8.776029	548.042	0.003115859
9.563366	565.249	0.003458767
10.34549	576.248	0.003600694
11.07193	594.181	0.004042075
11.79956	627.138	0.004603179
12.54307	649.726	0.005220335
13.30254	656.414	0.004457909
13.88563	688.024	0.005496163
14.53166	719.708	0.008476962
15.43004	799.116	0.003399495
15.75489	801.993	0.015764549
16.5761	842.599	0.008715561
17.11241	868.625	0.017150969
17.7841	885.592	-0.326328536
18.93133	978.177	0.436640354

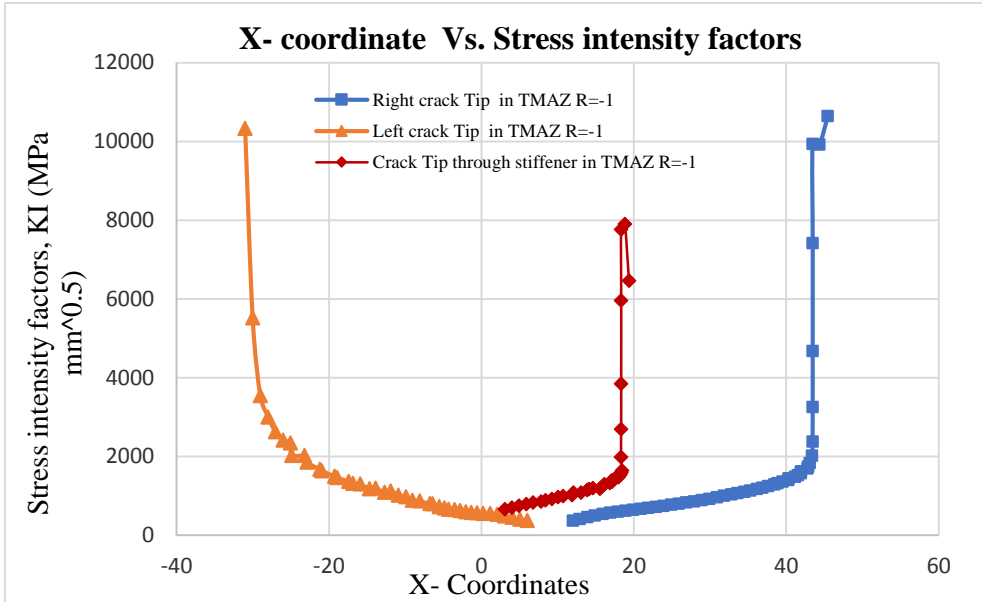


Figure 5.33 Change of stress intensity factor vs. X coordinates of crack

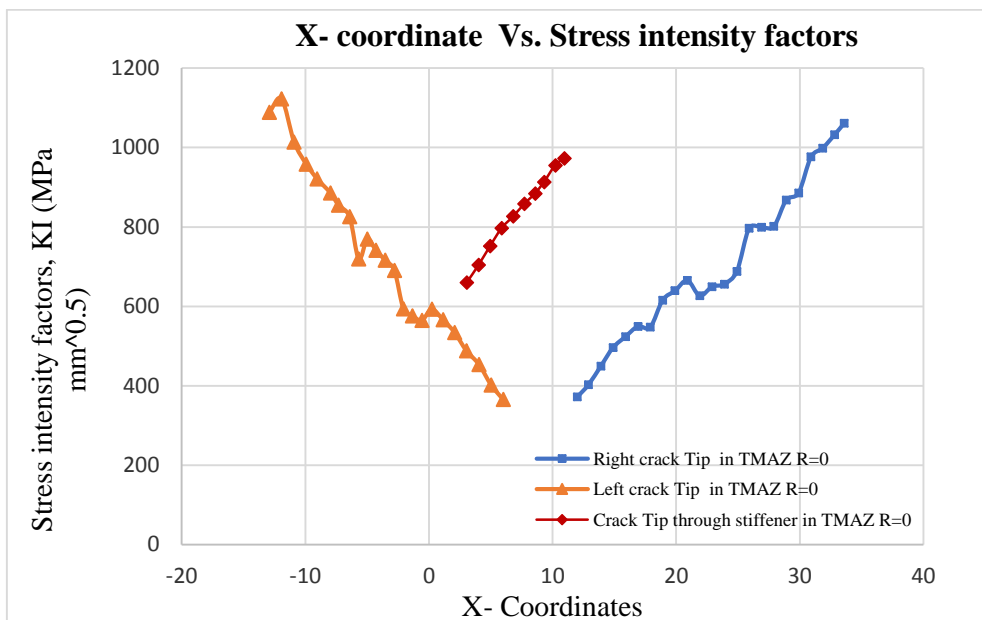


Figure 5.34 Change of stress intensity factor vs. X coordinates of crack

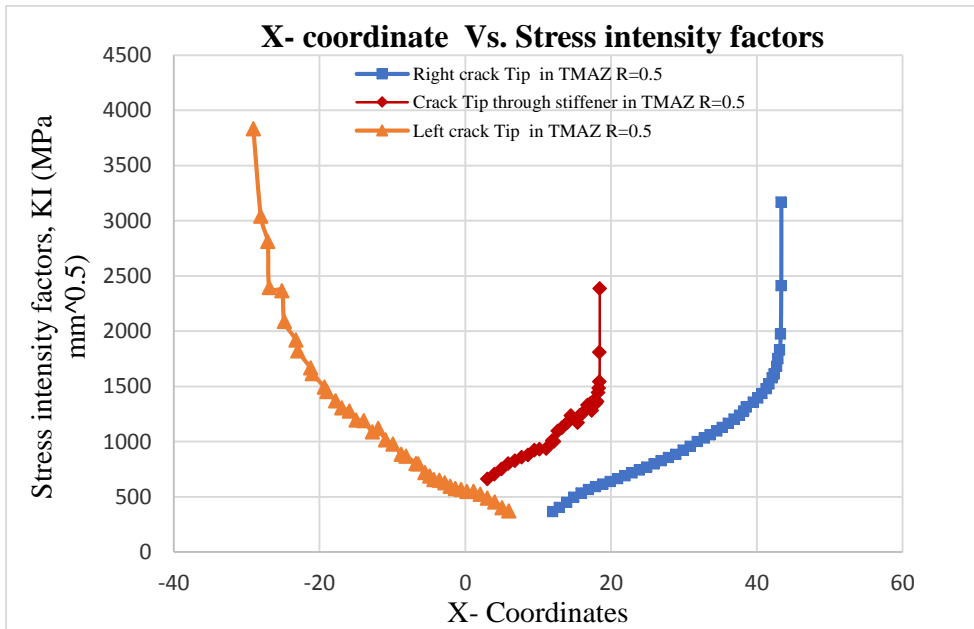


Figure 5.35 Change of stress intensity factor vs. X coordinates of crack

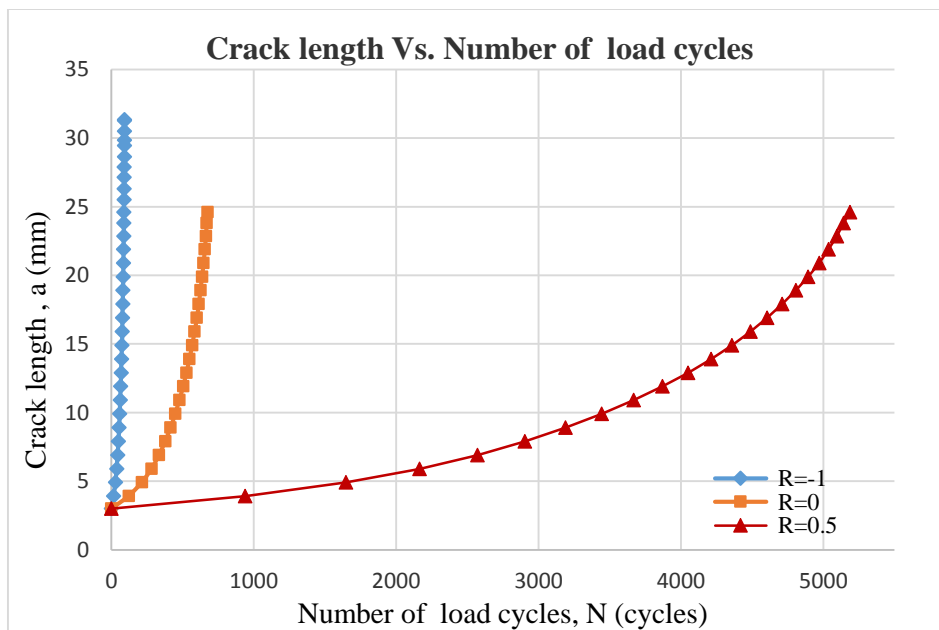


Figure 5.36 Crack propagation vs. cycle number – N

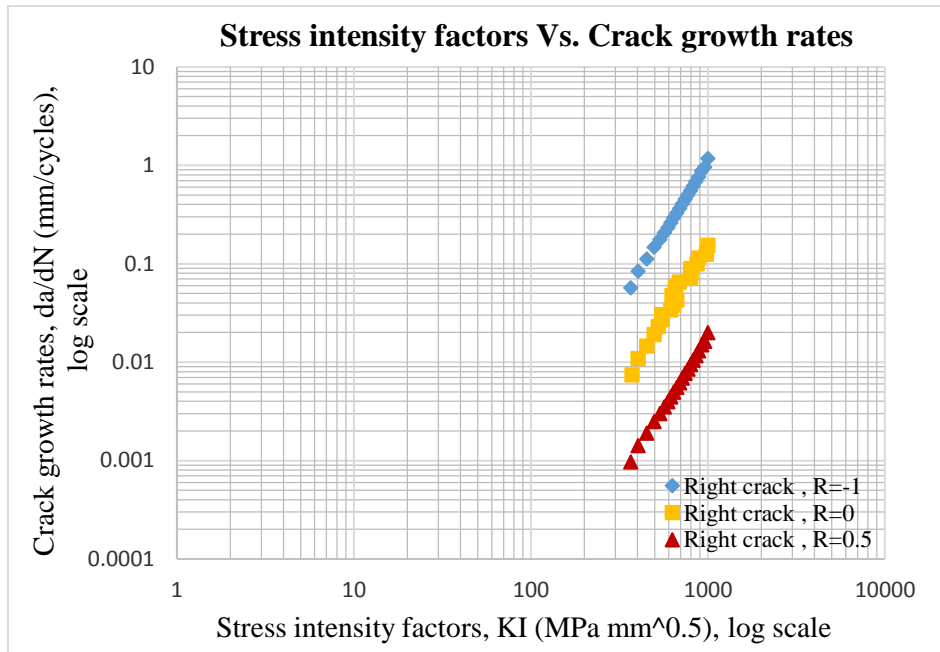


Figure 5.37 Change of stress intensity factor with crack growth rate da/dN

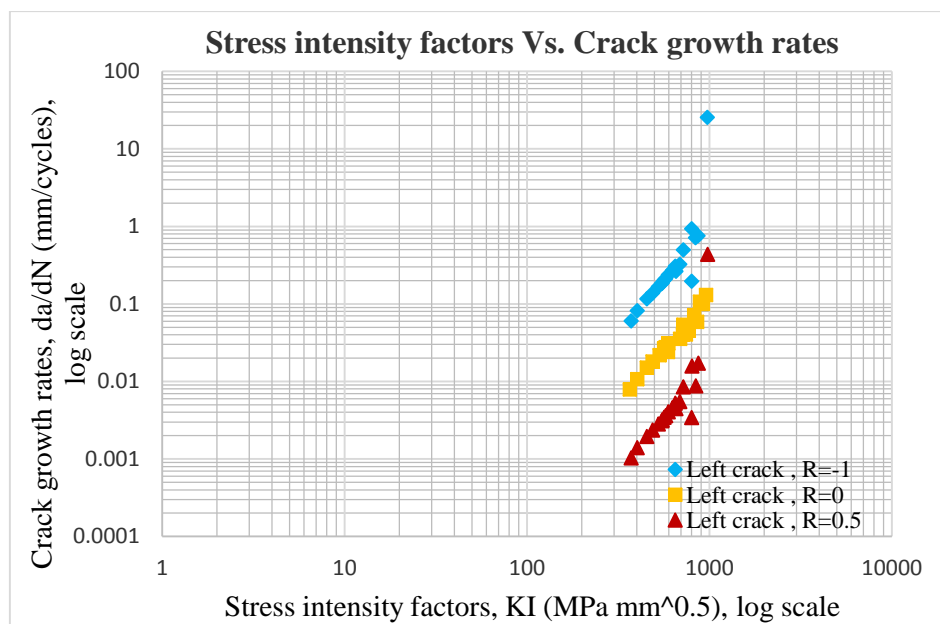


Figure 5.38 Change of stress intensity factor with crack growth rate da/dN

Results and Discussion

Double weld T plate is subjected to a tensile constant amplitude loading. Initial crack and final crack are respectively 3 and 19 mm. The final fracture criterion of crack length is adopted for the limit of crack growth.

From the fatigue crack growth test results (Table 5.7), the stress intensity factors with crack coordinates. It can be observed that the best fitting curves introduced by the stress ratio of $R = 0$ as the crack grows in regular manner. Figure 5.33, Figure 5.34 and Figure 5.35. Furthermore, the variation of crack length “a” VS number of cycle “N” is plotted in Figure 5.36 for fatigue crack growth of different R ratio (0.5,0,-1). In this figure, we show the effect of stress ratio on fatigue life N. As the stress ratio increases, the fatigue life increases.

It is understood that The FCG curves for all the examined R-ratios are shown in Figure 5.37 and Figure 5.38. As the stress ratio decreases, the fatigue crack growth rate, increases.

6 Experimental Validation of Numerical Results of friction stir welded T-joints

6.1 Introduction

In order to confirm previously presented conclusions drawn based on 3D FEM simulations performed in Abaqus, it was decided to organize experimental investigations of mechanical and metallurgical characterization of friction stir welded T-joints of similar aluminum alloys. The FSW process is concisely introduced and the interest of its application to stiffened structures of aluminum alloys explained.

It will also describe the techniques that were applied to analyze the data obtained from the experimental procedures. The experimental procedure and the results obtained are presented and discussed. This chapter is concerned only with experimental work while the modelling work was described in the previous Chapter.

The experimental work described in this chapter is included in an article submitted in 31 March 2017.

6.2 Material

The material used for this study was AA2024-T351 aluminum alloy, which has been widely used for constructions where mass is critical design parameter, like aircrafts. Mechanical properties of AA 2024-T351 as a base metal are well known, but not in the case of welded joints.

6.2.1 Chemical composition

The actual chemical composition for this material as specified in the material specification data sheet is given in Table 6.1.

Table 6.1 Chemical composition of the aluminum alloy used (%)

Material	Mg	Mn	Cu	Fe	Si	Cr	Zn	Ti	Al	Hardness	Elongation (%)
AA2024-T351	1.5	0.6	4.35	0.5	0.5	0.1	0.25	0.15	remaining	137	19

6.2.2 Metallography

Metallographic examination was carried out on the welded cross-section to obtain information about the microstructure of the material. Data for elastic-plastic tensile

properties are given in [79], in terms of true stress-strain curves, but here we have used different approach.

Namely, having in mind relatively low values of plastic strains, since AA 2024-T351 has modest capability of plastic deformation. A simple experiment has been performed with smooth tensile specimen, using ARAMIS system for measuring of strains, Figure 6.1.



Figure 6.1 The experimental setup: 1) Test machine, 2) Cameras, 3) Light source, 4) Specimen

Strains have been measured for different levels of loading, i.e. remote stress, at characteristic points in all four regions of welded joint, base metal (BM), nugget zone (NZ), heat-affected-zone (HAZ) and thermo-mechanically-affected-zone (TMAZ), Figure 6.2 [73]. Results are shown in Table 6.2, Table 6.3, and in Figure 6.3, in form of engineering stress-strain curves.

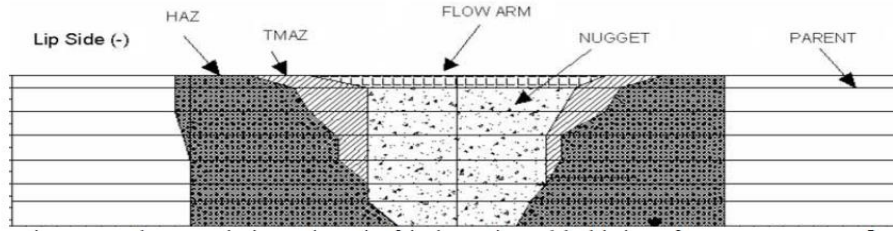


Figure 6.2 Characteristic regions in friction stir welded joint of AA 2024-T351, [83]

Table 6.2 Young's elasticity modulus (E) and Poisson's ratio (ν)

Elasticity				
FSW zones	NZ	TMAZ	HAZ	BM
Young's modulus of elasticity – E [GPa]	68	68	68	68
Poisson's ratio - ν	0.33	0.33	0.33	0.33
Yield strength – σ_Y [MPa]	320	302	398	370

Table 6.3 Stress-strain relation for different zones in welded joint

Plasticity								
σ [MPa]	NZ		HAZ		TMAZ		BM	
	ϵ	[-]	ϵ	[-]	ϵ	[-]	ϵ	[-]
20.4	0.0003		0.0003		0.0003		0.0003	
41.3	0.0006		0.0006		0.0006		0.0006	
59.6	0.0008		0.0008		0.0008		0.0009	
79	0.001		0.001		0.001		0.0011	
100.4	0.0014		0.0014		0.0015		0.0015	
136.9	0.0019		0.002		0.0021		0.0022	
186.6	0.0023		0.0025		0.0028		0.0028	
231.9	0.0035		0.0038		0.0048		0.0046	
323.4	0.0056		0.0086		0.0158		0.0104	
415.7	0.0198		0.0228		0.0398		0.032	

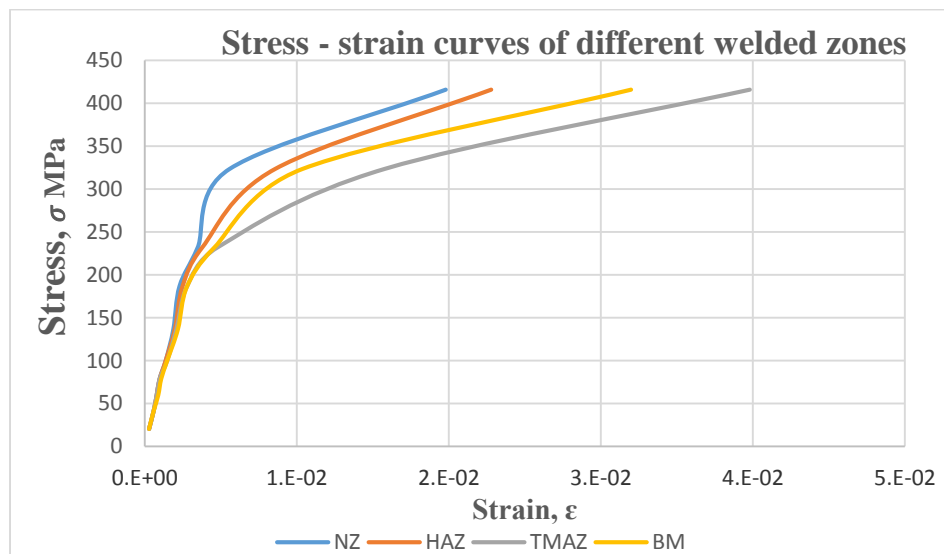


Figure 6.3 Stress–strain curves for different regions in welded joint

The constant Paris law (C and m) are taken from [72, 73], having the same value for all zones, $C=2.02345 \cdot 10^{-10}$ cycles⁻¹, $m=2.94$.

6.3 Specimen preparation and Tests description

Samples were obtained by sectioning friction stir welded plates in the direction of the weld line. The samples were cut and polished for metallographic examination. For this purpose, three samples of friction stir welded T-joints were analyzed. Both skin and reinforcement of these T-joints are made of AA2024 with T3 heat treatment (solution heat-treated and naturally aged) for all samples [75].

Three friction stir welded T joint samples of the AA2024-T351 were analyzed for comparative purposes. The thickness of the welded plates and the reinforcement are equal to the thickness of the skin in the T-joints samples (5 mm).

Mechanical tests were carried out for base material AA2024-T351. Macrostructures and microstructures of all friction stir welded samples were obtained and analyzed with the aim of detecting cracks, porosities and other defects, and also observing the metallurgical characteristics of the different zones of the weld [76].

6.4 Experimental investigation of fatigue crack growth

The geometry of the welded T-joints samples is presented in Figure 6.4 and Figure 6.5. A total of 9 specimens were used in the bending tests: Three specimens machined from each AA2024-T351 T-joint.

All crack propagation tests were performed in accordance with the standard test methods for measurement of fatigue crack growth rates described in ASTM E 399 with the specific, 3PB-like specimen Figure 6.5, using high-frequency pulsator Figure 6.6, in force control. The tests were carried out at constant load amplitude, constant frequency of 15 HZ and constant stress ratio of $R = 0$. The T joint specimens were pre-cracked to an initial crack length of 2.5 mm. Maximum applied stress was 10 MPa. The specimen was designed so that the stringer effect can be investigated [78].

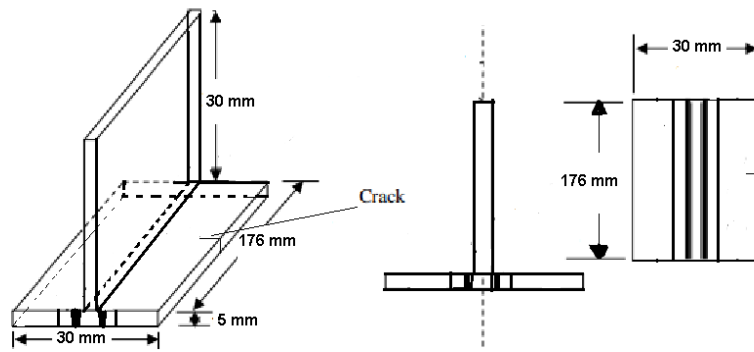


Figure 6.4 Configuration of the T-joints

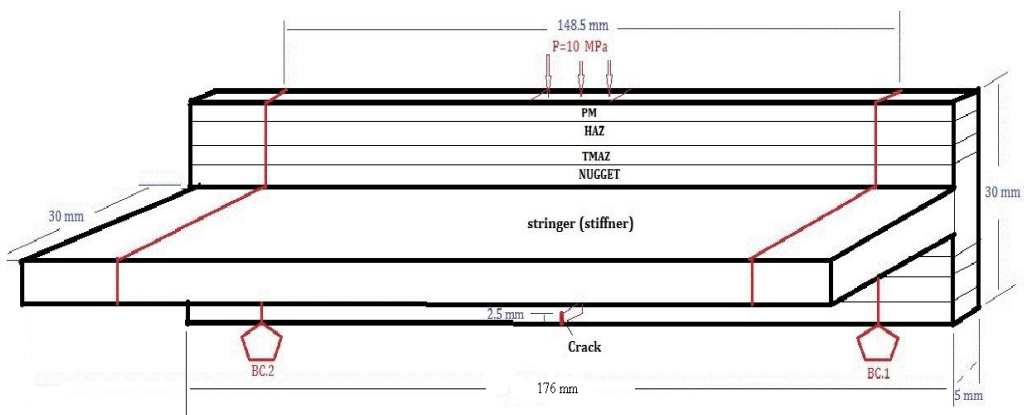


Figure 6.5 Three Point Bending specimen made of T Joint



Figure 6.6 Fatigue crack growth equipment

Special foils were used to measure crack length, Figure 6.7. As the crack grows and its tip is moving, the foil breaks and changes its resistance linearly with crack length changes, as schematically shown in Figure 6.7.

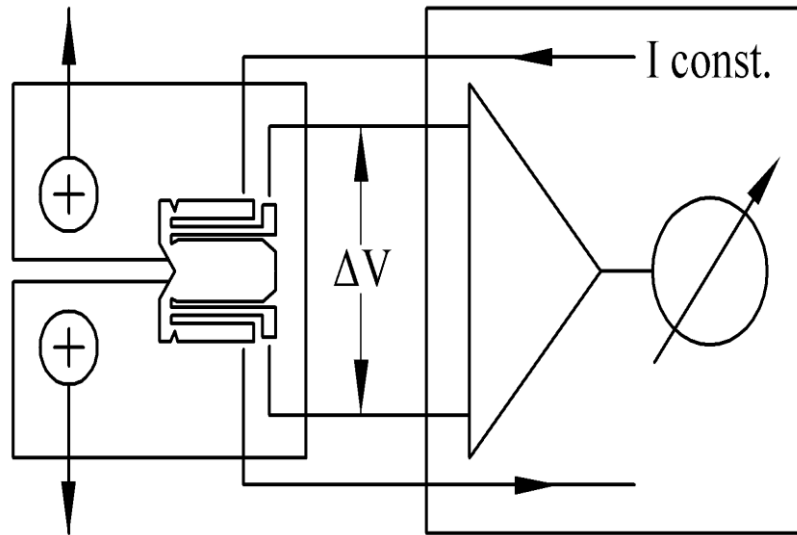


Figure 6.7 Scheme of measuring foil for fatigue crack growth monitoring

The experiment was performed the initial crack length 2.5 mm up to crack length 8.5 mm, with the basic idea to compare the results with numerical simulation. The results for crack length vs. number of cycles are given in Table 6.4 and in Figure 6.10, together with numerical results.

6.5 Finite Element Model (FEM) and Analysis

6.5.1 Material model

An elastic-plastic material model with isotropic hardening model was employed for FEA. This model is a reasonable assumption for remote tension loading and is characterized by a uniform expansion (hardening) in the size of the yield surface (yield stress) in all principal directions in the stress space, as plastic straining occurs.

6.5.2 FEA software

All simulations and analyses were conducted on ABAQUS 6.11, which is a general purpose of finite element program [77]. A 3-D FEM model (figure 1) of a T-welded joint

in an aluminum alloy 2024-T351 specimen of dimensions (176x30x5) for both skin and stiffener has been created using authors' written Abaqus code. For this purpose, three-dimensional homogeneous isotropic model is used to study the mechanical properties of the welded structure. Extended Finite Element Method (xFEM) including ABAQUS and Morfeo software are used to demonstrate the results of the growth of cracks in FSW 2024-T351 welded joints. Three-point bending fatigue load stress is applied in the center of the plate opposite to the initial crack. The material properties in all welded regions of the joint are adopted from available experiments, as well as the fatigue crack growth.

The main objective of this work is to study stringer effect on fatigue crack growth in T joints made by FSW of AA 2024-T351, by using extended finite element method (xFEM), as already used in the case of butt joints, [74,75], and also for T joint [76,77].

The extended finite element method was developed to ease difficulties in solving problems with localized features that are not efficiently resolved by mesh refinement, [78-80]. A key advantage of xFEM is that in such problems the finite element mesh does not need to be updated to track the crack path. Morfeo/Crack for Abaqus relies on the implementation of the

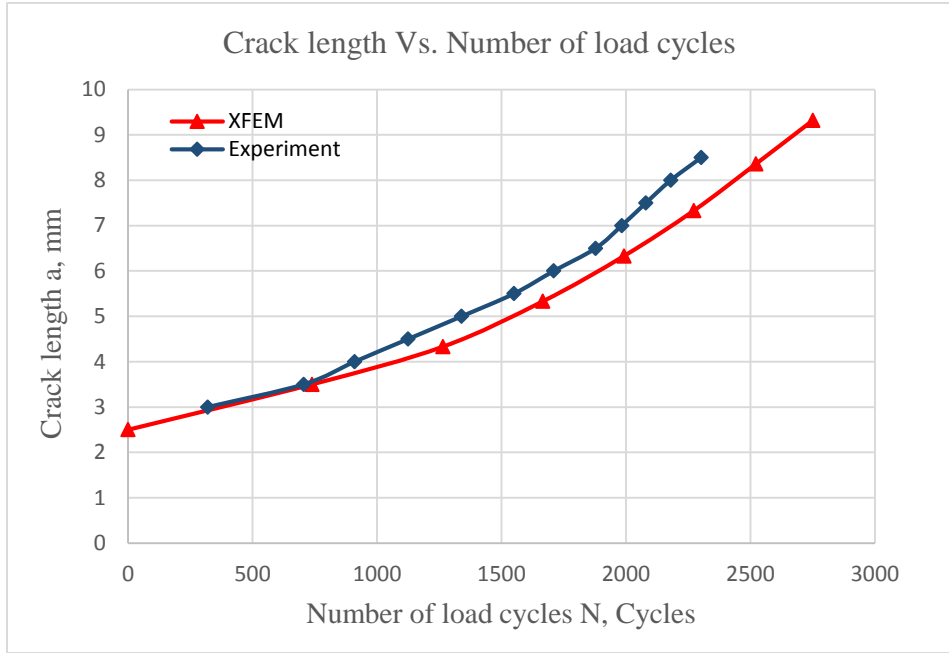
xFEM method available in Abaqus. Morfeo/Crack for Abaqus is capable of performing crack propagation simulations in complex geometries. It calls Abaqus at each propagation step and between each step, then reads the Abaqus solution, recovers a richer, improved xFEM solution in a small area surrounding the crack and computes the SIFs. This procedure has been recently applied to verify the results of 3D simulation with the experiments carried out on the standard Charpy specimen. From the point of view, the material behavior and the xFEM simulation require basic mechanical properties (tensile), in both elasticity and plasticity, as well as material parameters defining fatigue crack growth rate, e.g. C and n in Paris Law. For the base metal all of them are well known, but there are very few data about weldments, i.e. material properties of different regions in welded joint, e.g. [82,83]. It is very complicated to measure these properties in such a small regions, as HAZ and THAZ are, so another approach will be used here, as described in [84]. Results from the analysis were post-processed using the ABAQUS Viewer.

6.5.3 Numerical model

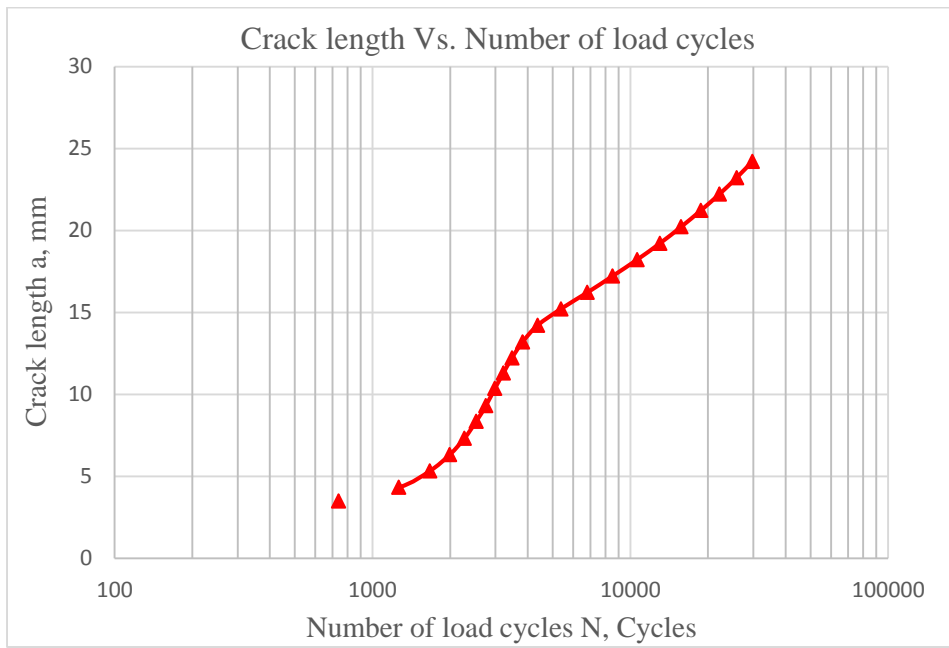
There are 6 main steps of creating a model in ABAQUS

Table 6.4 X-FEM and Experimental data

Number of steps	XFEM				Experiment		
	Crack length, mm	Stress intensity factor, KI MPa√mm	Number of cycles	Crack growth rate, da/dN (mm/cycle)	Crack length (a),mm	Number of Cycles (N), cycles	Crack growth rate,da/dN
1	2.5	197.939	0	0.00114	3	320	0.0015625
2	3.5	224.59	738.813	0.00165	3.5	705	0.001298701
3	4.33	248.385	1264.666	0.00222	4	910	0.002439024
4	5.33	269.158	1666.107	0.00282	4.5	1125	0.002325581
5	6.33	285.361	1992.416	0.00334	5	1340	0.002325581
6	7.33	297.894	2273.044	0.0038	5.5	1550	0.002380952
7	8.36	308.751	2522.826	0.00422	6	1710	0.003125
8	9.32	316.098	2751.53	0.00452	6.5	1878	0.00297619
9	10.36	309.444	2979.453	0.00425	7	1983	0.004761905
10	11.31	308.735	3215.339	0.00422	7.5	2080	0.005154639
11	12.23	292.802	3471.953	0.00361	8	2180	0.005
12	13.2	255.786	3815.994	0.00242	8.5	2302	0.004098361
13	14.22	213.736	4370.564	0.00143			
14	15.22	172.141	5378.604	0.00075			
15	16.22	162.915	6812.964	0.00064			
16	17.22	152.244	8534.034	0.00052			
17	18.22	142.865	10620.384	0.00043			
18	19.22	137.803	13028.754	0.00039			
19	20.22	132.325	15725.294	0.00034			
20	21.22	127.051	18763.884	0.00031			
21	22.22	122.602	22161.864	0.00027			
22	23.22	120.355	25837.704	0.00026			
23	24.22	117.023	29775.884	0.00024			
24	25.22	113.935	34044.134	0.00022			
25	26.22	111.259	38640.554	0.00021			



a)



b)

Figure 6.10 Crack propagation vs. cycle number – N , a) comparison between experimental and numerical data

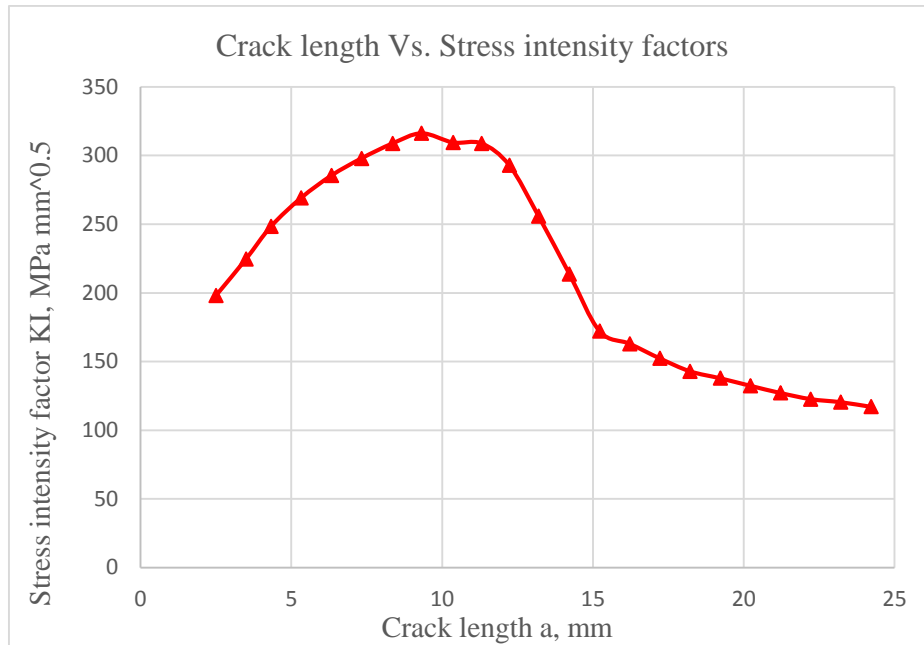


Figure 6.11 Change of stress intensity factor vs. crack length

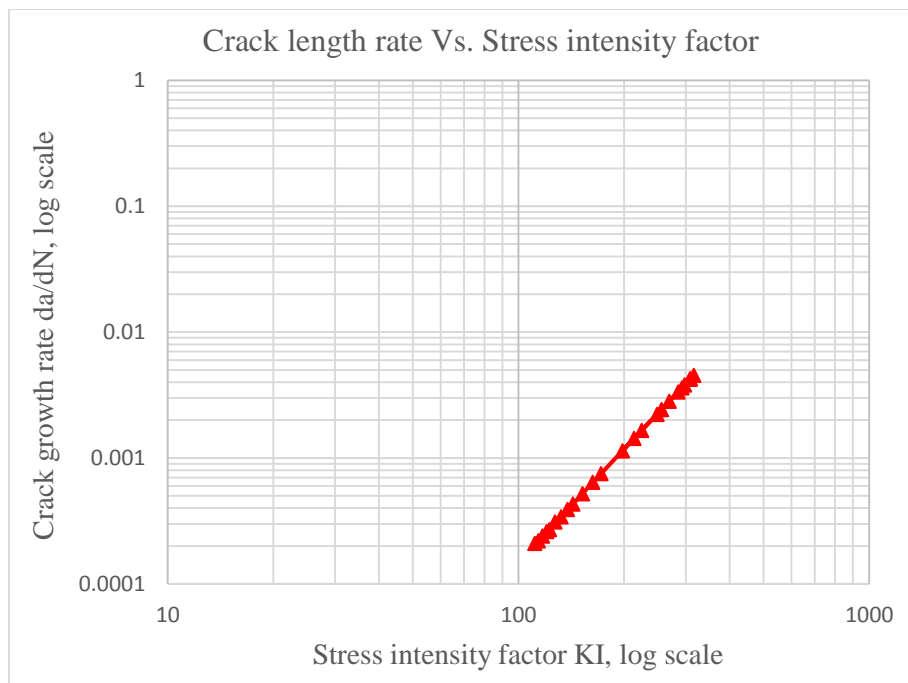


Figure 6.12 Change of crack growth rate and stress intensity factor

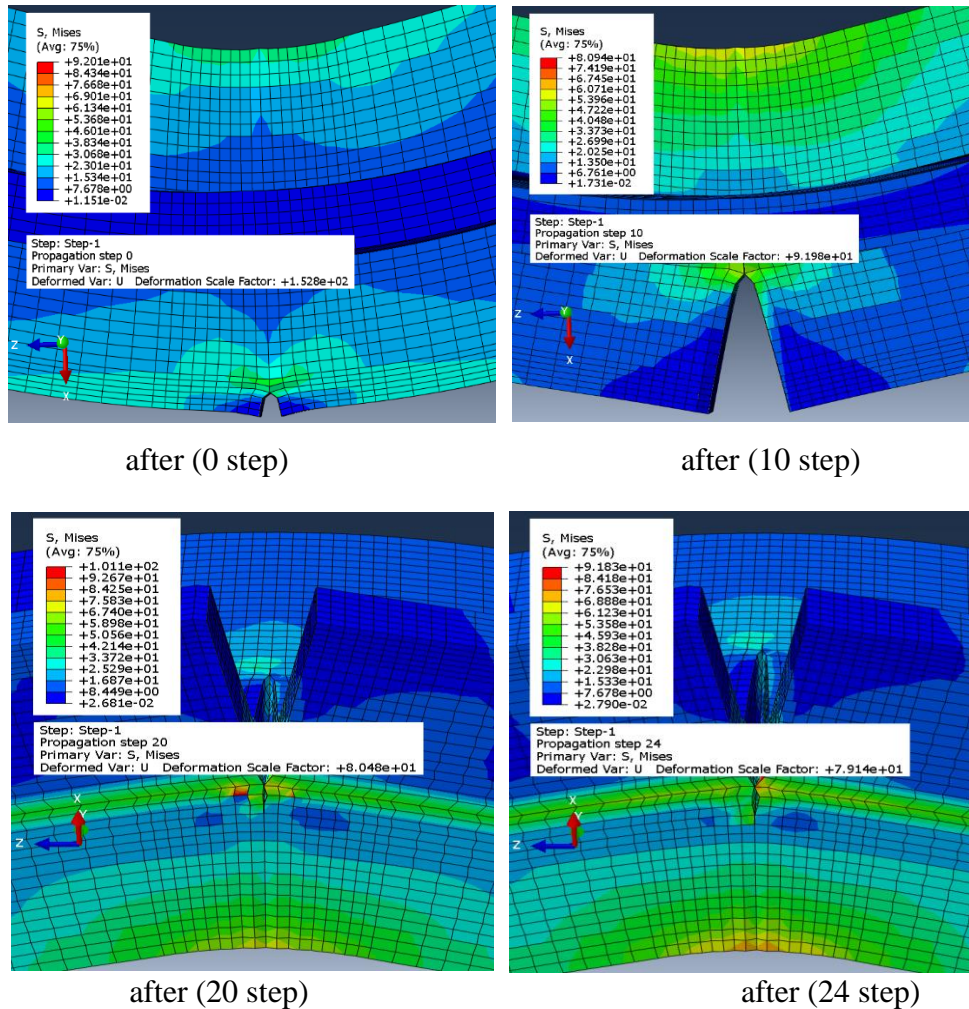


Figure 6.13 Crack length and Von Mises stress for different crack growth steps (0, 10, 20, 25)

6.6 Experimental & Numerical results and discussion

In this section, resulted data of experimental and numerical simulation using ABAQUS/Morfeo software are given in Table 4, in the form of the stress intensity factor, number of cycles and crack growth rate vs. crack length, for 25 crack growth steps (each increment approximately 1 mm). Crack length as a function of load cycles N is also given in Figure 6.10, whereas stress intensity factor vs. crack length is given in Figure 6.11. In addition, Figure 6.12 describes the change of crack growth rate with the increase of stress intensity factor

Comparison between experimental and numerical results is shown in Figure 6.10a, indicating good agreement, as well as the conservative prediction of numerical simulation, but just up to 8.5 mm. Figure 6.10b presents only numerical results, indicating

significant decrease of crack growth rate once crack tip reached the stringer and consequent slower growth rate through stringer.

From Figure 6.11 it is clearly seen that from step 1 till step 8 the stress intensity factor increases until step 9 is reached, when it starts to decrease because of the stiffener (stringer) effect. The same holds for the crack growth rate, leading to an increase of the structural life of T welded joint due to stringer effect. Finally, crack growth and von Mises stress distribution are shown in Figure 6.13 for different steps, i.e. at the beginning (0 step) and after 10, 20 and 25 steps. One can see that crack growth changes direction from the base plate to the stringer after 10th step, or, more precisely in 12th step, as seen from Table 6.4.

Concluding remarks

Based on the presented results, one can conclude that numerical simulation can be used to predict number of cycles during crack growth in a complex structure such as welded T joint. It has been proved by good agreement of numerical and experimental results up to crack length of 8.5 mm.

Strong effect of stringer has been demonstrated, reducing stress intensity factor and contributing significantly to reliable and longer service life of welded joints made of AA2024-T351 [8].

The performance of the FEA model was assessed by comparing its predictions with experimental measurements. The most likely failure mechanisms of joints with various geometric characteristics were identified [85].

7 Conclusions and Recommendations

The conducted research in this doctoral dissertation aims to solve problems of estimating the integrity in T welded structures of aluminum alloy, as well as fatigue crack growth phenomena. The work was analyzed in the following examples, based on which there were relevant conclusions:

The first case is both butt and T welded plate loaded in three - point bending with an edge crack were simulated and the effect of the stiffener when comparing the structural lives is clearly seen.

It can be noticed that the stiffener (stringer) indicates redistribute load, and increases of the structural life of the material welded structure, at the same time stress intensity factors decrease when the crack reaches the stringer compared to unstiffened welded structure. Faster crack growth occurs after load cycles number of 13000. During the propagation of the crack through the structure, change of its direction can be clearly seen after the crack propagation reaches the stringer; it grows vertically within the stringer and horizontally within the base material. This is related to shear stresses within the structure

The second case is the effect of one and two stiffeners was reported. Three different welded plates (butt joint, T welded joint and double T welded joint) is subjected to tensile loading and crack located in TMAZ. It has been experimentally established that TMAZ is the place where cracks occur most often. Crack length as a function of load cycles N is also obtained. It was decided to count the number of cycles from initial crack, until reaches the specific values and compare this value with the number of cycles in all three different welded joint. For butt-welded joint, faster crack growth, occurs after load cycles number of 400 and total number of cycle to reach a value of crack length 18mm is 520 cycles, as shown in the change of the curve slope.

For one stiffener T welded joint, faster crack growth occurs after load cycles number of 550 and total number of cycle to reach a crack length value of 18mm is 588 cycles.

For two stiffeners T welded joint, faster crack growth occurs after load cycles number of 650 and total number of cycle to reach a crack length value of 18mm is 615 cycles.

Finally, the stiffeners (stringers) indicate redistribute load, and increasing of the structural life of the material welded structure, at the same time stress intensity factors decrease when the crack reaches the stringer compared to unreinforced welded structure.

Effect of different stress ratios (0.5, 0 and -1) is also studied and different results are obtained.

As the stress ratio increases, the fatigue life increases.

For studying crack growth of different stress ratios, we conclude that when the stress ratio decreases, the fatigue crack growth rate increases.

The third case is T welded plate loaded in three - point bending with an edge crack by comparing the experimental results with the numerical results obtained. Fatigue life of the loaded specimen was indicating good agreement between experimental and numerical data values, as well as the conservative prediction of numerical simulation, but just up to 8.5 mm. The numerical results, indicating significant decrease of crack growth rate once crack tip reached the stringer and consequent slower growth rate through stringer.

By examining a large number of different 3D models, it was found that the stringers of modeled panels have an impact on the distribution of the stress intensity factor near the crack tip, i.e. on its own growth. The way in which the boundary conditions are defined (connection with the rest of construction, assembly), as well as the method of introducing load into the structure has a significant impact on obtaining quality solutions of numerical calculations. Also, define the type and size of the final element mesh on the 3D model of plate is important for the accuracy of the calculation. Therefore, the mesh around the crack tip needs to be refinement, also in all area of its expected growth.

The main results and conclusions of the work presented in the dissertation are as follows: Based on the presented results, one can conclude that numerical simulation can be used to predict number of cycles during crack growth in a complex structure such as welded T joint. It has been proved by good agreement of numerical and experimental results up to crack length of 8.5 mm.

Strong effect of stringer has been demonstrated, reducing stress intensity factor and contributing significantly to reliable and longer service life of welded joints made of AA 2024-T351.

The crack propagates in different directions (base material and stringer) because of shearing stresses in the structure and redistribution of stress intensity factors.

This work has shown that the benefits of using software in the integrity assessment of the structure are reflected in the following: saving time and money, which are important from an economic point of view. So, software user, in the framework of which, replaces

expensive Laboratory measurements: modeling the structure, introducing the initial crack in the structure, and then calculating the stress intensity and the deformation, as well as crack propagation simulation with all relevant parameters of fracture mechanics.

Guidance for further research investigations in order to study more closely the phenomenon of initial crack growth in stiffened structures including T welded joint plates obtained by friction stir welding are:

Examining different forms and locations of cracks with different positions in the welded structure,

Studying fatigue crack growth in stiffened curved welded plate,

Analysis the growth of multi cracks,

Analysis of residual stresses impact in the welded areas.

References

- [1] R.S. Mishra and Z.Y. Ma, *Mater. Sci. Eng. R* 50 (2005) 1-78.
- [2] Y. Li, L.E. Murr, J.C. McClure, *Mater. Sci. Eng. A* 271 (1999) 213.
- [3] A.L. Biro, B.F. Chenelle and D.A. Lados, *Metall. Mater. Trans. B*, 43A, 2012, pp. 1622-1637.
- [4] M. Ericsson and R. Sandstrom, *Inter. Jour. Fatig.* 25 (2003) 1379-1387.
- [5] S. Suresh, *Fatigue of Materials*, 2nd edition, Cambridge University Press, 1998.
- [6] G. Biallas, R. Braun, C.D. Donne, G. Staniek, W.A. Kaysser, in: *Proceedings of the First International Symposium on Friction Stir Welding*, Thousand Oaks, CA, USA, June 14–16, 1999.
- [7] P.S. Pao, E. Lee, C.R. Feng, H.N. Jones, D.W. Moon, in: K.V. Jata, M.W. Mahoney, R.S. Mishra, S.L. Semiatin, T. Lienert (Eds.), *Friction Stir Welding and Processing II*, TMS, Warrendale, PA, USA, 2003, p. 113.
- [8] H. Hori, S. Makita, H. Hino, in: *Proceedings of the First International Symposium on Friction Stir Welding*, Thousand Oaks, CA, USA, June 14–16, 1999.
- [9] M. Kumagai, S. Tanaka, in: *Proceedings of the First International Symposium on Friction Stir Welding*, Thousand Oaks, CA, USA, June 14–16, 1999.
- [10] G. Bussu, P.E. Irving, in: *Proceedings of the First International Symposium on Friction Stir Welding*, Thousand Oaks, CA, USA, June 14–16, 1999.
- [11] J.Z. Zhang, R. Pedwell, H. Davies, in: *Proceedings of the Second International Symposium on Friction Stir Welding*, Gothenburg, Sweden, June 2000.
- [12] M. Erisson, R. Sandstrom, J. Hagstrom, in: *Proceedings of the Second International Symposium on Friction Stir Welding*, Gothenburg, Sweden, June 2000.
- [13] N. Jayaraman, P. Prevey, M. Mahoney, in: K.V. Jata, M.W. Mahoney, R.S. Mishra, S.L. Semiatin, T. Lienert (Eds.), *Friction Stir Welding and Processing II*, TMS, 2003, p. 259.
- [14] K.V. Jata, K.K. Sankaran, J.J. Ruschau, *Metall. Mater. Trans. A* 31 (2000) 2181.

-
- [15] C.D. Donne, G. Biallas, T. Ghidini, G. Raimbeaux, in: Proceedings of the Second International Symposium on Friction Stir Welding, Gothenburg, Sweden, June 26–28, 2000.
- [16] P.S. Pao, S.J. Gill, C.R. Feng, K.K. Sankaran, *Scripta Mater.* 45 (2001) 605.
- [17] G. Bussu and P.E. Irving, *Int. J. Fatigue* 25 (2003) 77.
- [18] S. Kim, C.G. Lee and S.J. Kim, *Mat. Sci. Eng. A.* 478 (2008) 56-64.
- [19] C. Zhou, X. Yang and G. Luan, *J. Mater. Sci.* 41 (2006) 2771-2777.
- [20] A. Steuwer et al., *Materials Science and Engineering A* 441 (2006) 187–196].
- [21] H. R. Shercliff and P. A. Colegrove: in 'Friction stir welding and processing', (ed. R. S. Mishra et al.), 187-217; 2007, Materials Park, OH, ASM International.
- [22] V. I. Vill': 'Friction welding of metals'; 1959, Mashgiz, Leningrad.
- [23] R. E. Andrews and K. A. Beamish: 'Characterisation of and guidelines for rotary friction welding of common metallic engineering materials', TWI members report no. 824, TWI, Abington, UK, 2005.
- [24] Y. G. Kim, H. Fujii, T. Tsumura, T. Komazaki and K. Nakata: *Mater. Sci. Eng. A*, 2006, **A415**, 250-254.
- [25] P. L. Threadgill and A. J. Leonard: 'Macro and microstructural features of friction stir welds in various materials', TWI members report no. 693/1999, TWI, Abington, UK, 1999
- [26] M. M. Z. Ahmed, B. P. Wynne, W. M. Rainforth and P. L. Threadgill: *Scr. Mater.*, 2008, **59**, 507-510
- [27] S. J. Barnes, A. Steuwer, S. Mahawish, R. Johnson and P. J. Withers: *Mater. Sci. Eng. A*, 2008, **A492**, 35-44
- [28] P. L. Threadgill and M. E. Nunn: 'A review of friction stir welding: part 1 process overview ', TWI members report no. 760/2003, TWI, Abington, UK, 2003.
- [29] Mishra, R.S., Ma, Z.Y., 2005. Friction stir welding and processing. *Materials Science and Engineering R: Reports*, 50(1-2), 1-78P
- [30] Mendez, P.F., Eagar, T.W., 2001. Welding processes for aeronautics. *Advanced Materials and Processes*, 159(5), 39-43.
- [31] Kwon, Y.J., Shigematsu, I., Saito, N., 2008. Dissimilar friction stir welding between magnesium and aluminum alloys. *Materials Letters*, 62(23), 3827-3829.

-
- [32] Colegrove, P.A., Shercliff, H.R. (2003), Experimental and Numerical analysis of Aluminium alloy 7075- T7351 friction stir welds, *Science and Technology of welding and Joining*, Vol. 8(5),pp. 360-368.
- [33] Sato, Y.S, Kokawa, H., Enmoto, M., Jogan, S. (1999), Microstructural Evolution of 6063 Aluminum during Friction Stir Welding, *Metallurgical and Materials Transactions A*, Vol.30 A, pp. 2429-2437
- [34] Donne, E. Lima, J. Wegener, A. Pyzalla, T. Buslaps, in: *Proceedings of the Third International Symposium on Friction Stir Welding*, Kobe, Japan, September 27– 28, 2001.
- [35] O. R. Myhr and O. Grong, "Process modelling applied to 6082-T6 aluminium weldments--II. Applications of model," *Acta Metallurgica et Materialia*, vol. 39, pp.2703-2708, 1991.
- [36] H. Jin, S. Saimoto, M. Ball, and P. L. Threadgill, "Characterisation of microstructure and texture in friction stir welded joints of 5754 and 5182 aluminium alloy sheets," *Materials Science and Technology*, vol. 17, pp. 1605-1614, 2001.
- [37] T. Hirata, T. Oguri, H. Hagino, T. Tanaka, S. W. Chung, Y. Takigawa, and K.Higashi, "Influence of friction stir welding parameters on grain size and formability in 5083 aluminum alloy," *Materials Science and Engineering: A*, vol. In Press, Corrected Proof, 2007.
- [38] Y. S. Sato, Y. Sugiura, Y. Shoji, S. H. C. Park, H. Kokawa, and K. Ikeda, "Post-weld formability of friction stir welded Al alloy 5052," *Materials Science and Engineering A*, vol. 369, pp. 138-143, 2004.
- [39] M. A. Sutton, B. Yang, A. P. Reynolds, and R. Taylor, "Microstructural studies of friction stir welds in 2024-T3 aluminum," *Materials Science and Engineering A*, vol.323, pp. 160-166, 2002.
- [40] M. A. Sutton, B. Yang, A. P. Reynolds, and J. Yan, "Banded microstructure in 2024-T351 and 2524-T351 aluminum friction stir welds. Part II. Mechanical characterization," *Materials Science and Engineering A*, vol. 364, pp. 66-74, 2004.
- [41] B. Yang, J. Yan, M. A. Sutton, and A. P. Reynolds, "Banded microstructure in AA2024-T351 and AA2524-T351 aluminum friction stir welds. Part I. Metallurgical studies," *Materials Science and Engineering A*, vol. 364, pp. 55-65, 2004.

-
- [42] C.E. Inglis, "Stresses in a plate due to the presence of cracks and sharp corners," *Trans. Inst. Nav. Archit. London* 55, 1913, pp. 219–230.
- [43] A.A. Griffith, "Phenomena of rupture and flow in solids," *Philos. Trans. R. Soc London Ser. A221*, 1920, pp. 163–198.
- [44] G.R. Irwin, "Analysis of stresses and strains near the end of a crack traversing in a plate," *J. Appl. Mech.* 24, 1957, pp. 361–364.
- [45] E. Orowan, "Energy criteria of fracture," *Weld. J.* 34, 1955, pp. 157–160.
- [46] James M. N. (1998). *Engineering Materialism and Structural Integrity*. *Journal of Engineering Design*. Vol. 9 No. 4, published by Carfax Publishing Ltd., pp.329-342.
- [47] Anderson, T.L. (1995). *Fracture Mechanics, Fundamentals and Applications*. 2nd Edition, CRC Press.
- [48] Rice J.R. (1968). A Path Independent Integral and the Approximate Analysis of Strain Concentration by Notches and Cracks. *Journal of Applied Mechanics*, Vol. 35, 379-386.
- [49] Radaj D (1996) Review of fatigue strength assessment of nonwelded and welded structures based on local parameters. *International Journal of Fatigue* 18(3):153–170
- [50] Fricke W (2003) Fatigue Analysis of Welded Joints: State of Development. *Marine Structures* 16(3):185–200
- [51] Kaplan MP, Wolff TA, Willis I (1996) Life extension and damage tolerance of aircraft. *ASM HandBook Volume 19 Fatigue and Fracture*. ASM International, USA, 557–564
- [52] Stephen R, Fatemi A, Stephen R, Fuchs H (2001) *Metal fatigue in engineering*. John Wiley & Sons, West Sussex, UK 1–465
- [53] Maddox S (2003) Review of fatigue assessment procedures for welded aluminum structures. *International Journal of Fatigue* 25(12):1359–1378
- [54] Zhou C, Yang X, Luan G (2006) Effect of oxide array on the fatigue property of friction stir welds. *Scripta Materialia* 54(8):1515–1520
- [55] Lomolino S, Tovo R, Dossantos J (2005) on the fatigue behaviour and design curves of friction stir butt-welded Al alloys. *International Journal of Fatigue* 27(3):305–316

-
- [56] Janssen M, Zuidema J, Wanhill RJH. Fracture Mechanics. 2. VSSD; 2002
- [57] Rooke, D.P. and Cartwright, D.J., Stress Intensity Factors. Her Majesty's Stationary Office, London (1976).
- [58] Murakami, Y. (ed.), Stress Intensity Factors Handbook. Pergamon Press, Oxford, 1987
- [59] Kahl A, Fricke W, Bollero A, Chirica I, Garbatov Y, Jancart F, Remes H, Rizzo CM, Von Selle H, Urban A, Wei L. Round Robin study on structural hot-spot and effective notch stress analysis. MARSTRUCT International Conference on Advancements in Marine Structures; 2007 Mar 12–14; Glasgow, UK. ISBN-10: 0415437253.
- [60] Dolbow, J. [1999]. An extended finite element method with discontinuous enrichment for applied mechanics. Ph. D. thesis, Northwestern University.
- [61] Sukumar, N., N. Moes, B. Moran, and T. Belytschko [2000]. Extended finite element method for three-dimensional crack modelling. International journal for numerical methods in engineering 48, 1549–1570.
- [62] [Karihaloo and Xiao 2003] B. L. Karihaloo and Q. Z. Xiao, “Modelling of stationary and growing cracks in FE framework without remeshing: a state-of-the-art review”, Comput. Struct. 81:3 (2003), 119–129.
- [63] Janssen, M., Zuidema, R.J.H. and Wanhill, J. Fracture Mechanics. New York. Spon Press Taylor & Francis, 2004.
- [64] Abass, H. H., Hedayati, S. and Meadows D. L. 1996. “Nonplanar Fracture Propagation from a Horizontal Wellbore : Experimental Study.” SPE Paper 24823.
- [65] Burlayenko, V. N. and Sadowski, T. 2008. “FE Modeling of Delamination Growth in Interlaminar Fracture Specimens.” Budownictwo I Architektura 2: 95–109.
- [66] Song, J.H., Areias, P. and Belytsckho, T. 2006. “A Method for Dynamic Crack and Shear Band Propagation with Phantom Nodes” International Journal for Numerical Methods in Engineering 67: 868–893.
- [67] Dassault Systemes. “Abaqus 6.9 Overview.” Last Modified 2009.
<http://abaqusdoc.ucalgary.ca/v6.9/books/rnb/default.htm>.

-
- [68] Benzeggagh, M. L., and Kenane, M. 1996. "Measurement of Mixed-Mode Delamination Fracture Toughness of Unidirectional Glass/Epoxy Composites with Mixed-Mode Bending Apparatus." *Composites Science and Technology* 56 (4): 439–449.
- [69] Elisa, P. 2011. "Virtual Crack Closure Technique and Finite Element Method for Predicting the Delamination Growth Initiation in Composite Structures" in *Advances in Composite Materials-Analysis of Natural and Man-Made Materials*, Edited by Dr. Pavla Tesinova.
- [70] Reeder, J. R. and Crews, J.H. 1990. "Mixed-Mode Bending Method for Delamination Testing." *AIAA Journal* 28 (7): 1270–1276
- [71] E. Rybicki and M. Kanninen, "A Finite Element Calculation of Stress Intensity Factors by a Modified Crack Closure Integral," *Engineering Fracture Mechanics*, vol. 9, no. 4, pp. 931–938, 1977.
- [72] Mishra, R.S., Ma, Z.Y., Friction stir welding and processing, *Materials Science and Engng. R* 50 (2005), pp.1-78.
- [73] A. Živković, A. Đurđević, A. Sedmak, S. Tadić, I. Jovanović, Đ. Đurđević, K. Zammit, Friction StirWelding of Aluminium Alloys – T Joints, *Structural Integrity and Life*, Vol. 15, No. 3, 2015, p. 181–186
- [74] E. Rakipovski, A. Grbović, G. Kastratović, N. Vidanović, Application of Extended Finite Element Method for Fatigue Life Predictions of Multiple Site Damage in Aircraft Structure, *Structural Integrity and Life* Vol. 15, No. 1, 2015, p. 3–6
- [75] D. Živojinović, A. Sedmak, A. Grbović, Crack Growth Analysis in Friction Stir Welded Joint Zones Using Extended Finite Element Method, *Structural Integrity and Life* Vol. 13, No. 3, 2013, p. 179–188
- [76] A. Kraedegh, W. Li, A. Sedmak, A. Grbović, N. Trišović, R. Mitrović, S. Kirin, Numerical Simulation of Fatigue Crack Growth in A2024-T351 T Welded Joint *Structural Integrity and Life* Vol. 17, No. 1, 2017, p. 3-6
- [77] M. Saeed Sghayer, A. Grbović, A. Sedmak, M. Dinulović, E. Doncheva, B. Petrovski, Fatigue Life Analysis of the Integral Skin-Stringer Panel Using XFEM *Structural Integrity and Life* Vol. 17, No. 1, 2017, p. 7-10

-
- [78] Belytschko T., Black T., 1999. Elastic crack growth in finite elements with minimal remeshing. *International Journal of Numerical Methods in Engineering* 45, 601–620.
- [79] Stolarska M., Chopp D. L., Moës, N., Belytschko T., Modelling crack growth by level sets in the extended finite element method, *International Journal for Numerical Methods in Engineering*, Vol. 51, No. 8, (2001), pp. 943-960.
- [80] N. Moës, A. Gravouil, and T. Belytschko. Non-planar 3D crack growth by the extended finite element and level sets — Part I: Mechanical model. *International Journal for Numerical Methods in Engineering*, 53:2549–2568, 2002.
- [81] Lj. Lazić Vulićević, A. Grbović, A. Sedmak , A. Rajić, The extended finite element method in fatigue life predictions of oil well welded pipes made of API J55 steel, *Frattura ed Integrità Strutturale*, 36 (2016) 46-54; DOI: 10.3221/IGF-ESIS.36.05
- [82] Golestaneh, A. F., Ali, A., Voon , W. S., Faizal, M., & Mohammadi, M. Z. (2009). Simulation of fatigue crack growth in friction stir welded joints in 2024-T351 Al alloy. *Suranaree Journal of Science and Technology*, 16, p. 35-46.
- [83] Golestaneh, A.F., Ali, A., Zadeh, M., Modelling the fatigue crack growth in friction stir welded joint of 2024-T351 Al alloy, *Materials and Design*, 30 (2009), p. 2928-2937.
- [84] B.S. Younise, A. Sedmak, Micromechanical Study of Ductile Fracture Initiation and Propagation on Welded Tensile Specimen with a Surface Pre-Crack in Weld Metal, *Structural Integrity and Life* Vol. 14, No. 3, 2014, p. 185–191
- [85] I. Camagic, Investigation of service condition effects on structural and life assessment of pressure vessels for high temperates (in Serbian), Faculty of Technical Sciences, University of Pristina with the seat in Kosovska Mitrovica, Serbia

Прилог 1.

Изјава о ауторству

Потписани-а Абубакар М.А. Кредег

број индекса Д48/13 _____

Изјављујем

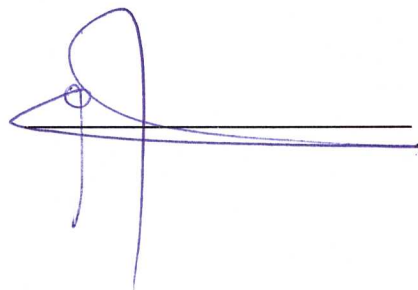
да је докторска дисертација под насловом

„РАСТ ЗАМОРНЕ ПРСЛИНЕ У Т ЗАВАРЕНОМ СПОЈЕВИМА ОД
АЛУМИНИЈУМСКЕ ЛЕГУРЕ - FATIGUE CRACK GROWTH IN T WELDED
JOINTS OF ALUMINUM ALLOY“

- резултат сопственог истраживачког рада,
- да предложена дисертација у целини ни у деловима није била предложена за добијање било које дипломе према студијским програмима других високошколских установа,
- да су резултати коректно наведени и
- да нисам кршио/ла ауторска права и користио интелектуалну својину других лица.

Потпис докторанда

У Београду, _____



Прилог 2.

Изјава о истоветности штампане и електронске верзије докторског рада

Име и презиме аутора Абубакар М.А.Кредег _____

Број индекса Д48/13 _____

Студијски програм Докторске студије _____

Наслов рада „РАСТ ЗАМОРНЕ ПРСЛИНЕ У Т ЗАВАРЕНОМ СПОЈЕВИМА ОД
АЛУМИНИЈУМСКЕ ЛЕГУРЕ - FATIGUE CRACK GROWTH IN T WELDED
JOINTS OF ALUMINUM ALLOY“ _____

Ментор Проф. Др Александар Седмак _____

Потписани/а Абубакар М.А. Кредег _____

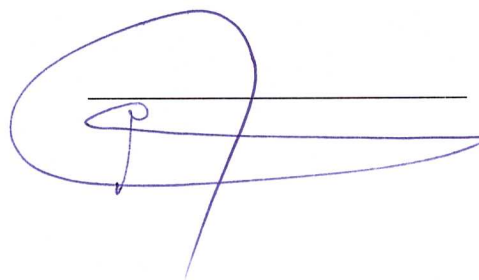
Изјављујем да је штампана верзија мог докторског рада истоветна електронској верзији коју сам предао/ла за објављивање на порталу **Дигиталног репозиторијума Универзитета у Београду**.

Дозвољавам да се објаве моји лични подаци везани за добијање академског звања доктора наука, као што су име и презиме, година и место рођења и датум одбране рада.

Ови лични подаци могу се објавити на мрежним страницама дигиталне библиотеке, у електронском каталогу и у публикацијама Универзитета у Београду.

Потпис докторанда

У Београду, _____



Прилог 3.

Изјава о коришћењу

Овлашћујем Универзитетску библиотеку „Светозар Марковић“ да у Дигитални репозиторијум Универзитета у Београду унесе моју докторску дисертацију под насловом:

„РАСТ ЗАМОРНЕ ПРСЛИНЕ У Т ЗАВАРЕНОМ СПОЈЕВИМА ОД АЛУМИНИЈУМСКЕ ЛЕГУРЕ - FATIGUE CRACK GROWTH IN T WELDED JOINTS OF ALUMINUM ALLOY“

која је моје ауторско дело.

Дисертацију са свим прилозима предао/ла сам у електронском формату погодном за трајно архивирање.

Моју докторску дисертацију похрањену у Дигитални репозиторијум Универзитета у Београду могу да користе сви који поштују одредбе садржане у одабраном типу лиценце Креативне заједнице (Creative Commons) за коју сам се одлучио/ла.

1. Ауторство

2. Ауторство - некомерцијално

3. Ауторство – некомерцијално – без прераде

4. Ауторство – некомерцијално – делити под истим условима

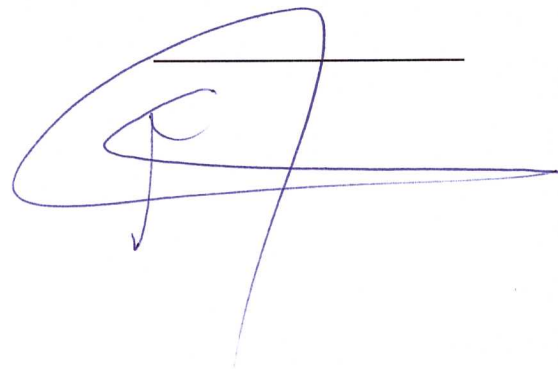
5. Ауторство – без прераде

6. Ауторство – делити под истим условима

(Молимо да заокружите само једну од шест понуђених лиценци, кратак опис лиценци дат је на полеђини листа).

Потпис докторанда

У Београду, _____



1. **Ауторство** - Дозвољаваате умножавање, дистрибуцију и јавно саопштавање дела, и прераде, ако се наведе име аутора на начин одређен од стране аутора или даваоца лиценце, чак и у комерцијалне сврхе. Ово је најслободнија од свих лиценци.
2. **Ауторство – некомерцијално.** Дозвољаваате умножавање, дистрибуцију и јавно саопштавање дела, и прераде, ако се наведе име аутора на начин одређен од стране аутора или даваоца лиценце. Ова лиценца не дозвољава комерцијалну употребу дела.
3. **Ауторство - некомерцијално – без прераде.** Дозвољаваате умножавање, дистрибуцију и јавно саопштавање дела, без промена, преобликовања или употребе дела у свом делу, ако се наведе име аутора на начин одређен од стране аутора или даваоца лиценце. Ова лиценца не дозвољава комерцијалну употребу дела. У односу на све остале лиценце, овом лиценцом се ограничава највећи обим права коришћења дела.
4. **Ауторство - некомерцијално – делити под истим условима.** Дозвољаваате умножавање, дистрибуцију и јавно саопштавање дела, и прераде, ако се наведе име аутора на начин одређен од стране аутора или даваоца лиценце и ако се прерада дистрибуира под истом или сличном лиценцом. Ова лиценца не дозвољава комерцијалну употребу дела и прерада.
5. **Ауторство – без прераде.** Дозвољаваате умножавање, дистрибуцију и јавно саопштавање дела, без промена, преобликовања или употребе дела у свом делу, ако се наведе име аутора на начин одређен од стране аутора или даваоца лиценце. Ова лиценца дозвољава комерцијалну употребу дела.
6. **Ауторство - делити под истим условима.** Дозвољаваате умножавање, дистрибуцију и јавно саопштавање дела, и прераде, ако се наведе име аутора на начин одређен од стране аутора или даваоца лиценце и ако се прерада дистрибуира под истом или сличном лиценцом. Ова лиценца дозвољава комерцијалну употребу дела и прерада. Слична је софтверским лиценцама, односно лиценцама отвореног кода.